SANDIA REPORT
SAND20XX-XXXX
Printed Click to enter a date

Sandia National Laboratories

Post-Fukushima Research and Development Strategy for MELCOR

Lucas I. Albright and David L. Luxat

Prepared by
Sandia National Laboratories
Albuquerque, New Mexico
87185 and Livermore,
California 94550

Issued by Sandia National Laboratories, operated for the United States Department of Energy by National Technology & Engineering Solutions of Sandia, LLC.

Available to DOE and DOE contractors from
U.S. Department of Energy
Office of Scientific and Technical Information
P.O. Box 62
Oak Ridge, TN 37831

Telephone: (865) 576-8401
Facsimile: (865) 576-5728
E-Mail: reports@osti.gov
Online ordering: http://www.osti.gov/scitech

Available to the public from
U.S. Department of Commerce
National Technical Information Service
5301 Shawnee Rd
Alexandria, VA 22312

Telephone: (800) 553-6847
Facsimile: (703) 605-6900
E-Mail: orders@ntis.gov
Online order: https://classic.ntis.gov/help/order-methods/

ABSTRACT

Numerous MELCOR modeling improvements and analyses have been performed in the time since the severe accidents at Fukushima Daiichi Nuclear Power Station that occurred in March 2011. This report briefly summarizes the related accident reconstruction and uncertainty analysis efforts. It further discusses a number of potential pursuits to further advance MELCOR modeling and analysis of the severe accidents at Fukushima Daiichi and severe accident modeling in general. Proposed paths forward include further enhancements to identified MELCOR models primarily impacting core degradation calculations, and continued application of uncertainty analysis methods to improve model performance and a develop deeper understanding of severe accident progression.

ACKNOWLEDGEMENTS

This work was jointly supported by the U.S. DOE-NE IUP Fellowship Program and the United States Nuclear Regulatory Commission. The views expressed in the article do not necessarily represent the views of the U.S. Department of Energy or the United States Government.

Sandia National Laboratories is a multimission laboratory managed and operated by National Technology & Engineering Solutions of Sandia, LLC, a wholly owned subsidiary of Honeywell International Inc., for the U.S. Department of Energy's National Nuclear Security Administration under contract DE-NA0003525.

CONTENTS

1. Introduction 12
   1.1. Overview of the Severe Accidents at Fukushima Daiichi 12
   1.2. Objectives and Scope 13
2. MELCOR Modeling Research and Development 14
   2.1. Fukushima Daiichi Accident Reconstruction 14
   2.2. Uncertainty Analysis 14
   2.3. Overview of Outstanding Issues 15
      2.3.1. MELCOR Model Improvements 15
      2.3.2. Large-Scale Uncertainty Analysis 16
3. Summary 17

Appendix A. Reference Case Analysis 19

1. Introduction 20
2. Materials and Methods 24
   2.1. MELCOR V2.2 24
      2.1.1. MELCOR Eutectics Model 24
      2.1.2. MELCOR Interactive Materials Model 27
   2.2. Plant Representation 28
      2.2.1. Plant Model Parameters 29
      2.2.2. Scenario Assumptions 29
   2.3. Comparison Methodology 30
3. Results and Discussion 31
   3.1. Overall Accident Progression 31
   3.2. Hydrogen Generation 33
   3.3. Thermal Hydraulic Response 35
      3.3.1. Primary Coolant System Response 35
      3.3.2. Containment Response 37
   3.4. Reactor Core Degradation 39
   3.5. RPV Lower Head Breach 45
4. Conclusions 50

Appendix B. Uncertainty Analysis 53

1. Introduction 54
   1.1. Material Interactions and Core Degradation 54
   1.2. Material interactions, Core Slumping, and Lower Head Failure 55
2. Materials and Methods 56
   2.1. MELCOR V2.2 56
      2.1.1. MELCOR Material Interactions Models 56
      2.1.2. MELCOR Candling Models 57
      2.1.3. MELCOR Fuel Rod Failure Models 58
      2.1.4. MELCOR Debris Quenching and Dryout Models 60
   2.2. Plant Representation 62
   2.3. Parametric Uncertainty Analysis Specification 62
      2.3.1. Material Interactions Model Parameters 64
      2.3.2. Candling Model Parameters 65

2.3.3. Fuel Rod Failure Model Parameters 65
2.3.4. Debris Quenching and Dryout Parameters 66
2.4. Comparison Methodology 67
3. Results and Discussion 67
3.1. Overall Accident Progression 67
3.2. Hydrogen Generation 70
3.3. Thermal Hydraulic Response 71
3.3.1. Primary Coolant System Response 72
3.3.2. Containment Response 74
3.4. Reactor Core Degradation 75
3.5. RPV Lower Head Breach 85
4. Conclusions 93

LIST OF FIGURES

Figure 1. Fuel-clad system material evolution. (a) relatively unreacted fuel-clad, (b) significantly reacted fuel-clad, (c) significantly reacted fuel-clad with α-Zr(O) melting point < T < ZrO_2 melting point. 21
Figure 2. Pseudo-binary phase diagram of the UO_2-ZrO_2 system [15] 23
Figure 3. Core degradation maps over 25 hours (a) initial core configuration, (b) 4.0 hours core degradation map, (c) 5.0 hours core degradation map just before core plate failure, (d) 5.28 hours core degradation map after core slumping has occured, (e) 8.33 hours core degradation map just before lower head failure in the eutecitcs model simulation, (f) 25 hours core degradation map 33
Figure 4. Comparison of hydrogen generation by material. 34
Figure 5. Comparison of hydrogen generation distribution. 35
Figure 6. Comparison of the RPV pressure transient. Vertical bands highlight periods of IC operation (0.0-0.8 hours), sustained SRV cycling (~0.8 - lower head failure), and post-lower head failure (lower head failure - 25 hours), respectively. 36
Figure 7. Comparison of the steam dome temperature transient. 37
Figure 8. Comparison of the RPV water level transient 37
Figure 9. Comparison of the drywell pressure transient. 38
Figure 10. Comparison of the wetwell pressure transient. 38
Figure 11. Comparison of the suppression pool temperature transient. 39
Figure 12. Comparison of the core melting progression. 40
Figure 13. Comparison of the minimum axial flow area through the active core region. 41
Figure 14. Comparison of control blade poison temperatures. 41
Figure 15. Comparison of control blade damage progression. 42
Figure 16. Comparison of fuel canister temperatures 42
Figure 17. Comparison of fuel canister damage progression. 43
Figure 18. Comparison of fuel cladding temperatures. 44
Figure 19. Comparison of fuel cladding damage progression. 44
Figure 20. Comparison of fuel temperatures. 45
Figure 21. Comparison of fuel damage progression. 45
Figure 22. Comparison of debris mass distribution. Total Mass: total mass of all materials (intact and debris) in the RPV, Total RPV: total debris mass (conglomerate and particulate) in the RPV, Total AC: total debris mass (conglomerate and particulate) in the active core, Total LP:

total debris mass (conglomerate and particulate) in the lower plenum, and Conglomerate RPV: total conglomerate debris mass in the RPV. 46
Figure 23. Comparison of lower plenum debris masses. 47
Figure 24. Comparison of particulate debris temperatures. 47
Figure 25. Comparison of oxidic molten pool temperatures. 48
Figure 26. Comparison of metallic molten pool temperatures. 48
Figure 27. Comparison of lower head inner wall temperatures. 49
Figure 28. Comparison of ejected debris masses. 50
Figure 29. Default time-at-temperature fuel rod failure model [5] [6]. 60
Figure 30. Event progression summary strip plot (scatter plot with one categorical axis). The x-axis shows categorical events; TAF: top of active fuel, Candling: onset of candling, BAF: bottom of active fuel, CPF: core plate failure, LHF: lower head failure. The y-axis shows the event timing for every realization and event category. 69
Figure 31. Strip plot of in-vessel, integral hydrogen generation from core material oxidation after 25.0 hours. The x-axis shows categories of core materials that can produce hydrogen during oxidation; TOTAL: all materials, ZR: zirconium, SS: stainless steel, B4C: boron carbide. The y-axis shows integral hydrogen generation (after 25.0 hours) through oxidation of a given material for every case. 70
Figure 32. Strip plot of in-vessel, integral hydrogen generation in radial core rings after 25.0 hours. The x-axis shows radial core rings; ring 1 is the innermost ring and ring 5 is the outermost ring in the active core region. The y-axis shows integral hydrogen generation (after 25.0 hours) through core material oxidation in a given core ring for every case. 71
Figure 33. RPV water level (y-axis) relationship with debris mass in the lower plenum (x-axis) at 5.5 hours. Marker types represent core plate damage states; circle: core plate intact, triangle: core plate failed. 72
Figure 34. Steam dome temperature (y-axis) relationship with debris mass in the lower plenum (x-axis) at (a) 5.5 hours and (b) 10.3 hours. Marker sizes represent core plate damage states; large: core plate intact, small: core plate has failed. Marker types represent lower head damage states; circle: lower head intact, triangle: lower head failed. 74
Figure 35. Drywell pressure (y-axis) dependence on in-vessel hydrogen generation (x-axis) at 10.3 hours. Marker types represent lower head damage states; circle: lower head intact, triangle: lower head failed. 75
Figure 36. Normalized axial flow area of the core (x-axis) relationship with fuel intact mass fraction (y-axis) at 5.5 hours. Marker types represent core plate damage states; circle: core plate intact, triangle: core plate failed. 76
Figure 37. Molten mass (y-axis) relationship with the normalized axial flow area of the core (x-axis) at 5.5 hours. Marker types represent core plate damage states; circle: core plate intact, triangle: core plate failed. 77
Figure 38. Component damage progression strip plots at (a) 4.5 hours and (b) 6.5 hours. The x-axis shows categories of core components; TOTAL: total core (all core components), NS: non-supporting structure (control blade), CN: fuel canister, CL: fuel cladding, FU: fuel. The y-axis shows the intact mass fraction of each component category for every realization. 78
Figure 39. Maximum component temperature strip plot. The x-axis shows categories of core components; TOTAL: all core components, NS: non-supporting structure (control blade), CN+CB: fuel canister, CL: fuel cladding, FU: fuel. The y-axis shows the intact mass fraction of each component category for every realization. 79

Figure 40. Cladding damage progression (y-axis) relationship with breach temperature (x-axis) at 6.5 hours. Marker sizes represent the relationship between the breach and relocation temperatures; small: $Tbreach < Treloc$, large: $Tbreach > Treloc$ 80
Figure 41. Maximum cladding temperature (y-axis) relationship with relocation temperature (x-axis). Marker types represent the integrity of the cladding oxide layer; circle: $\mathrm{OXTH} < \mathrm{R}hold$ (cannot hold up molten materials), triangle: $\mathrm{OXTH} > \mathrm{R}hold$ (can hold up molten materials). 82
Figure 42. Fuel damage progression (y-axis) relationship with relocation temperature (x-axis) at 6.5 hours. Marker sizes represent the relationship between the breach and relocation temperatures; small: $Tbreach < Treloc$, large: $Tbreach > Treloc$ 82
Figure 43. Maximum fuel temperature (y-axis) relationship with relocation temperature (x-axis). Marker types represent the integrity of the cladding oxide layer; circle: $\mathrm{OXTH} < \mathrm{R}hold$ (cannot hold up molten materials), triangle: $\mathrm{OXTH} > \mathrm{R}hold$ (can hold up molten materials)... 83
Figure 44. Core plate failure timing (x-axis) relationship with the ratio between relocation temperature and breach temperature (y-axis). 84
Figure 45. Debris mass distribution strip plots at 6.5 hours. The x-axis shows region categories in the RPV; RPV: entire RPV region, AC: active core region, LP: lower plenum region. The y-axis shows the debris mass in each region category for every realization. 85
Figure 46. Lower plenum debris masses strip plot at 6.5 hours. The x-axis shows the debris type categories; PD: particulate debris, MP1: oxidic molten pool, MP2: metallic molten pool. The y-axis shows the mass of each debris type category for every realization. 86
Figure 47. Maximum particulate debris temperature in the lower plenum (y-axis) relationship with relocation temperature (x-axis). 87
Figure 48. Maximum particulate debris mass in the lower plenum (y-axis) relationship to time of lower head failure (x-axis). Marker sizes represent the core plate failure timing; small: core plate failure timing < 14.0 hours, large: core plate failure timing > 14.0 hours. 88
Figure 49. Maximum oxidic molten pool temperature in the lower plenum (y-axis) relationship with relocation temperature (x-axis). 89
Figure 50. Maximum metallic molten pool temperature in the lower plenum (y-axis) relationship with relocation temperature (x-axis). 90
Figure 51. Lower head temperature (y-axis) relationship with debris mass in the lower plenum (x-axis) at 10.3 hours. Marker types represent lower head damage states; circle: lower head intact, triangle: lower head failed. Marker size represents lower plenum dryout timing; small: lower plenum dryout > 8.8 hours, large: lower plenum dryout < 8.8 hours. 91
Figure 52. Lower head failure timing (x-axis) relationship with relocation temperature (y-axis). Marker sizes represent the relationship between the breach and relocation temperatures; small: $Tbreach < Treloc$, large: $Tbreach > Treloc$. 92
Figure 53. Ejected debris masses strip plot at 25.0 hours. The x-axis shows categories of core materials; ZR: zirconium, SS: stainless steel, SSOX: oxidized stainless steel, UO2: uranium dioxide, ZRO2: oxidized zirconium, TOTAL: all core materials. The y-axis shows the mass of each core material category for every realization. 93

LIST OF TABLES

Table 1. MELCOR Eutectics Model Binary Material Interaction Parameters 25

Table 2. Parabolic Rate Constants by Material [2] [3] 27
Table 3. BWR/3 Reactor Model Parameters 28
Table 4. Boundary Conditions 30
Table 5. Key Event Timings 31
Table 6. Alternate Refreezing Components 57
Table 7. Uncertain Parameters 63

This page left blank

ACRONYMS AND DEFINITIONS

Abbreviation	Definition
FDNPS	Fukushima-Daiichi Nuclear Power Station
IC	Isolation condenser
RCIC	Reactor core isolation cooling
RPV	Reactor pressure vessel
ECCS	Emergency core cooling systems
HPCI	High pressure core injection
ADS	Automatic depressurization system
MSLR	Main steam line rupture
R&D	Research and development
BSAF Project	Benchmark Study of the Accident at the Fukushima Daiichi Nuclear Power Plant
OECD	Organisation For Economic Co-Operation And Development
NEA	Nuclear Energy Agency
CSNI	Committee on the Safety of Nuclear Installations

1. INTRODUCTION

1.1. Overview of the Severe Accidents at Fukushima Daiichi

On March 11, 2011 at 14:46 JST, the Great East Japan Earthquake shook the coast of japan. The shock was measured as a magnitude M 9.0 earthquake, lasting for 140-160 seconds. An estimated 50m lateral east-south-east displacement and 7m-10m upward displacement triggered a two-stage tsunami. At the FDNPS, the earthquake damaged vital switchyard equipment and all six off-site power lines, causing a loss of off-site power and triggering a reactor scram at operating units. 39 minutes after the earthquake, the first tsunami reached the FDNPS, and 10 minutes later the second tsunami, with a height of 14-15m, overwhelmed tsunami walls. That water that breached the tsunami walls damaged plant systems, structures, and components (including diesel generators) and onsite structures and also inundated the site with seawater, sand, silt, and debris **Error! Reference source n ot found.**.

The accident at Fukushima Daiichi Unit 1 progressed more quickly than at units 2 and 3 because the accident was largely unmitigated despite significant efforts by plant staff. Initially, decay heat removal and core cooling were maintained by operation of the isolation condensor. Unfortunately, at the time of the tsunami, operators had throttled the IC, an action taken to prevent core temperatures from dropping excessively, and they were unable to restart either IC train due to loss of power. Operators made numerous attempts to reestablish injection into the core. Without core cooling, the core boil-off and subsequent degradation progressed quickly. It is believed that during the accident, the bolts securing the head of the drywell were stretched and that the head lifted, allowing combustible gases and fission products to leak from containment into the refueling bay. Shortly after the operators vented the wetwell, a hydrogen explosion was observed at unit 1 [1][2][3]. Current observations from ongoing decommissioning efforts suggest that nearly all core materials were ejected to the cavity after lower head failure [4].

At Fukushima Daiichi Unit 2, severe accident conditions were significantly delayed by unexpected RCIC operation to about 70 hours. Ultimately, the RCIC system was unable to compensate, and it failed. After RCIC failure, core degradation proceeded through lower head and containment failure. Manual RPV depressurization was initiated by plant staff to attempt emergency water injection. Shortly after blowdown, three pressure spikes are observed in the primary system. These pressure spikes are likely due to boiloff and material relocation events [1][2][3]. Current observations from decommissioning efforts suggest that a large quantity of debris was held up in the lower plenum of the RPV, and that the thin layer of debris in the cavity is metallic [4].

The accident at Fukushima Daiichi Unit 3 was also delayed by ECCS operation – the RCIC system was operated for 21.5 hours after which the HPCI was operated until its failure at 36 hours. After termination of injection by either ECCS, significant core degradation occurred. Rapid depressurization of the primary system is observed near 42 hours, possibly by MSLR or erroneous ADS operation. Similar to unit 2, pressure spikes in the primary system are observed after blowdown and are likely caused by material relocation events [1][2][3]. Current observations from decommissioning efforts suggest that little to no debris remains in the lower plenum of the RPV and the presence of a large debris bed in the cavity [4].

1.2. Objectives and Scope

The primary objective of this report is to summarize the research and development strategy for the MELCOR code accounting for severe accident progression and modeling insights developed through Fukushima Daiichi research efforts in the years since the accidents.

The R&D strategy presented in this document reflects MELCOR modelling R&D efforts and intentions according to the current understanding of light water reactor severe accident progression and modeling and the severe accidents that occurred at Fukushima Daiichi.

2. MELCOR MODELING RESEARCH AND DEVELOPMENT

In response to the events at Fukushima Daiichi, several MELCOR initiatives have been pursued to demonstrate and improve MELCOR severe accident modeling capabilities. Significant modeling improvements have been made to the MELCOR code as part of these initiatives including improved computational performance and enhanced material interaction modeling [2][5][6]. MELCOR modeling capabilities have been demonstrated through accurate reconstructions of the multi-unit severe accident at Fukushima Daiichi as part of the Benchmark Study of the Accident at the Fukushima Daiichi Nuclear Power Plant (BSAF Project) and through follow-up large-scale uncertainty analyses [2][7][8][9].

2.1. Fukushima Daiichi Accident Reconstruction

Reconstructions of the accidents at Fukushima Daiichi, as they are currently understood, for each of the reactor units was performed by Sandia National Laboratories using MELCOR V2.2 during the BSAF project. The BSAF project, which was directed by the OECD/NEA/CSNI, concluded in 2018 [2]. The aim of the project's first phase was to evaluate the accident progression and source terms in the primary containment vessel for each of the reactor units out to 7 days after the initiating event. Phase II of the BSAF project expanded the scope to include analysis of accident progression and source terms out to three weeks after the initiating event. As a participant in the BSAF Project, SNL developed three week long MELCOR simulations for each Fukushima Daiichi Nuclear Power Station reactor and a single, combined MACCS simulation combining each of the three MELCOR simulations. The accident simulations produced during the BSAF project accurately reconstruct the accidents that occurred at each reactor unit at FDNPS by using the forensic approach. With the forensic approach, subject matter experts interpret available plant data to reconstruct a plausible accident progression (e.g., debris relocation, lower head failure, etc.) that reasonably recreates observed accident signatures (e.g., pressure spikes, hydrogen combustion, etc.). The postulated accident progression is enforced as a boundary condition in a MELCOR calculation that is evaluated for its accuracy in reproducing the accident sequence. Through application of this analysis methodology in tandem with MELCOR modeling improvements, the severe accident analysis and modeling team members developed MELCOR simulations representative of the severe accidents FDNPS to produce accurate source term estimates.

2.2. Uncertainty Analysis

Following the BSAF project, the ARC-F project was launched by OECD/NEA/CSNI to develop a deeper understanding of severe accident progression and the status of Fukushima Daiichi Nuclear Power Station reactors. As part of the ARC-F project SNL has pursued investigations into the impact of uncertainties on the in-vessel accident progression at the Fukushima Daiichi Nuclear Power Station reactors. These efforts have focused on an investigation into the effect of material interactions on severe accident progression at Fukushima Daiichi Unit 1 through material interaction model uncertainty analysis [7][8][9]. The analysis was subdivided into two parts: (1) a reference case comparison between MELCOR simulations using the *interactive materials model* or the *eutectics model* using nominal model parameters, and (2) an uncertainty analysis that investigated the parametric uncertainty space of each material interaction model and its interaction with other core degradation models. The uncertainty analysis was not best estimate, but exploratory with the intent to investigate model differences across the full range of considered parametric uncertainties. In this study accelerated core degradation occurred in eutectics model simulations, including key events such as

core plate failure and lower head failure. Eutectics model simulations also exhibited larger quantities of molten debris and higher maximum fuel and debris temperatures. Material interaction model differences were found to impact core degradation pathways leading to bifurcation in accident progression characteristics.

2.3. Overview of Outstanding Issues

As demonstrated in the previous Fukushima Daiichi severe accident analysis efforts, the MELCOR code can produce accurate reconstructions of the severe accidents, as they are currently understood, for each of the reactor units. In fact, it is believed that some of the largest uncertainties concerning the accidents at Fukushima Daiichi are not parametric, model uncertainties, but event uncertainties. Event uncertainties, or uncertainties in the accident progression, that have persisted since the Fukushima Daiichi severe accidents are tied to the limited data that was collected during the accidents because of loss of power and other onsite challenges. The scarcity of data hinders analysts' abilities to develop a straightforward, comprehensive characterization of the accident progression. Remaining uncertainties at each of the reactor units include the quantity of water successfully injected into the reactor cores/elsewhere in containment, degree of debris oxidation and hydrogen mass generated, primary system depressurization mode, debris composition and characteristics prior to lower head failure and ex-vessel, the mode of lower head failure, the extent of CCI, and the potential for liner melt-through. Despite these remaining questions, key observations from available accident data can be accurately reproduced, within acceptable uncertainty limits, by multiple variations of the postulated accident sequences using the MELCOR code. And although uncertainties in the accident progression surrounding key events have persisted through single case best-estimate accident analyses, they can be reduced and better resolved through continued improvements to the MELCOR code and continued application of large-scale uncertainty analysis methods.

2.3.1. MELCOR Model Improvements

Through the enhancement of current MELCOR models and the addition of new models to fill existing gaps, the MELCOR code analyses of the FDNPS severe accidents will be further improved. For example, material interaction modelling in MELCOR has been revisited and enhanced since the accidents at Fukushima Daiichi to more accurately capture early component failure, interactions between core debris and in-vessel structures, in-vessel debris morphology, interactions between core debris and ex-vessel structures, and ex-vessel debris morphology phenomena. Through enhancements to material interaction modeling in MELCOR, capabilities to model the behavior of material mixtures are increased. Specifically, composition-dependent mixture properties and the relocation of mixtures is treated more generally. Further enhancements, however, are possible. Specifically, a generalized thermochemistry model to treat multicomponent mixtures across a variety of core component types, and thermochemical reactions between core debris and the lower head.

Other identified, open core degradation model enhancements include the oxidation of debris in motion, melting and relocation of non-core in-vessel structures, localized attack and failure of the core plate, and lower head failure modeling. Potential enhancements to thermal hydraulic models include suppression pool thermal stratification modeling, buoyant and momentum-driven plume flow structures, and numerical performance during low-pressure boil-off transients. Ex-vessel phenomena that can be enhanced include corium interactions with below-vessel structures, CCI

modeling, including further evaluation of water ingress models, and finally ex-vessel coolability considering alternate debris bed morphologies.

Lastly, MELCOR models representative of plant instrumentation have been proposed as potential enhancements. Such models would approximate the behavior of plant instrumentation relative to the actual plant status (e.g., a core water level instrumentation model versus the actual water level predicted by MELCOR) [10].

2.3.2. Large-Scale Uncertainty Analysis

Further insights into the severe accidents at FDNPS and severe accident progression more generally can be developed through continued application and development of large-scale uncertainty analysis methods. To date, parametric uncertainty studies have dominated severe accident analysis applications. Further advancement can occur by expanding the dimensions of the uncertainty space considered to include event and model form uncertainties.

Expanded uncertainty analyses can give rise to emergent patterns that inform both model development and severe accident understanding. Such analyses can be used to drive model development efforts through demonstrating model robustness and performance, investigating model bias, and even surveying for potential gaps in modeling. The results from such analyses naturally lead to more robust, accurate modeling of severe accident progression. Similarly, expanded uncertainty analysis broadens the domain of accident progression variations considered, eliciting accident progression pathways, attractor states, and other patterns that would otherwise remain obscured. In those patterns, analysts will expose deeper insights into severe accident progression and mitigative actions.

3. SUMMARY

Advancements in the understanding of severe accidents have been made through a combination of model development and analysis efforts since the severe accidents at Fukushima Daiichi. Model development efforts have including enhanced numerical performance, improved RCIC modeling, and enhanced material interaction modeling. Such model developments have stimulated further MELCOR analyses including accurate reconstruction of the severe accidents at Fukushima Daiichi and large-scale uncertainty analysis investigations into material interaction models and their impact on accident progression. Outlying issues and remaining questions that have arisen from Fukushima Daiichi model development and analysis efforts can be resolved through further studies. Proposed work includes further model development efforts including core degradation model enhancements and further uncertainty analysis efforts that consider expanded uncertainty space domains. Pursuit of both efforts in parallel will produce more robust, accurate models and a deeper understanding of severe accident progression that can be used to improve mitigative actions.

REFERENCES

[1] International Atomic Energy Agency, "The Fukushima Daiichi Accident Technical Volume 1 Description and Context of the Accident" International Atomic Energy Agency, Vienna, 2015.

[2] OECD Nuclear Energy Agency, "Benchmark Study of the Accident at the Fukushima Daiichi Nuclear Power Plant - (BSAF Project) -- Phase I Summary Report," OECD/NEA/CSNI, 2016.

[3] N. Andrews, C. Faucett, T. Haskin, N. Bixler, D. Clayton, and R. Gauntt, "Sandia National Laboratories' Contribution to the OECD/NEA BSAF Phase II Project," Portland,OR, August, 2019.

[4] TEPCO, https://www.tepco.co.jp/en/hd/decommission/progress/retrieval/index-e.html, last accessed Aug 9, 2021.

[5] L. L. Humphries, B. A. Beeny, C. Faucett, F. Gelbard, T. Haskin, D. L. Louie and J. Phillips, "MELCOR Computer Code Manuals Reference Manual, Vol. 2: Reference Manual," U.S. Nuclear Regulatory Commission, Washington, DC, 2019.

[6] L. L. Humphries, B. A. Beeny, F. Gelbard, D. L. Louie and J. Phillips, "MELCOR Computer Code Manuals Reference Manual, Vol. 1: Primer and Users' Guide," U.S. Nuclear Regulatory Commission, Washington, DC, 2019.

[7] L. I. Albright, N. Andrews, L. L. Humphries, R. O. Gauntt and T. Jevremovic, "Uncertainty Analysis of Corium Relocation to the Lower Plenum Using Results from The OECD/NEA BSAF Phase II Project," Portland,OR, August, 2019.

[8] L. I. Albright, N. Andrews, L. L. Humphries, M. H. Piro, G. E. Sjoden, D. L. Luxat and T. Jevremovic, "Material Interactions in Severe Accidents - Benchmarking the MELCOR V2.2 Eutectics Model for a BWR-3 Mark-I Station Blackout: Part I - Single Case Analysis," *Accepted.*

[9] L. I. Albright, N. Andrews, L. L. Humphries, D. L. Luxat and T. Jevremovic, "Material Interactions in Severe Accidents - Benchmarking the MELCOR V2.2 Eutectics Model for a BWR-3 Mark-I Station Blackout: Part II - Uncertainty Analysis," *Accepted.*

[10]J. L. Rempe, "SAMMI 2020 – Summary Conference Report," Rempe and Associates, LLC, Idaho Falls, 2020.

APPENDIX A. REFERENCE CASE ANALYSIS

MATERIAL INTERACTIONS IN SEVERE ACCIDENTS - BENCHMARKING THE MELCOR V2.2 EUTECTICS MODEL FOR A BWR-3 MARK-I STATION BLACKOUT: PART I - SINGLE CASE ANALYSIS

Lucas I. Albright[a,b,*], Nathan Andrews[a], Larry L. Humphries[a], Markus H.A. Piro[c], Glenn E. Sjoden[b], David L. Luxat[a], Tatjana Jevremovic[d]

[a]*Sandia National Laboratories,1515 Eubank, Albuquerque, New Mexico 87123, United States of America*
[b]*University of Utah, 201 Presidents Cir, Salt Lake City, Utah 84112, United States of America*
[c]*Ontario Tech University, 2000 Simcoe Street North, Oshawa, Ontario L1G OC5, Canada*
[d]*International Atomic Energy Agency, Wagramer Str.5, 1220 Vienna, Austria*

ABSTRACT

In this analysis, the two material interaction models available in the MELCOR code are benchmarked for a severe accident at a BWR under representative Fukushima Daiichi boundary conditions. This part of the benchmark investigates the impact of each material interaction model on accident progression through a detailed single case analysis. It is found that the eutectics model simulation exhibits more rapid accident progression for the duration of the accident. The slower accident progression exhibited by the interactive materials model simulation, however, allows for a greater degree of core material oxidation and hydrogen generation to occur, as well as elevated core temperatures during the ex-vessel accident phase. The eutectics model simulation exhibits more significant degradation of core components during the late in-vessel accident phase – more debris forms and relocates to the lower plenum before lower head failure. The larger debris bed observed in the eutectics model simulation also reaches higher temperatures, presenting a more significant thermal challenge to the lower head until its failure. At the end of the simulated accident scenario, however, core damage is comparable between both simulations due to significant core degradation that occurs during the ex-vessel phase in the interactive materials model simulation. A key difference between the two models' performance is the maximum temperatures that can be reached in the core and therefore the maximum ΔT between any two components. When implementing the interactive materials model, users have the option to modify the liquefaction temperature of the ZrO_2-interactive and UO_2-interactive materials as a way to mimic early fuel rod failure due to material interactions. Through modification of the liquefaction of high melting point materials with significant mass, users may inadvertently limit maximum core temperatures for fuel, cladding, and debris components.

HIGHLIGHTS

- The eutectics model simulation exhibits accelerated accident progression in comparison to the interactive materials model simulation
- Earlier degradation of fuel components is observed for the eutectics model simulation

* Corresponding Author
Email Addresses: lialbri@sandia.gov, (Lucas I. Albright), nandrew@sandia.gov (Nathan Andrews), llhumph@sandia.gov (Larry L. Humphries), dlluxat@sandia.gov (David L. Luxat), T.Jevremovic@iaea.org (Tatjana Jevremovic)

- The eutectics model simulation exhibits greater quantities of both molten and refrozen, conglomerate debris
- Greater masses of debris are formed and ejected from the RPV in the eutectics model simulation
- The interactive materials model simulation exhibits lower peak temperatures for fuel, cladding, and debris components

Keywords: MELCOR, Severe Accident, Material Interactions, Eutectics Model, Interactive Materials Model

1. INTRODUCTION

The treatment of material interactions in modern severe accident analyses is evolving. For over two decades, material interactions have been known to accelerate the degradation of reactor core systems, structures, and components (SSCs) during severe accidents in light water reactors (LWRs) [1]. Recently, severe accident experts have recognized the need to improve traditionally implemented material interaction models. Previously, modification of global, constituent material melting points of known reactions was sufficient to capture material interaction physics to the necessary degree accuracy in the MELCOR code [2] [3]. Today, the MELCOR code is moving towards higher fidelity material interaction models thanks to insights gained by post-accident analysis of the severe accidents at Fukushima Daiichi and expectant safety analysis of emerging reactor technologies. With the advent of mature accident tolerant fuels and next-generation reactor designs, it is imperative that accurate treatment of material interactions be incorporated into severe accident codes to fully capture the complex behavior of material interactions and multi-component mixtures under severe accident conditions.

Design-specific SSCs as well as materials will determine the importance of material interactions to core damage progression. As a matter of fact, interactions between SSC materials are known to occur at all temperatures. At low temperatures, however, the reaction rate is often slow enough that the effect is negligible. At higher temperatures, the reaction rate accelerates. Under prolonged extreme temperature conditions, as experienced during a severe accident, material interactions can contribute to, or even cause, early failure of core SSCs (e.g. control rods, fuel assemblies, and other core support structures) and fission product barriers (FPBs) (e.g. fuel matrix, fuel cladding, reactor pressure vessel (RPV)) [4] [5]. Such interactions can be solid-solid interactions that form low melting point alloys and eutectic mixtures, or chemical dissolution of solids by a liquid mixture. After failure of SSCs and FPBs, core materials relocate downward and coolable rod-like geometry may be lost – coolable geometry is impaired by phenomena that obstruct the open area of flow channels including bowing, ballooning, candling, and collapse. Of prime importance are material interactions that can lead to early relocation of reactor fuel and fission products (FPs), commonly referred to as "heat-bearing materials" because of their associated decay heat. For LWRs, the interaction between UO_2 fuel and Zr-based fuel cladding materials are known to cause early relocation of heat-bearing materials [1].

Material changes to the fuel-clad system begins with autocatalytic Zr oxidation[1] and the formation of an external oxide scale. Cladding oxidation produces oxygen stabilized α-Zr(O) until the point of oxygen saturation, after which, an oxide scale (ZrO_2) begins to form [1]. The ZrO_2 scale continues to grow as oxygen from the steam diffuses through the scale to oxygen-stabilized and unoxidized portions of the cladding. Internally, oxidation of Zr-based cladding also occurs by oxygen diffusing from the UO_2 fuel pellet at high temperatures. Similarly to external oxidation of Zr-based cladding, the uptake of oxygen by Zr-based cladding from the UO_2 results in α-Zr(O) and hypo-stoichiometric UO_{2-x} that eventually becomes a UO_2 + U (uranium oxide plus liberated metallic uranium) layer [6]. The U metal within this layer will interact with Zr in the neighboring α-Zr(O) layer forming a (U,Zr) alloy. The (U,Zr) alloy in the α-Zr(O) penetrates the full depth of the layer, linking a (U,Zr) layer low in oxygen to the UO_2 + U layer. Finally, there is a second layer of α-Zr(O) before the unoxidized Zr layer. At temperatures above the melting point of zirconium-based cladding, unoxidized portions will melt and dissolve the fuel and oxide scale. The progression of material changes to the fuel clad system are shown in Figure 1.

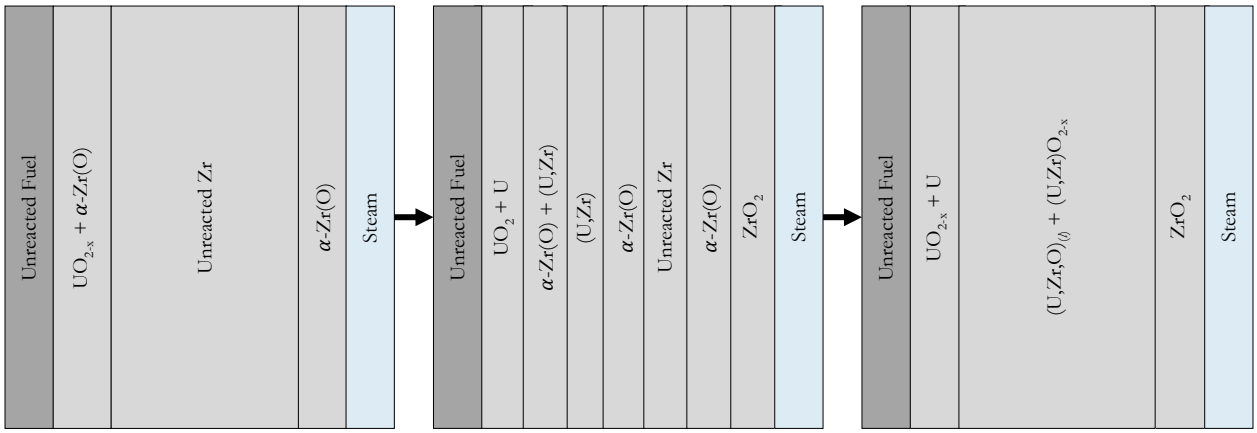

Figure 1. Fuel-clad system material evolution. (a) relatively unreacted fuel-clad, (b) significantly reacted fuel-clad, (c) significantly reacted fuel-clad with α-Zr(O) melting point < T < ZrO_2 melting point.[2]

Dissolution of UO_2 and ZrO_2 by Zr-based cladding occurs rapidly after the onset of melting (around 2000 K-2100 K), far below melting points of either UO_2 (approximately 3100 K) and ZrO_2 (about 3000 K) [1]. Furthermore, UO_2 dissolution by molten Zr-based cladding occurs more quickly than ZrO_2 dissolution. The resulting molten material is a U-Zr-O mixture that continues to dissolve both UO_2 and ZrO_2, accumulating fission products and degrading the protective oxide (ZrO_2) scale until the melt refreezes, or the oxide scale fails. After failure of the oxide scale, the U-Zr-O melt and any fission products contained within it will relocate downward in the core region by the candling process, redistributing the heat production in the core and leading to greater thermo-chemical challenges to FPBs and SSCs at lower core elevations.

[1] It should be noted that oxidation of core materials, and Zr in particular, is a significant source of combustible hydrogen gas. Accumulation of hydrogen gas produced by core material oxidation is safety significant as deflagration and/or detonation may occur.

[2] MELCOR does not model fuel rod degradation at the level of detail shown in Figure 1 (e.g. layering in the cladding).

The chemical dissolution of both UO_2 and ZrO_2 by Zr-based cladding is driven by two primary mechanisms: oxygen diffusion and natural-convection mass transfer [7] [8]. Natural-convection mass transfer occurs when dissolved materials create local density gradients that lead to mixture circulation – standard material densities are as follows: liquid U ~17 g/cm^3, Zr-based cladding ~6 g/cm^3, ZrO_2 ~5.68 g/cm^3 [6]. Density differences caused by UO_2 dissolution are much larger than those caused by ZrO_2 dissolution. Consequently, natural-convection mass transfer has a greater influence on UO_2 dissolution. The convective mass transfer process is defined as [9] [10]:

$$UO_{2-x} + Zr(O)_{(l)} \rightarrow (U, Zr, O)_{(l)} \quad (1)$$

$$ZrO_2 + Zr_{(l)} \rightarrow 2Zr(O)_{(l)} \quad (2)$$

Oxygen diffusion-controlled dissolution follow the chemical path as follows:

$$UO_2 + Zr_{(l)} \rightarrow UO_{2-x} + Zr(O)_{(l)} \rightarrow (U, Zr, O)_{(l)} \quad (3)$$

$$ZrO_2 + Zr_{(l)} \rightarrow ZrO_{2-x} + Zr(O)_{(l)} \quad (4)$$

In the case of UO_2 dissolution, the process occurs in two stages: an initial period of rapid convection-based dissolution that terminates when the resulting mixture reaches U and O saturation and a subsequent period of diffusion-based dissolution and precipitation within the melt; oxygen diffusion from the remaining solid fuel into the melt causes oversaturation of the liquid and precipitation of $(U,Zr)O_{2-x}$ [11]. Oxygen diffusion-based dissolution drives ZrO_2 dissolution because molten Zr-based cladding and ZrO_2 have similar densities (i.e. density differences are too small for appreciable natural convection to occur) [9]. Both UO_2 and ZrO_2 dissolution are heavily influenced by the oxygen content within the melt and any external oxygen sources (e.g. steam). Oxygen diffusion-controlled dissolution of a component can only occur above the melting point of Zr-based cladding after surface wetting of the component by the melt. Surface wettability is material dependent, and different for the various material combinations in the fuel-clad-oxide scale complex [12].

At the fuel-clad interface, oxygen diffuses from the UO_2 into the liquid Zr-based cladding, forming hypo-stoichiometric UO_{2-x} and α-Zr(O). In time, the hypo-stoichiometric UO_{2-x} becomes uranium metal and dissolves into the α-Zr(O), forming a U-Zr-O melt. A similar process occurs externally as oxygen diffuses from the oxide scale to the forming hypo-stoichiometric ZrO_{2-x} and α-Zr(O) [9] [10]. As with cladding oxidation and the formation of the oxide scale, the oxygen diffusion-controlled dissolution process is governed by parabolic kinetics. Parabolic kinetics generally apply to processes where the diffusion is rate-limited by the formation of a protective oxide scale [13]. Mathematically, such a process can be represented by the parabolic rate law, which for reaction processes that include an initial transient period of accelerated reaction kinetics before reaching steady-state parabolic kinetics, takes the following form:

$$(x(T,t) - x_o)^2 = K(T)t \quad (5)$$

where $x(T,t)$ is the mass or weight percent of dissolved material [kg or wt.%] at a given temperature T [K] and time t [s], x_o is the mass or weight percent of that material [kg or wt.%] dissolved during the initial period of rapid dissolution, and $K(T)$ is a temperature dependent rate

constant $\left[\frac{\text{wt.\%}^2}{\text{s}}\right]$. For many reaction processes, the rate constant is given by the Arrhenius relation shown by:

$$K(T) = A\exp\left(\frac{-B}{RT}\right) \tag{6}$$

with experimentally derived correlation constants A and B have units $\left[\frac{\text{wt.\%}^2}{\text{s}}\right]$ and $\left[\frac{\text{J}}{\text{mol}}\right]$, respectively, and the universal gas constant R has units of $\frac{\text{J}}{\text{K·mol}}$. Experimentally derived constants for the correlation were derived by Hoffman et al. and can be found in reference [14].

There are many material interactions that can occur in LWRs that affect core damage progression. Other notable material interactions identified in early studies include Fe/Zr, Zr/Ni, and Fe/B, which impact the integrity of a number of core structures including control rods, grid spacers, and fuel canisters. The earliest interactions to occur in LWRs start near 1200 K (Fe/Zr and Zr/Ni reactions) followed by Fe/B reactions near 1450 K [1]. Historically, research efforts have been dedicated to understanding the pseudo-binary systems of constituent materials (e.g. UO_2-ZrO_2 shown in Figure 2). More recent thermodynamic studies have investigated larger material systems and shown that binary systems of constituent materials do not reflect the compounding effects of multi-component systems, including the complex topology of their phase diagrams; prominent multi-component mixtures that relate to LWR technologies are U-Zr-O, U-Zr-O-Fe, and Fe-Zr-B.

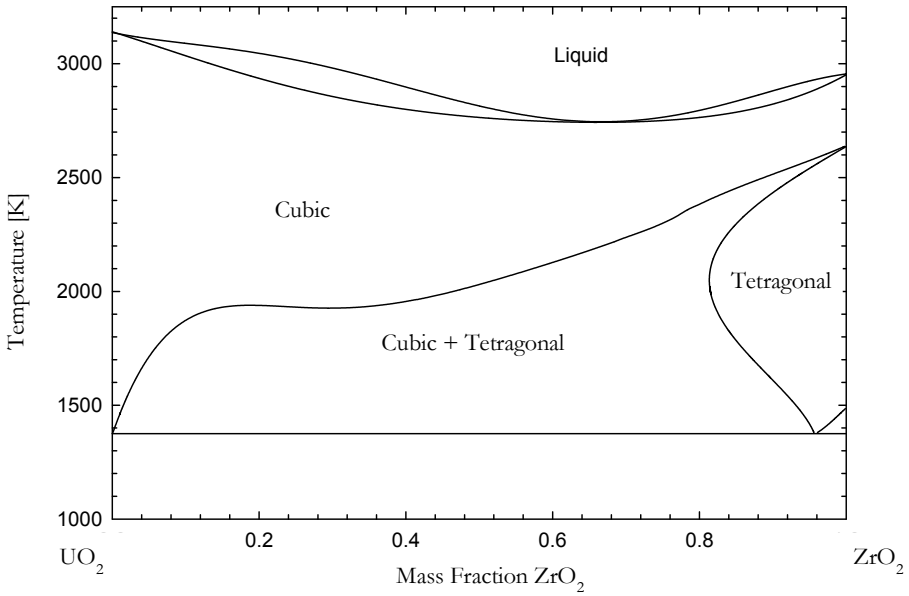

Figure 2. Pseudo-binary phase diagram of the UO_2-ZrO_2 system [15]

In this analysis, the authors have performed a single case, best-estimate analysis using the two material interaction models presently available to MELCOR users for a station blackout (SBO) of a boiling water reactor (BWR) using representative Fukushima Daiichi Unit 1 boundary conditions. The goal of this work is not to replicate the accident progression at Fukushima Daiichi Unit 1, but to perform a fundamental comparison between the eutectics and interactive material models. The single case, best-estimate analysis is performed using MELCOR's eutectics model and repeated using

the "interactive materials" model to provide comparison. The eutectics model was recently implemented as the new default treatment for material interactions in MELCOR, replacing the traditionally utilized interactive materials model. Chapter 2 of this analysis details the authors' approach and includes a summary of MELCOR V2.2 capabilities and relevant models, a description of the plant model used in the analysis, and the analysis comparison methodology. In chapter 3, the authors present analysis results and discuss their importance, while chapter 4 concludes the analysis and highlights key findings.

2. MATERIALS AND METHODS

2.1. MELCOR V2.2

MELCOR is a fully integrated, engineering-level severe accident code developed at Sandia National Laboratories for the U.S. Nuclear Regulatory Commission (USNRC) to support plant licensing and regulatory efforts [2] [3]. MELCOR's capabilities encompass the breadth of severe accident phenomena, spanning the initiating event through the release of radioactive materials to the environment for multiple reactor types. MELCOR uses the control volume approach to capture plant response to accident conditions and grants users significant flexibility when defining plant parameters, from plant nodalization, to correlation and built-in model parameter modification through control functions and sensitivity coefficients. While previous versions of MELCOR were predominately parametric, phenomenological models in the current version are mostly mechanistic; parametric models in general, are limited to phenomena with large uncertainties. This analysis is performed with MELCOR V2.2 revision 15348 [2] [3].

Renewed interest in the importance of material interactions has brought a change in the default treatment of material interactions in MELCOR. The following built-in MELCOR material classes are relevant to this analysis: ZR (representative of Zr-based alloys), ZRO2 (representative of ZrO_2), UO2 (representative of UO_2-based nuclear fuel), SS (representative of stainless steel), SSOX (representative of oxidized stainless steel), INC (representative of inconel), B4C (representative of B_4C control material). In the present section, MELCOR material designations are used in order to maintain consistency with other MELCOR reference materials.

2.1.1. MELCOR Eutectics Model

The eutectics model is currently implemented as the default treatment for material interactions in the MELCOR code but can be overwritten by definition of the necessary interactive materials model parameters. MELCOR's eutectics model enables explicit treatment of material interactions and has three main components: reactions that can cause early failure of fuel and control rods, composition-dependent mixture properties (e.g. reduced liquefaction temperatures), and the dissolution of intact components by molten mixtures.

Molten mixture properties resulting from material interactions are treated for mixtures that have been converted to conglomerate debris. Conglomerate debris materials are associated with core components [3]and treated as coherent mixtures. Material pairs corresponding to material interactions treated by MELCOR become part of the conglomerate debris mixture by one of three processes: (1) intact solid components reach their melting point, (2) two intact solid components in mechanical

[3] Core components are MELCOR modeling objects for the different types of structures and debris found in a reactor core (e.g. fuel, supporting structure, particulate debris, etc.)

contact reach their eutectic temperature, or (3) dissolution of intact solid components by a liquid mixture.

Eutectic Reactions
MELCOR models two eutectic reactions that can lead to early failure of SSCs in BWRs: the eutectic interaction between zirconium-based fuel cladding and inconel grid spacers (ZR/INC); and the eutectic interaction between B4C and steel control rod cladding (SS/B4C). The ZR/INC reaction occurs at 1400 K by default and can cause early failure of fuel rods, while the SS/B4C occurs at 1520 K by default and can lead to early failure of the BWR control blades. Default reaction temperatures are defined to approximate the point when the reaction rate of material interactions between two contacting solids causes significant liquefaction. Molten material formed by these eutectic reactions becomes conglomerate debris associated with that component.

Composition-Dependent Mixture Properties
The simplified eutectics model has built-in capability to treat six pseudo-binary mixtures as surrogates for the complex, multi-component systems that may develop locally during severe accidents, shown in 0. The molar ratios and "eutectic temperature" of each material pair are derived from binary phase diagrams for each mixture.

Table 1. MELCOR Eutectics Model Binary Material Interaction Parameters

Material Pairs		Molar Ratio	Eutectic Temperature [K]
ZR	INC	0.76/0.24	1210
ZR	SS	0.76/0.24	1210
ZRO2	UO2	0.50/0.50	2450
ZR	B4C	0.43/0.57	1900
SS	B4C	0.69/0.31	1420
ZR	Silver-Indium-Cadmium (AGINC)	0.67/0.33	1470

When the eutectics model is active, the solidus temperature of a mixture is calculated as the mole-weighted combination of the solidus temperatures of every binary combination of material pairs in the mixture:

$$TS_{mix} = \frac{\sum_j \sum_{i \neq j} f_i f_j TS_{ij}}{\sum_j \sum_{i \neq j} f_i f_j} \tag{7}$$

where f_i is the mole-fraction of the first constituent material, f_j is the mole-fraction of the second constituent material, and TS_{ij} is the solidus temperature for a mixture of materials *i* and *j* with the same relative proportions as the total mixture. Currently, TS_{ij} is obtained from either mole-weighting of each constituent material solidus temperature or one of six pseudo-binary phase diagrams shown in 0. For the material pairs in 0, the solidus temperature of a mixture is treated as mole-weighted average of the eutectic temperature and solidus temperature of the constituent in excess of the eutectic composition:

$$T_{solidus}^{mix} = f_{eutectic}\, T_{eutectic} + f_{excess}\, T_{solidus}^{excess} \tag{8}$$

where $T_{solidus}^{mix}$ is the solidus temperature of the mixture, $f_{eutectic}$ is the mole-fraction of the primary constituent, $T_{eutectic}$ is the eutectic temperature of the mixture, f_{excess} is the mole-fraction of the constituent in excess ,and $T_{solidus}^{excess}$ is the solidus temperature of the constituent in excess

MELCOR does not perform Gibbs free energy minimization to evaluate the phase of material mixtures. The liquidus temperature of each component and the eutectic mixture are set to the solidus temperature plus 0.01 K. The specific enthalpy of the eutectic mixture is determined according to mixture temperature and phase. For mixture temperatures below the calculated solidus, weighted individual enthalpies are added together; extrapolated solid enthalpies are used for any constituent that would normally be liquid. At mixture temperatures greater than the calculated mixture liquidus, mass weighted individual enthalpies are added together; extrapolated liquid enthalpies are used for any constituent that would normally be solid. When mixture temperatures lie between the solidus and liquidus of a mixture, linear interpolation between the solidus and liquidus enthalpy is used. The latent heat of fusion for a eutectic mixture is taken as the difference between the liquid and solid enthalpy as determined by the mass weighted enthalpies. All other properties of formed mixtures are defined as the mass-weighted averages of constituent properties.

Chemical Dissolution of Solids

MELCOR has a built-in capability to treat the chemical dissolution of solids. The rate of dissolution is governed by parabolic kinetics using experimentally obtained rate constants. Currently, MELCOR only allows material mixtures to dissolve UO2 and ZRO2. UO2 and ZRO2 dissolution occurs only if the enthalpy of a molten mixture exceeds its liquidus enthalpy. Two limitations are employed by MELCOR on the chemical dissolution of UO2 and ZRO2: mixture enthalpy limits and parabolic rate limitations. The amount of dissolved material is first predicted by the parabolic rate reported by Hofmann, et al., 1989 [14]. This predicted mass is then used to calculate mixture enthalpy to ensure conservation of energy. If the updated mixture enthalpy is too high, then the mass will be reduced until the updated mixture enthalpy is equal to the liquidus enthalpy of the updated mixture composition. Thus, the parabolic rate is treated as an upper bound for dissolution and is used for all mixtures, including mixtures with a low ZR content for which the predictions become more inaccurate. The parabolic rate limitation for UO2 and ZRO2 dissolution in MELCOR is implemented as[4]:

$$\left(x_j^f\right)^2 = \left(x_j^i\right)^2 + K_j\,\Delta t \tag{9}$$

where x_j^f is the mass fraction of material *j* at end of time step, x_j^i is the mass fraction of material *j* at start of time step, Δt is the timestep size, and K_j is the temperature dependent rate constant defined by the Arrhenius equation[5]:

$$K_j = A_j \exp\left(\frac{B_j}{T}\right) \tag{10}$$

MELCOR calculates K_j using the experimental correlations reported by Hofmann et al. [14] for all mixtures, regardless of composition. Application of the dissolution constants obtained

[4] Eq. 9 is a discretized form of the time and temperature dependent parabolic rate equation shown in Eq. 5.

[5] MELCOR accounts for the universal gas constant, R, from Eq. 6 in the values reported for B_j shown in 0.

experimentally by Hoffman et al., shown in 0, introduces error into the predicted dissolution rates as the Zr content decreases in the mixture. Furthermore, the dissolution models for UO_2 and ZrO_2 do not become active until after cladding failure.

Table 2. Parabolic Rate Constants by Material [2] [3]

Solid	$A_j \left[\frac{\text{wt.}\%^2}{\text{s}}\right]$	B_j [K]
ZrO_2	1.47×10^{14}	8.01×10^4
UO_2	1.02×10^{15}	8.14×10^4

2.1.2. MELCOR Interactive Materials Model

Until recently, the interactive materials model was used to capture the effects of material interactions by the MELCOR code. The interactive materials model captured the reduced melting points of core materials caused by material interactions by artificially lowering respective material liquefaction temperatures.

Interactive Materials
The material classes: ZRO2-INT, UO2-INT, and B4C-INT, with identical characteristics to the pure ZRO2, UO2, and B4C material classes, respectively, are available to users with the added option to modify liquefaction temperatures thereby approximating the effect of materials interactions on material phase changes during core degradation. Other material properties available to user-modification as part of the interactive materials model include thermal conductivity, density, and latent heat of fusion. Modifications to the ZRO2-INT, UO2-INT, and B4C-INT material classes are global and are not composition dependent – intact UO2-INT, ZRO2-INT, and B4C-INT materials melt at their reduced liquefaction temperatures without consideration of the availability of other interacting materials or liquids.

Secondary Material Transport
When the interactive materials model is activated, the secondary material transport model is also enabled. This model allows the transport of unmolten secondary materials by candling molten materials to simulate both the dissolution of UO2 by molten ZR and the oxide shell debris that is carried with candling materials. Two mechanisms of transport are possible using the secondary material transport model. The first option transports a mass of unmolten material defined as a fraction of the candling molten mass:

$$\Delta M_s = F_1 \, \Delta M_m \tag{11}$$

the second option transports an amount of unmolten material equal to a fractional proportion of its existing fraction within a component:

$$\Delta M_s = F_2 \frac{M_{s,total}}{M_{m,total}} \, \Delta M_m \tag{12}$$

where F_1 is the input fraction of the candling molten mass, $F_2$is the fraction of proportional relocation, M_s is the unmolten secondary material, M_m is the candling molten mass refrozen (deposited) on a component, $M_{s,total}$ is the total unmolten secondary material mass in the component in the cell of origin, and $M_{m,total}$ is the total material mass in the cell of origin. The secondary material transport model is inactive if the eutectics model is activated.

2.2. Plant Representation

The foundation of the plant model featured in this analysis is the Peach Bottom Nuclear Power Plant (1180 MW(e) BWR/4 reactor, Mk-I containment) model maintained by Sandia National Laboratories (SNL) for the USNRC, which was used in the State of the Art Reactor Consequence Analysis (SOARCA) Peach Bottom Analysis project [16] [17]. Post-Fukushima, a version of the Peach Bottom Nuclear Power plant model was modified by SNL to incorporate accurate design characteristics of the Fukushima Daiichi Unit 1 nuclear reactor (1380 MW(th) BWR/3 reactor, Mk-I containment) – plant characteristics from the model are shown in 0 – and used in the Organisation for Economic Cooperation and Development Nuclear Energy Agency (OECD/NEA) Benchmark Study of the Accident at the Fukushima Daiichi Nuclear Power Plant (BSAF) project [18]. In this analysis, boundary conditions representative of the Fukushima Daiichi Unit 1 accident (1F1) that were used during the BSAF project have been preserved and are outlined below. The primary purpose of this analysis is not to reconstruct the severe accident at Fukushima Daiichi Unit 1, but to compare the effect of material interaction models available to MELCOR users on the progression of core degradation and overall plant states. To that end, changes have been made to the plant model that do not necessarily reflect the 1F1.

Table 3. BWR/3 Reactor Model Parameters

Plant Parameter	Value
Rated Core Power [MW_{th}]	1380
Total RPV water inventory [kg]	147634
Number of fuel assemblies [#]	400
Number of control blades [#]	97
Total mass of UO_2 [kg]	77403
Total mass of zircaloy [kg]	30431
Total mass of stainless steel [kg]	47767
Total mass of B_4C [kg]	540
Mass of active region zircaloy cladding [kg]	16779
Mass of upper core, non-active region zircaloy cladding [kg]	2202
Mass of lower core, non-active region zircaloy cladding [kg]	0
Mass of zircaloy in fuel canister [kg]	11451
Mass of stainless steel in control blades [kg]	9000
Mass of stainless steel in top guide tube and upper tie plate [kg]	4420
Mass of stainless steel in core support plate and other stainless steel support structures [kg]	8880
Mass of lower plenum stainless steel support structures [kg]	25467

The nodalization scheme of the plant remains unchanged from the BSAF project [18]. Thermal hydraulic phenomena are modeled in 26 separate control volumes representing the lower plenum and core region, while core degradation phenomena are captured in 88 core cells. The Mark I containment building is discretized into six control volumes and the drywell floor is divided into three regions where debris can accumulate and interact with the concrete floor during molten core concrete interaction (MCCI). The reactor building is discretized into 14 control volumes. More information on the plant nodalization scheme can be found in references [19] (RPV nodalization) and [20] (containment nodalization).

2.2.1. Plant Model Parameters

For the present analysis, the number of safety relief valves (SRVs) operating during the accident sequence has been increased from one to four to accurately represent SRV behavior. Changing the number of safety relief valves operating during the simulation alters the behavior of energy transfer from the primary system to containment including distributing energy rejected from the primary system across four main steam lines (dependent on predicted SRV behavior). Each SRV operates based on its separate pressure setpoints that, in turn, depend on the availability of power. Core degradation forcing functions (e.g. core ring failures, lower head failure, etc.) were used by analysts during BSAF to simulate a forensic reconstruction of key accident signatures observed during 1F1. Such forcing functions have been removed from the plant model, to allow core degradation to proceed according to built-in MELCOR models. By using built-in MELCOR models, a more complete comparison can be made between the eutectic and interactive materials models' effects on core damage progression as predicted by MELCOR. Furthermore, it removes user bias based on interpretation of the observations recorded during 1F1, changing the plant model from a forensic reconstruction to an accident scenario under representative boundary conditions. In this analysis, the default time-at-temperature fuel rod failure model, described in greater detail in part II of this analysis, is activated [21].

2.2.2. Scenario Assumptions

Representative boundary conditions are preserved from the 1F1 plant model for the BSAF project and are shown in 0. As in the BSAF study for 1F1, gross creep failure of the lower head is assumed, and penetration failures are disabled. The decay heat and FP inventory boundary conditions used in this analysis are the same as those used in the BSAF plant model [22]. Four periods of operation of the two train (A and B) isolation condenser (IC) are assumed. IC activity takes place from 0.10-0.28 hours for trains A and B, 0.52-0.55 hours for train A, 0.63-0.67 hours for train A, and 0.77-0.80 hours for train A. Each IC train is assumed to remove heat equal to 42.4 MW per train for the duration of operation. Minimal water injection is modeled during the first 25 hours of the scenario. A rapid linear increase in flow occurs between 9.20 and 9.21 hours from 0.0 kg/s to a maximum flow rate of 0.36 kg/s. The maximum allowable flow rate continues at 0.36 kg/s through the scenario, which is scaled based on the steam dome pressure. No flow is assumed when steam dome pressure is above 1.10 MPa, and maximum flow is assumed when steam dome pressure is 0.60 MPa. Injected water is assumed to reach the lower plenum until lower head failure occurs. After lower head failure, water is injected directly into the drywell cavity. Recirculation pump leakage to the drywell of the containment is assumed (approximately 10 gallons/min). Drywell head flange leakage from the containment drywell to the undershield plug is also assumed to occur starting at 0.648 MPa. Wetwell Venting at 23.7 hours and a reactor building explosion at 24.8 hours are also assumed.

Table 4. Boundary Conditions

Boundary Condition	Description
SRV Seizure	Not permitted
SRV Gasket Leak	Not permitted
Main Steam Line Rupture	Not permitted
Lower Head Gross Creep Failure	Permitted
Lower Head Penetration Failure	Not permitted
Drywell Head Flange leakage	Begins at 0.6481 MPa pressure in the drywell
Main Steam Line Isolation Valve Closure	At 0.0 hours
Feedwater System Ceases Operation	At 0.0 hours
IC Train A Operation	0.1-0.28 hours 0.52-0.55 hours 0.63-0.67 hours 0.77-0.8 hours
IC Train B Operation	0.1-0.28 hours
Wetwell Venting	At 23.7 hours
Reactor Building Explosion	At 24.8 hours

2.3. Comparison Methodology

In part I of this benchmark, baseline model behavior is examined through single case, best-estimate simulations using the interactive materials model and the eutectics model. Nominal values are used in both models for uncertain parameters (e.g. zirconium breakout temperatures, core component failure temperatures, candling parameters, etc.). Uncertainties associated with these parameters are investigated in more detail in part II of this benchmark: Material Interactions in Severe Accidents - Benchmarking the MELCOR V2.2 Eutectics Model on a BWR with Representative Fukushima Daiichi Boundary Conditions: Part II - Uncertainty Analysis. In this analysis, ZRO2-INT and UO2-INT liquefaction temperatures are equal to the SOARCA mean value, 2479 K, for the interactive materials model simulation. Proper implementation of the interactive materials model requires that core component failure criteria be set equal to the same temperature to properly fail core structures. The single case, best-estimate simulations are analyzed and compared according to a similar methodology presented in the Modular Accident Analysis Program (MAAP)-MELCOR Crosswalk [23].

First, the overall accident progression is described in detail. This includes comparison of key accident signatures for each simulation. Key accident signatures are defined in this study as event timings indicative of deteriorating conditions in the core including decreasing water level, FPB failure, transitions between core damage states/accident phases, etc. Core energy functions are also compared to provide insight into dominant modes of energy production and loss, and their implications on core debris morphology.

Second, a comparison of hydrogen generation between the two simulations is made. Hydrogen is a highly combustible gas generated by the oxidation of core materials. Differences in the accident progression between the two simulations affect the available inventory of oxidant and the surface area exposed to the oxidant.

Next, a comparison is made of the thermal hydraulic response in both the primary system and containment. RPV water level, pressures, and temperatures in the primary system and containment provide additional context to the accident progression outlined in section 3.1 and the conditions in the primary system during peak in-core hydrogen production.

Finally, the fourth and fifth elements of this comparison – reactor core degradation and reactor pressure vessel lower head breach – interrogate the implications of both the interactive materials and eutectics models effects on core component degradation and failure, debris formation and morphology, and other aspects of in-vessel debris evolution. Figures of merit include intact component temperatures and mass fractions; core melt progression; debris morphology, distribution, and temperature; thermal challenge to the lower head; and ejected debris masses.

3. RESULTS AND DISCUSSION

The following section details an in-depth comparison between the interactive materials model and eutectics model simulated plant behavior. Plots have been annotated with vertical bands of blue, white, and red from left to right to illustrate the early in-vessel (up to the initial loss of rod-like geometry – defined in this study as the onset of candling), late in-vessel (up to initial lower head failure), and ex-vessel phases of each respective simulation. Results deviating from this format are explained as they are introduced. Interactive materials (e.g. ZRO2-INT) are denoted, in this section, an "-interactive" suffix.

3.1. Overall Accident Progression

A comparison of key event timings from a single simulation for each respective model are shown in 0. Strong agreement is observed in timings of early in-vessel phase events (e.g. core boiloff from top of active fuel (TAF) to bottom of active fuel (BAF)); time differences in the occurrence of all core boiloff phenomena are less than or equal to two minutes. Initial gap release occurs at 3.45 hours in both simulations, after significant core boiloff has occurred, the core is less than 1/3 uncovered, during the early in-vessel accident phase. Strong agreement between simulations is typical for severe accident codes during the early in-vessel phase of accident progression in perturbation and sensitivity studies; the result of strong validation of relevant models, and limited degrees of freedom.

Table 5. Key Event Timings

Event	Interactive Materials model [h]	Eutectics Model [h]
Core Water Level at TAF	2.54	2.56
Core Water Level at 2/3 TAF	2.88	2.89
Core Water Level at 1/3 TAF	3.19	3.19
Core Water Level at BAF	4.00	3.97
Initial Gap Release	3.45	3.45
Initial Candling in Ring 1	3.69	3.64
Initial Particulate Debris Formation	3.64	3.70

Initial Core Plate Failure	5.05	5.01
Core Slump	5.25	5.01
Lower Plenum Dryout	7.56	6.36
Initial RPV Failure	10.72	8.34

Late in-vessel phase events included in 0, show strong agreement initially, but local differences are observed to evolve into large temporal differences in the occurrence of lower plenum dryout and initial RPV failure. This observation is also confirmed in Figure 3, which shows core degradation maps at various times in the scenario. Such differences in accident progression are a byproduct of increasing degrees of freedom that occurs by the introduction of previously inactive and/or nonexistent physical and phenomenological connections between core components and materials, i.e. late in-vessel phase severe accident phenomena and relocation of core materials. The onset of the late in-vessel accident phase is observed to occur at 3.64 hours, approximately three minutes earlier in the eutectics model simulation. It is noteworthy to observe that the occurrence of initial candling in ring 1 (the centermost core ring) and initial particulate debris formation are reversed between the two simulations. The eutectics model exhibits candling before particulate debris formation, whereas the interactive materials model simulation exhibits the opposite. These degradation pathways, candling and particulate debris formation, correspond to distinct debris relocation characteristics discussed in greater detail in part II of this analysis. Shortly after the onset of the late in-vessel phase, at four hours, accelerated degradation of core structures is observed (discussed in greater detail in section 3.4), as shown in Figure 3(b).

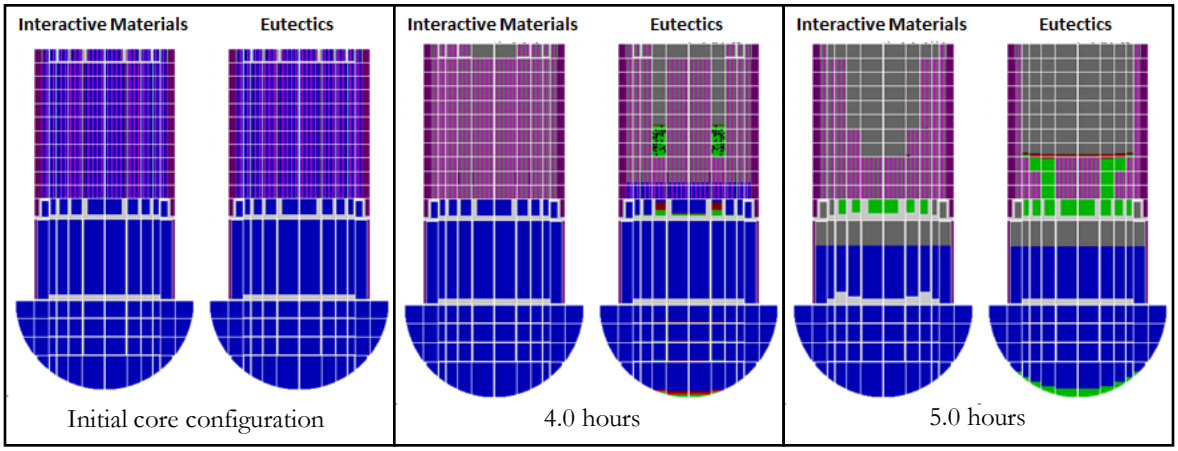

(a) (b) (c)

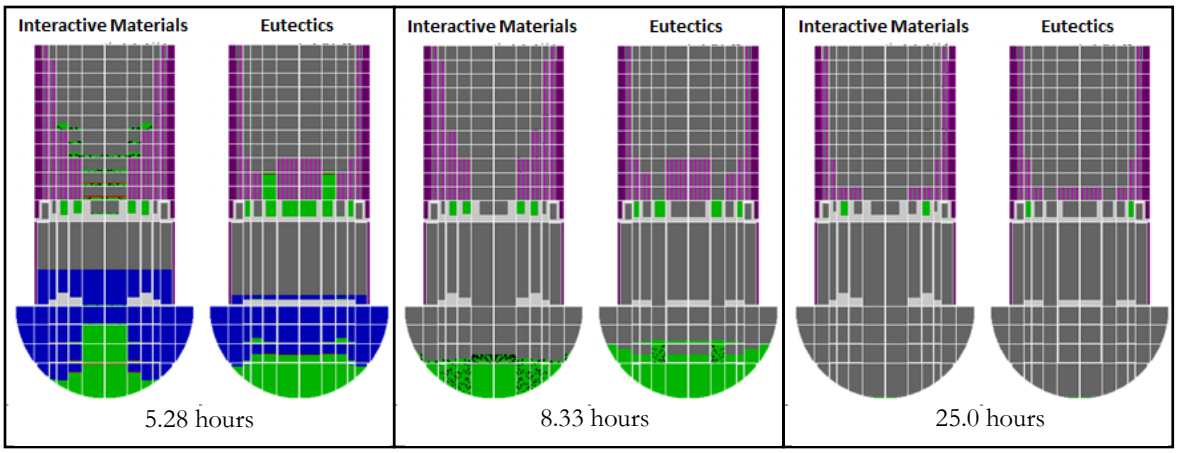

Figure 3. Core degradation maps over 25 hours (a) initial core configuration, (b) 4.0 hours core degradation map, (c) 5.0 hours core degradation map just before core plate failure, (d) 5.28 hours core degradation map after core slumping has occured, (e) 8.33 hours core degradation map just before lower head failure in the eutecitcs model simulation, (f) 25 hours core degradation map

Core plate failure marks a major transition within the late in-vessel accident phase, creating a pathway for massive debris relocation to the lower plenum. In both simulations, core plate failure is observed to occur just after five hours (Figure 3(c)); the eutectics model simulation exhibits core plate failure 3 minutes earlier than the interactive materials model simulation. The eutectics model simulation exhibits core slumping, defined as relocation of 20% of the initial fuel mass to the lower plenum, at the same time as core plate failure. Conversely, the interactive materials model simulation exhibits a 12 minute delay between core plate failure and core slumping. The core degradation map after core slumping in both simulations is shown in Figure 3(d). Debris accumulation in the lower plenum boils the remaining water inventory. Lower plenum dryout occurs at 6.36 hours, approximately 1.5 hours after core plate failure, for the eutectics model simulation. The interactive materials model simulation exhibits delayed lower plenum dryout, approximately 1.2 hours longer, at 7.56 hours. Figure 3(e) shows that the eutectics model exhibits more complete destruction of core structures at 8.33 hours, just before lower head failure in the eutectics model.The eutectics model exhibits lower head failure at 8.34 hours, 2.38 hours before the interactive materials model simulation, which exhibits lower head failure at 10.72 hours. Key accident signatures are consistently simulated to occur at later times for the interactive materials model simulation when compared to the same accident signatures simulated by the eutectics model simulation. Figure 3(f) shows that after 25.0 hours, both simulations exhibit comparable core damage.

3.2. Hydrogen Generation

The amount of energy released by the oxidation of core materials is proportional to the amount of hydrogen liberated; ~6.5 MJ are released per kg of hydrogen generated. Figures of merit corresponding to hydrogen generation for each simulation are illustrated in Figure 4 and Figure 5, which show the distribution of hydrogen generation by material and radial location, respectively.

It is observed in Figure 4, that hydrogen is generated primarily by the oxidation of zirconium-based structures (fuel cladding and canister wall), while minimal hydrogen is produced by B_4C reactions. Similar quantities of hydrogen are produced by B_4C reactions in both simulations. The interactive

materials model simulation, however, exhibits greater hydrogen generation from the oxidation of both stainless steel and zirconium-based structures than the eutectics model simulation. As discussed in sections 3.1 and 3.4, the eutectics model simulation exhibits earlier failure of core components, including fuel and cladding components. Conversely, in the interactive materials model simulation, components remain above the core plate, in an oxidizing steam environment, for a longer period of time. In other words, earlier relocation of large quantities of debris to the lower plenum, as observed in the eutectics model simulation, limits the degree of oxidation of core materials that can take place. At the end of the simulation, 25 hours, the interactive materials model exhibits 761 kg of hydrogen, about 145 kg more than the eutectics model simulation's 615.7 kg of hydrogen.

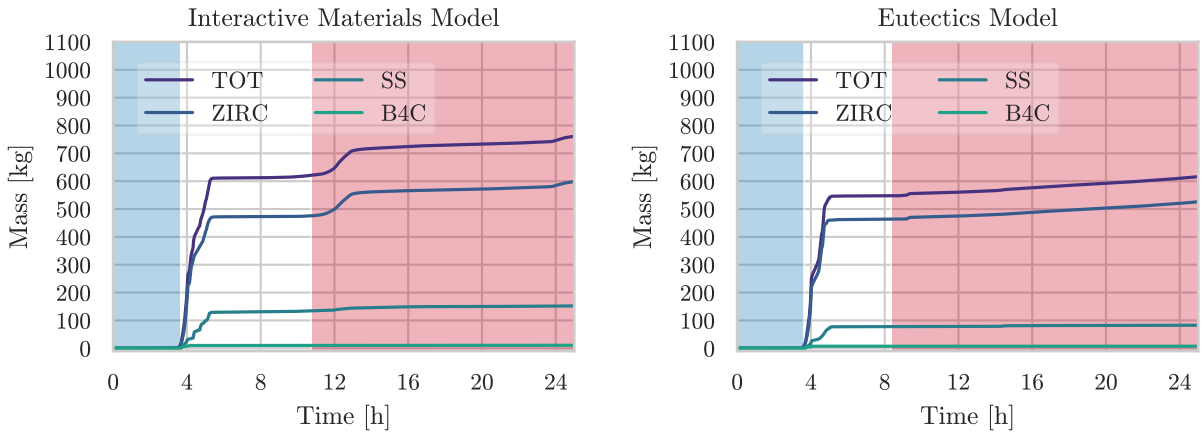

Figure 4. Comparison of hydrogen generation by material.

For both the interactive materials model simulation and the eutectics model simulation, hydrogen production begins in the innermost rings (1, 2, and 3) at nearly the same time, followed by ring 4, and finally ring 5 as shown in Figure 5. For the interactive materials model simulation, the majority of hydrogen production occurs between (3.5-6 hours) during core and lower plenum boiloff. The primary hydrogen generating transient occurs in the eutectics model simulation during the same time period. At 25.0 hours, the interactive materials model simulation exhibits between 13 kg and 56 kg more hydrogen generation in each core ring in comparison to the eutectics model simulation. This observation is consistent with earlier observations that core components, fuel components in particular, remain intact for longer periods in the interactive materials model simulation. The greatest differences in hydrogen generation are observed in rings 2 and 5. In ring 2, fuel and cladding components are observed to completely fail before 5 hours in the eutectics model simulation, preventing continued oxidation of those materials. In ring 5, the interactive materials model simulation exhibits elevated core temperatures, in excess of 1500 K, promoting greater hydrogen generation.

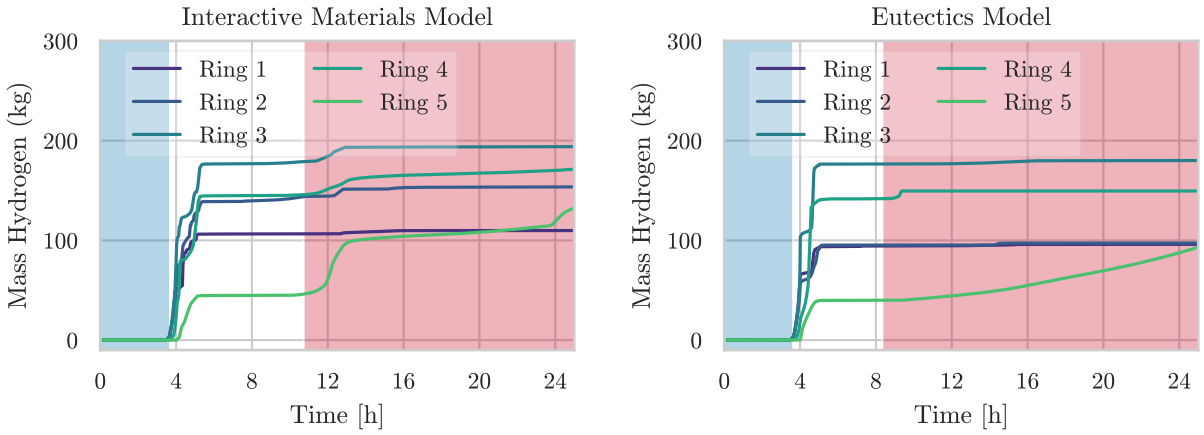

Figure 5. Comparison of hydrogen generation distribution.

3.3. Thermal Hydraulic Response

3.3.1. Primary Coolant System Response

The RPV steam dome pressure transient for each simulation is shown in Figure 6. An initial decrease in steam dome pressure is observed at the beginning of both simulations (0.0 - 0.28 hours) when both IC trains are operating. After IC train B ceases operation at 0.28 hours, however, RPV steam dome pressure increases to the SRV opening setpoints. At 0.8 hours, IC train A shuts off for the remaining duration of the accident scenario and no further core cooling is provided by either train of the IC system. SRV cycling continues through the early and late in-vessel phases of the accident until primary system depressurization by lower head failure in both models; for approximately 9.9 hours in the interactive materials model simulation, and 7.5 hours in the eutectics model simulation. The interactive materials model simulation exhibits less frequent SRV cycling after lower plenum and downcomer dryout, but prior to lower head failure, due to steam starvation and the lack of coolant inventory available to vaporize. The same behavior is not observed in the eutectics model simulation because downcomer dryout does not occur before lower head failure. After lower head failure, primary system pressure follows closely that of containment pressure in both simulations.

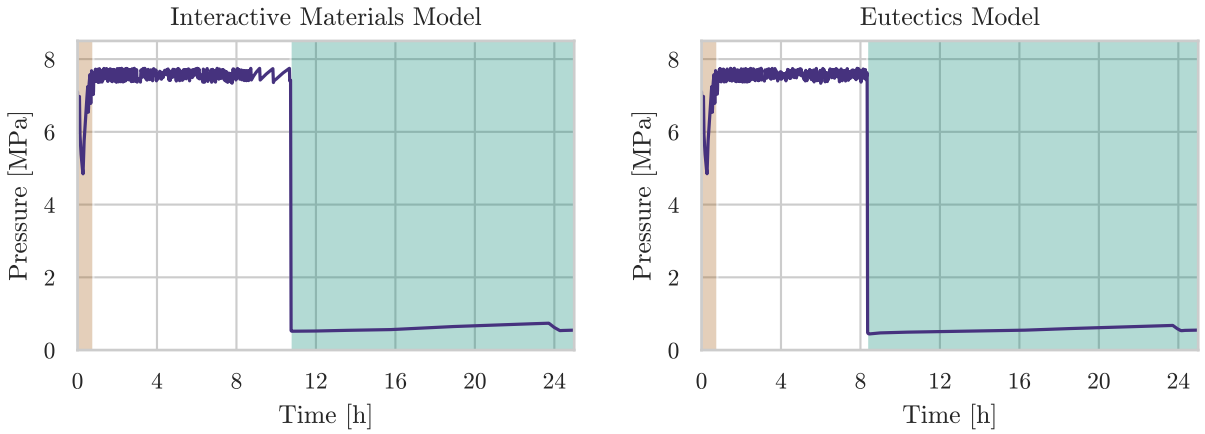

Figure 6. Comparison of the RPV pressure transient. Vertical bands highlight periods of IC operation (0.0-0.8 hours), sustained SRV cycling (~0.8 - lower head failure), and post-lower head failure (lower head failure - 25 hours), respectively.

Figure 7 shows the temperature transient in the RPV steam dome. Near the end of the early in-vessel phase, steam dome temperatures begin to rise due to core uncovery and associated steam production. Shortly after the onset of the late in-vessel phase, at approximately 4.0 hours, both models exhibit rapidly rising temperatures in the steam dome, coincident with rapid hydrogen generation by highly exothermic oxidation of core materials by steam. The rapid rise in steam dome temperature is interrupted when the RPV water level drops below BAF due to a decrease in the steam production, as shown in Figure 8. Both simulations exhibit a second peak in steam dome temperatures coincident with renewed oxidation of core materials by steam associated with lower plenum boiloff. Lower plenum boiloff begins after core plate failure for interactive materials model simulation. Conversely, the eutectics model simulation exhibits renewed lower plenum boiloff and increasing steam dome temperatures in combination with debris relocation to the lower plenum (discussed in section 3.5) prior to core plate failure. After lower plenum boiloff has occurred, steam dome temperatures are observed to increase in a pseudo-linear fashion in both simulations, with small features corresponding to debris relocation and SRV activation, until lower head failure. After an initial, sharp decrease in steam dome temperature coincident with lower head failure, steam dome temperatures increase as remaining core components, particularly in outer core rings, oxidize further. Peak steam dome temperatures observed for both simulations over the course of the transient occur during core slumping and are 1246 K for the interactive materials model simulation and 1123 K for the eutectics model simulation.

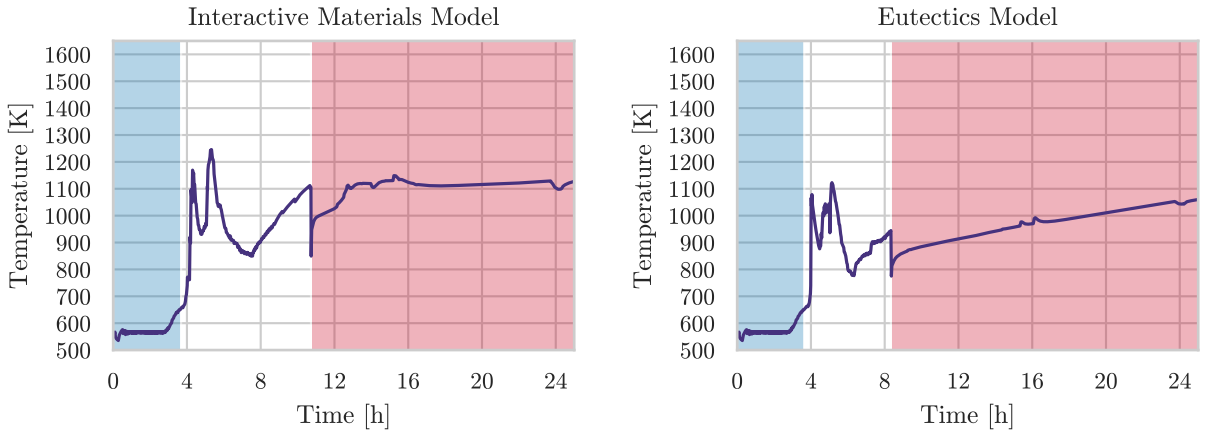

Figure 7. Comparison of the steam dome temperature transient.

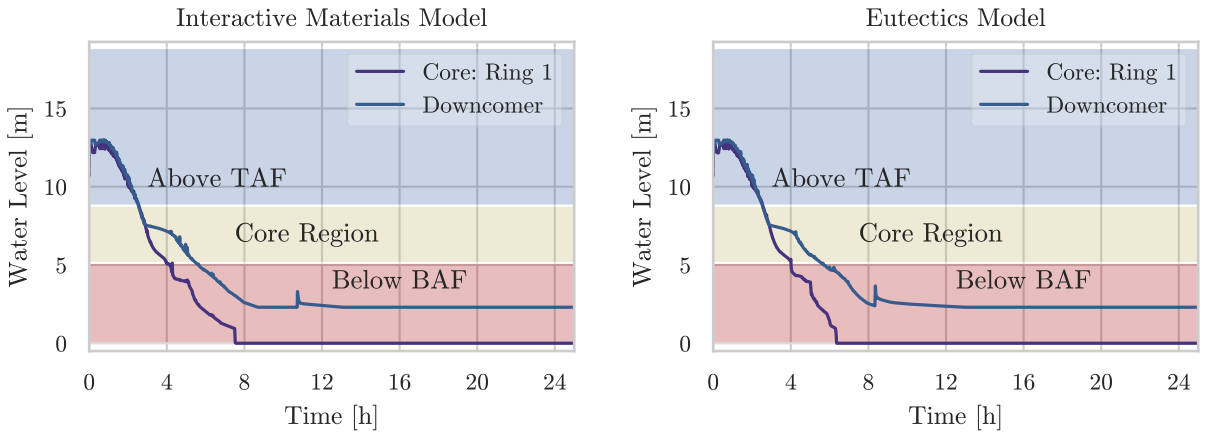

Figure 8. Comparison of the RPV water level transient.

RPV water level is shown in Figure 8. As with other figures of merit thus far considered, little difference is observed between the simulations until the late in-vessel phase begins, when the core water level is near the BAF. Lower plenum dryout occurs 2.51 hours after core plate failure for the interactive materials model simulation, and 1.35 hours after core plate failure for the eutectics model simulation. Lower plenum boiloff is observed to be more rapid in the eutectics model simulation because of more significant debris relocation to the lower plenum. In both simulations, downcomer water level trails core water level until the top of the jet pump is reached, at which point it decreases more slowly to the bottom of the jet pumps. Lower head failure causes a small peak in downcomer water levels in both simulations due the accompanying change in pressure.

3.3.2. Containment Response

Figure 9 and Figure 10 show pressures in the drywell and wetwell, respectively. In both simulations, the wetwell pressure follows very closely the drywell pressure. During the early in-vessel phase, SRV cycling has little effect on containment pressure because the steam is injected into the suppression pool, where it condenses. After the late in-vessel phase begins, near 4.0 hours in both simulations, drywell and wetwell pressures rise in response to the addition of noncondensable gases (NCGs); hydrogen that is generated rapidly in the core region in both simulations and is transported into

containment by SRV cycling. Both simulations exhibit a gradual increase in containment pressure after the termination of the hydrogen generating transient up until lower head failure. As can be seen in Figure 11, the suppression pool does not reach saturation temperatures in either simulation. In other words, the suppression pool does not boil. Thus, pressure changes in containment are driven by the transfer of hot noncondensable gases in the primary system to containment until lower head failure in both simulations.

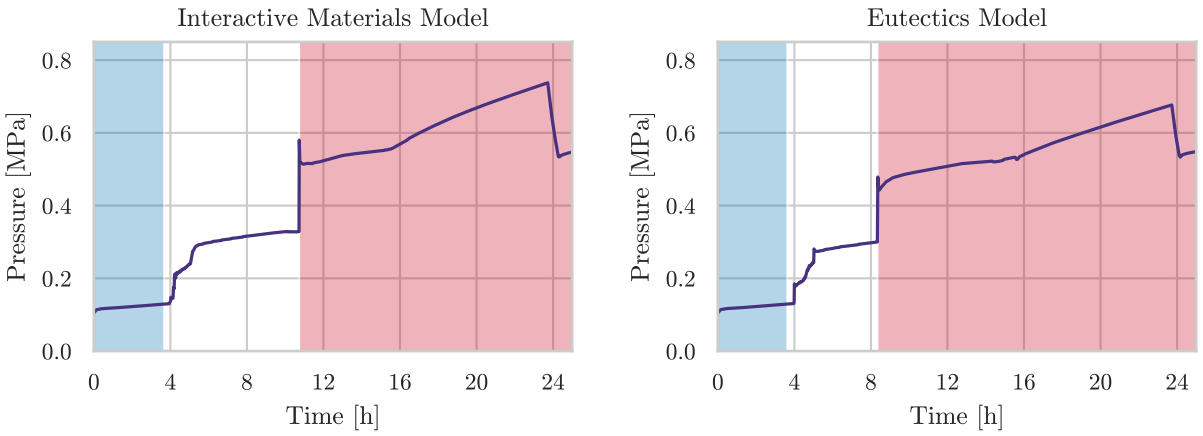

Figure 9. Comparison of the drywell pressure transient.

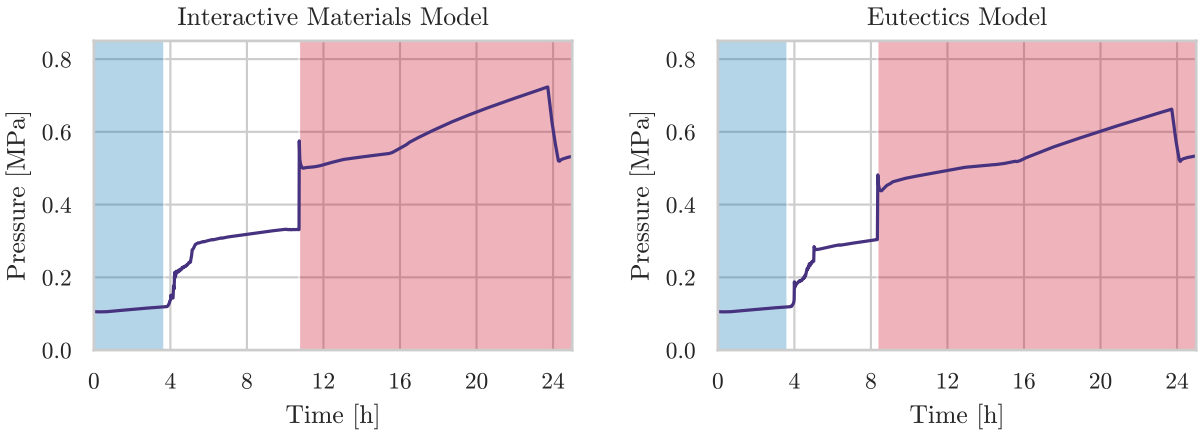

Figure 10. Comparison of the wetwell pressure transient.

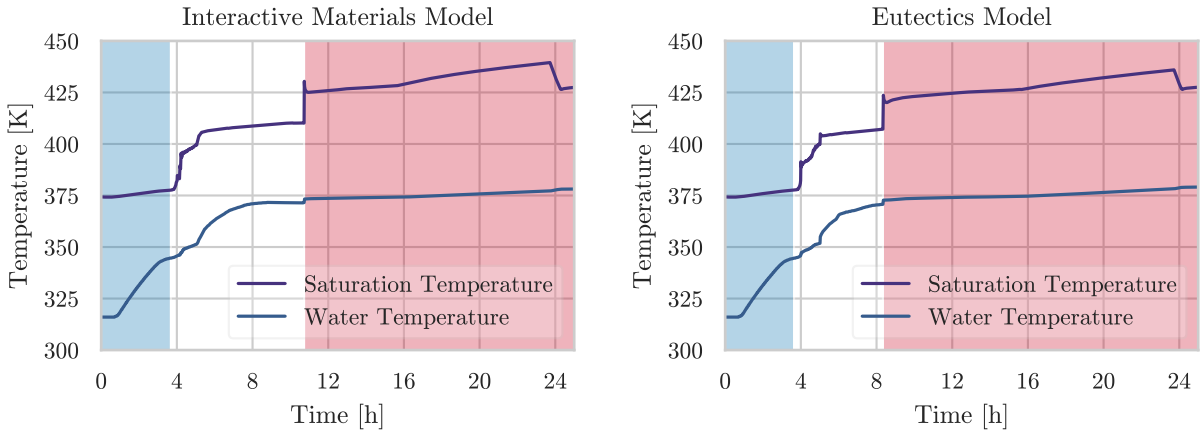

Figure 11. Comparison of the suppression pool temperature transient.

Lower head failure causes drastic pressurization of containment (> 0.15 MPa change) in both simulations due to the liberation of remaining inventories of NCGs and steam flashing of water from the primary system to containment. After the initial pressurization event, containment pressures are observed to decrease initially, likely as a result of steam condensation. In both simulations, containment pressures then continue to increase due to containment heatup and continued NCG production until containment venting at 23.7 hours.

3.4. Reactor Core Degradation

After the onset of the late in-vessel phase of core degradation begins, changes to core geometry and debris formation occurs quickly. Figure 12 shows the core melt progression for both simulations. Within the first hour of the late in-vessel phase, molten debris masses reach between 10-20 Mg for both simulations. Greater peak molten masses are observed in the eutectics model simulation in both the active core region and lower plenum region. Molten material is more persistent and masses are greater in the active core region than the lower plenum region for both simulations. By about 6 hours, the molten debris in both simulations has refrozen completely, and remains solid until lower head failure. After lower head failure, both simulations exhibit molten material formation in the active core region. The interactive materials model exhibits the formation of a small, persistent mass of molten material shortly after lower head failure that remains until the end of the accident scenario at 25 hours. The maximum mass attained by the molten material is 2.0 Mg, which decreases to >0.2 Mg near 16 hours. Conversely, a single, short-lived instance of molten material formation in the active core region is observed after lower head failure for the eutectics model simulation.

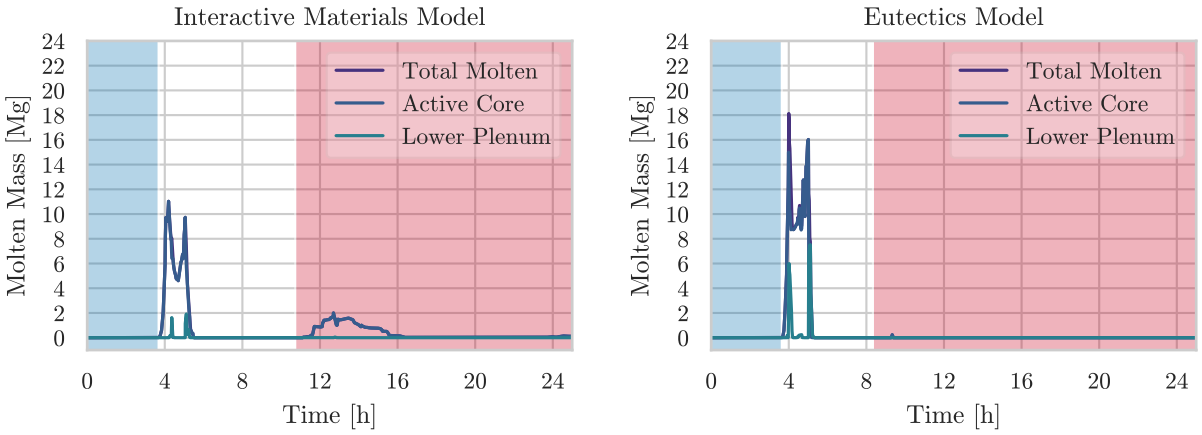

Figure 12. Comparison of the core melting progression.

Molten pools form when core debris is blocked from relocating further downward in the core, and temperatures exceed material melting points. Figure 13 shows the minimum axial flow area in each core ring. Each instance of large molten material masses coincides with decreased axial flow area. In particular, maximum molten material masses coincide with complete blockages of one or more core rings. When a blockage forms, coolant can no longer move through a core ring, and energy is no longer convected away from the debris, promoting molten material formation. Normalized axial flow areas can exceed 1.0 when intact core components fail, increasing the axial flow area beyond its original value. The interactive materials model simulation exhibits persistent blockages in rings 2-5, whereas the eutectics model simulations only exhibits a persistent blockage in rings 4 and 5. Reduction of axial flow area can be the result of either buildup of particulate debris or flow path occlusion by candled materials. For example, the flow area reduction in rings 2 and 3 observed during the ex-vessel phase of the interactive materials model simulation are coincident with particulate debris buildup in the active core region (not shown). Furthermore, both simulations exhibit axial flow areas that increase beyond the original value. For the interactive materials model simulation, the axial flow area is increased beyond the original value only in ring 1. Conversely, the eutectics model exhibits increased axial flow areas in rings 1-3. The effects of reduced axial flow are also observed in the hydrogen generation and the steam dome temperature transients in Figure 5 and Figure 7, respectively.

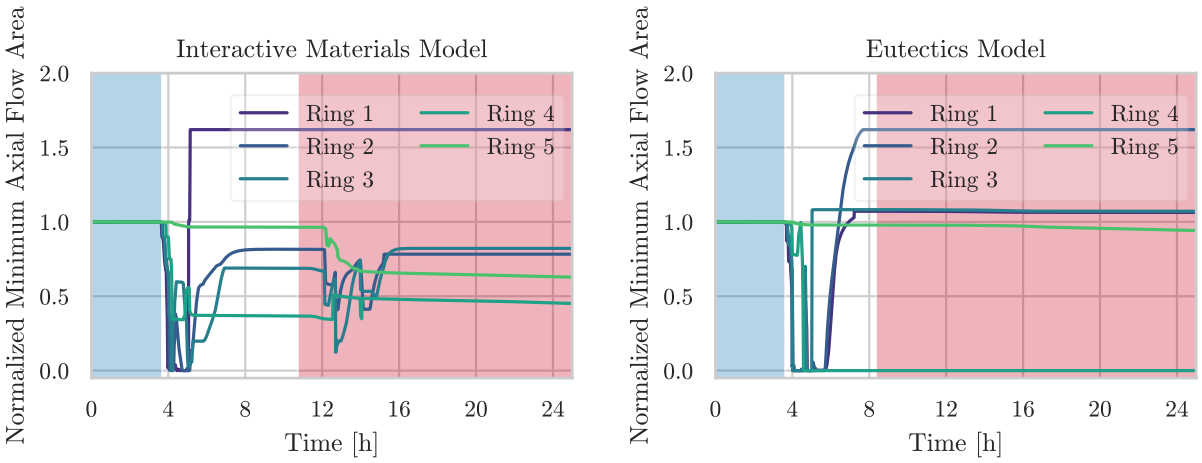

Figure 13. Comparison of the minimum axial flow area through the active core region.

Control rod poison (CRP) structure temperature transients and intact mass fractions are shown in Figure 14 and Figure 15, respectively. Early, complete destruction of CRP structures are observed in rings 1-4 by 5 hours for both simulations. After lower head failure, CRP structures are observed to fail in ring 5 for the interactive materials model simulation, but not in the eutectics model simulation. The temperature of B_4C in all core cells containing intact CRP structures[6] are shown in Figure 14. Both simulations exhibit CRP heat-up beginning in the early in-vessel phase to each respective B_4C /stainless steel parametric failure temperature; 1520 K for the interactive materials model simulation and 1700 K for the eutectics model simulation. Standard practice to capture the B_4C /stainless steel interaction in CRP structures when using the interactive materials model is to fail those components parametrically at the eutectic temperature (1520 K). Conversely, the eutectics model captures the B_4C /stainless steel interaction only after component temperatures exceed the eutectic temperature; thus, the parametric failure temperature is set above the eutectic temperature at 1700 K in this analysis. Figure 15 shows the corresponding degradation of CRP structures. Both simulations exhibit complete destruction of CRP structures in rings 1-4 and 10% degradation of structures in ring 5 by 5 hours. In the interactive materials model simulation, CRP structures remaining in ring 5 have failed by 13 hours, coincident with significant hydrogen production by oxidation of Zr-based structures in ring 5. For the eutectics model simulation, no degradation of ring 5 CRP structures is observed after 5 hours.

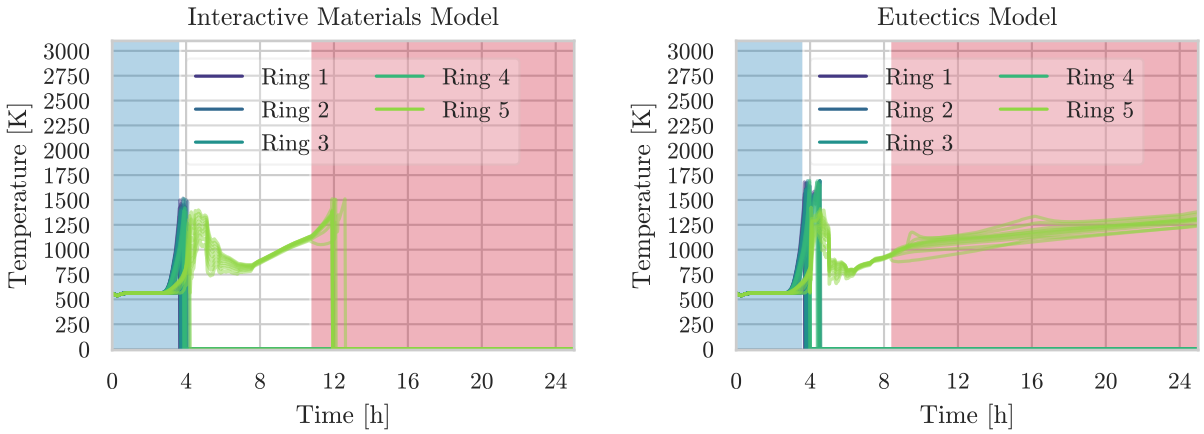

Figure 14. Comparison of control blade poison temperatures.

[6] When an intact component has a mass of 0.0 kg in MELCOR (i.e. the component has failed or was initialized without mass), that component temperature is set equal to 0.0 K.

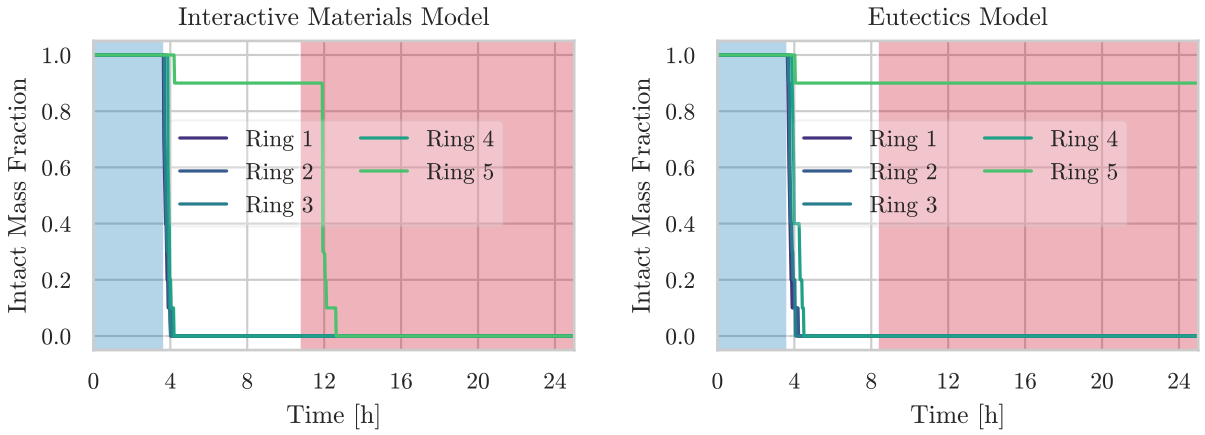

Figure 15. Comparison of control blade damage progression.

Fuel canister temperatures for both models exhibit similar qualitative behavior to CRP temperatures and are shown in Figure 16. Rapid heat-up is observed at the end of the early in-vessel phase during core boiloff reaching parametric failure temperatures of 2100 K (Zr melting point) by 5 hours. After rapid heatup and degradation, during lower plenum boiloff, remaining fuel canister components undergo significant cooling. Fuel canister temperatures decrease to between 650 K and 1000 K, with the eutectics model simulation exhibiting lower temperatures than the interactive materials model simulation. Following lower plenum dryout, fuel canister temperatures rise in both simulations. The second period of fuel canister heatup is more significant for the interactive materials model simulation, with some fuel canister components reaching the failure temperature setpoint around 12 hours due to increased exothermic oxidation of Zr-based components in ring 5. The eutectics model simulation does not exhibit fuel canister heatup beyond 1500 K, or any further failure of fuel canister components. Fuel canisters, a zirconium-based structure, are highly impacted by elevated temperatures because of the potential for runaway zirconium oxidation.

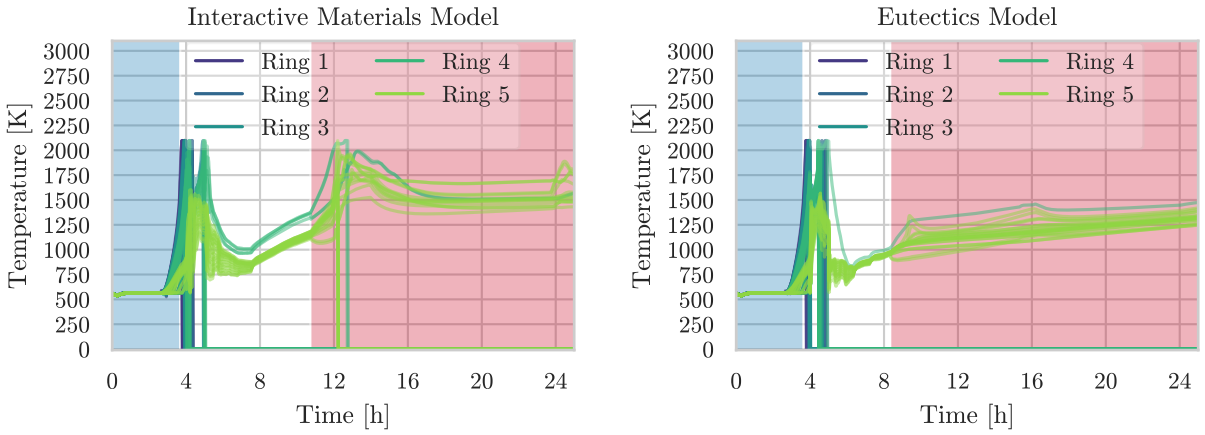

Figure 16. Comparison of fuel canister temperatures.

Complete destruction of fuel canister components in rings 1-3 is observed by 5 hours in both simulations. As temperatures rise towards the end of the late in-vessel phase and into the ex-vessel phase, further degradation of remaining fuel canister components is observed. Figure 17 shows that

shortly after 5 hours, the interactive materials model still has intact components remaining in rings 4 and 5; 15% intact and 91% intact, respectively. For the eutectics model simulation, intact components are also remaining in rings 4 and 5; 5% intact and 92% intact, respectively. Near 12 hours, the interactive materials model simulation exhibits a reduction of intact mass by oxidation in rings 4 and 5. Further reduction of intact fuel canister mass through oxidation is also observed in ring 5 during the ex-vessel phase for the eutectics model simulation, but to a lesser extent. After 25 hours intact mass remains in rings 4 and 5 for both simulations. In ring 4, 5% of the original mass remains intact, while for ring 5, the interactive materials model shows significantly more degradation, 35%, than the eutectics model simulation, 77%.

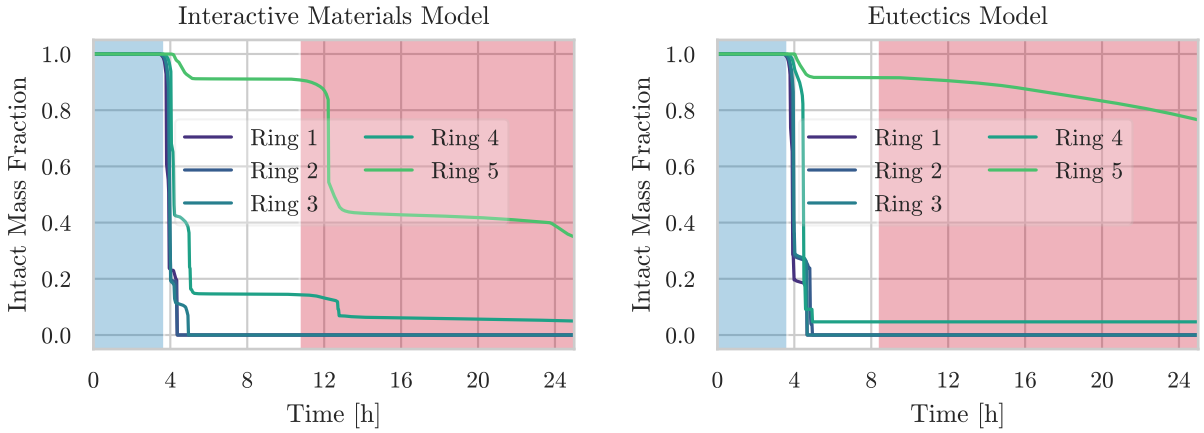

Figure 17. Comparison of fuel canister damage progression.

The fuel cladding, also zirconium-based, exhibits a similar initial heat-up profile in both simulations, as shown in Figure 18. Contrary to the observed fuel canister behavior, unoxidized zirconium in the cladding superheats in excess of its melting point due to holdup by the oxide scale formed during cladding oxidation. Furthermore, a larger number of fuel cladding components remain standing after 5 hours in both simulations. Peak fuel cladding temperatures reach 2478.6 K in the interactive materials model simulation – the modified liquefaction temperature of UO_2-interactive and ZrO_2-interactive is set to 2479 K – and 2712.1 K in the eutectics model simulation during the late in-vessel phase. As with other core components, fuel cladding temperatures decrease during lower plenum boiloff. After lower plenum boiloff, temperatures increase steadily until lower head failure. During the ex-vessel phase of the accident, fuel cladding heat-up is observed to accelerate in multiple core cells, peaking between 2300 K and 2400 K in both simulations. Fuel cladding failures are also observed during the ex-vessel phase, at between 12 and 14 hours for the interactive materials model simulation and near 16 hours for the eutectics model simulation.

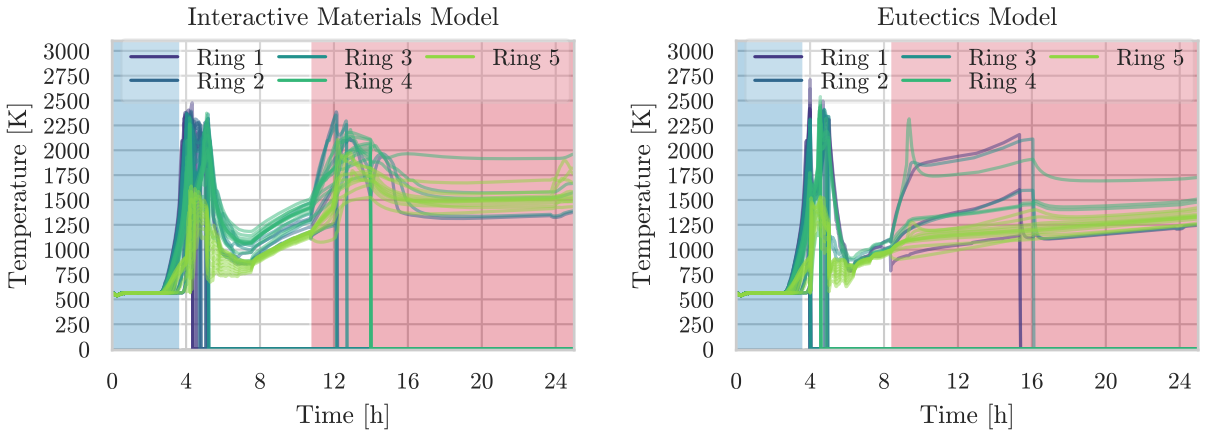

Figure 18. Comparison of fuel cladding temperatures.

Figure 19 shows the intact mass fractions for fuel cladding components in each ring of both simulations. Only partial degradation of the fuel cladding in rings 2-5 occurs in the interactive materials model simulation. At 5.5 hours, complete destruction of ring 1 cladding components has occurred in the interactive materials model simulation. Partial degradation in rings 2, 3, 4, and 5 has occurred, with 12%, 21%, 17%, and 85% remaining intact, respectively. After 25 hours, the same intact mass fractions have decreased to 12%, 12%, 13%, and 51%. Degradation of the fuel cladding is more significant for the eutectics model simulation In the eutectics model simulation, complete destruction of ring 2 cladding components has occurred by 5.5 hours. At the same time, 2%, 3%, 17%, and 86% of the original mass of Zr remains intact in rings 1, 3, 4, and 5. At 25 hours, remaining intact mass fractions are 1%, 1%, 11%, and 62%.

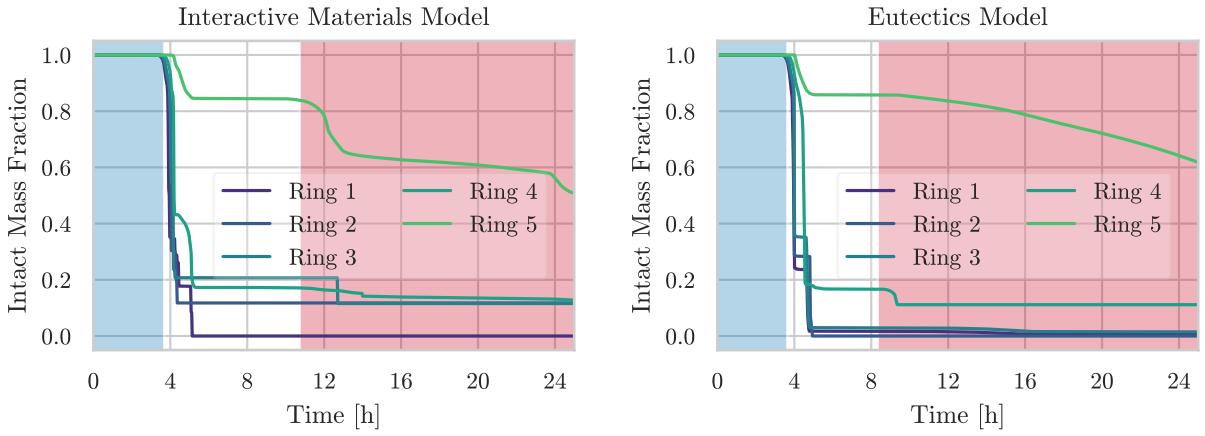

Figure 19. Comparison of fuel cladding damage progression.

Figure 20 and Figure 21 show intact fuel temperatures and intact fuel mass fractions, respectively. Fuel temperatures follow very closely, those observed for fuel cladding. Namely, heat-up begins towards the end of the early in-vessel phase. By 5 hours, peak temperatures reach 2479.0 K and 2928.1 K for the interactive materials and eutectics model simulations, respectively. As observed for other core components, fuel components cool during lower plenum boiloff and begin to heat up again after boiloff is complete. After lower head failure, multiple core cells are observed to fail,

between 12-14 hours for the interactive materials model simulation, and near 16 hours for the eutectics model simulation. Intact mass fractions of fuel components, however, differs greatly from that of the cladding. In both simulations, partial degradation of fuel components is observed in rings 1-4, while ring 5 fuel components remains 100% intact after 25 hours. At 5.5 hours, rings 1, 2, and 3 have been significantly degraded (0%, 30%, and 50% remain intact) while ring 4 has only slightly degraded (99% remain intact) for the interactive materials model simulation. By 25 hours, fuel components in rings 2, 3, and 4 have undergone further degradation with 10%, 10%, and 30% of the original UO2 mass remaining intact, respectively. By comparison, the eutectics model simulation exhibits enhanced degradation of fuel components by 5.5 hours: 18%, 0%, 18%, and 25% of fuel components remain intact in rings 1, 2, 3, and 4, respectively. The same holds true at 25 hours, with 9%, 9%, and 25% of the original fuel components remaining intact in rings 1, 3, and 4, respectively.

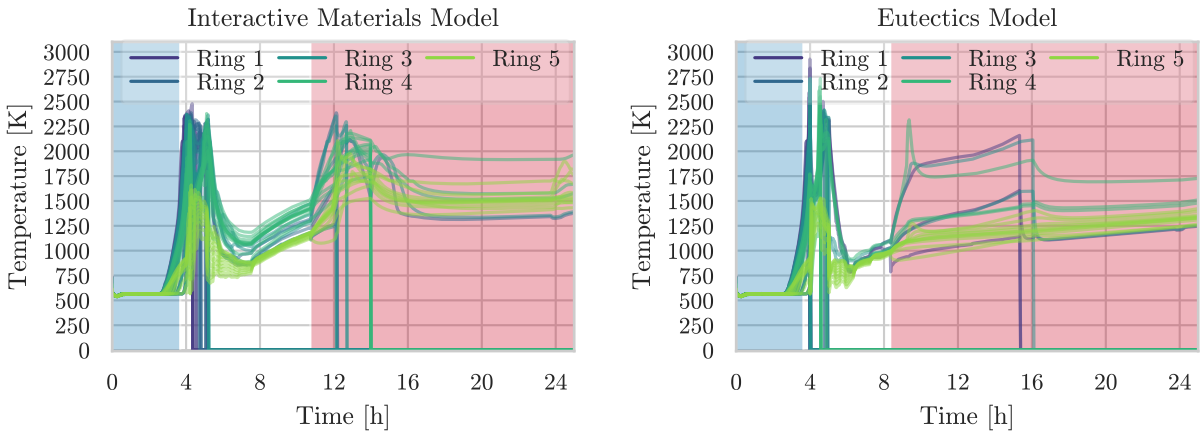

Figure 20. Comparison of fuel temperatures.

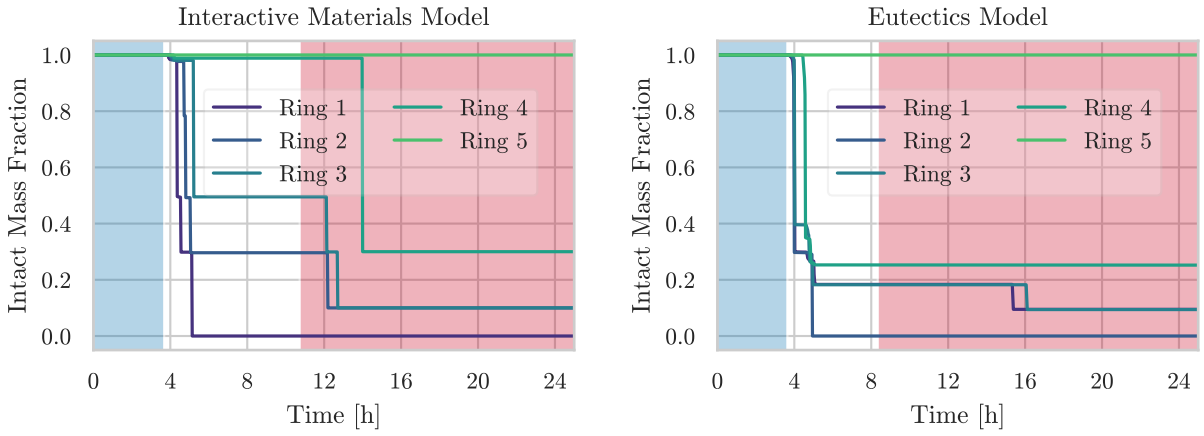

Figure 21. Comparison of fuel damage progression.

3.5. RPV Lower Head Breach

As follows from Figures 15-21, the interactive materials model simulation calculates smaller debris masses throughout the late in-vessel phase than the eutectics model, which is shown in Figure 22. The total mass of core materials is observed to increase in both simulations because of core material oxidation. Both simulations exhibit debris relocation to the lower plenum before core plate failure,

however, the majority of debris is observed to build up on the core plate until its failure in both cases. Zr is observed to relocate to the lower plenum first in the interactive materials model, while in the eutectics model the first material to relocate to the lower plenum is stainless steel, quickly followed by B_4C (not shown). After core plate failure and termination of debris slumping, both simulations exhibit between 2-4 Mg of debris remaining in the core region. Maximum total debris masses in the RPV exhibited by the eutectics model simulation, 94.1 Mg, are larger than those exhibited by the interactive materials model simulation, 57.4 Mg. Furthermore, the eutectics model exhibits larger conglomerate debris masses. At the time of maximum debris masses, only 17.7 Mg of the total debris mass is made up of conglomerate debris (previously molten) in the interactive materials model simulation. By comparison, 58.1 Mg of the total debris is made up of conglomerate in the eutectics model simulation, more evidence of the greater tendency by the eutectics model to produce molten debris. At the time of lower head failure, the majority of debris is ejected; however, debris ejection events do occur until almost 16 hours in both simulations. The total mass of all materials remaining in the RPV after 25 hours are 84.8 Mg (8.3 Mg debris) for the interactive materials model simulation and 72.7 Mg (8.0 Mg debris) for the eutectics model simulation.

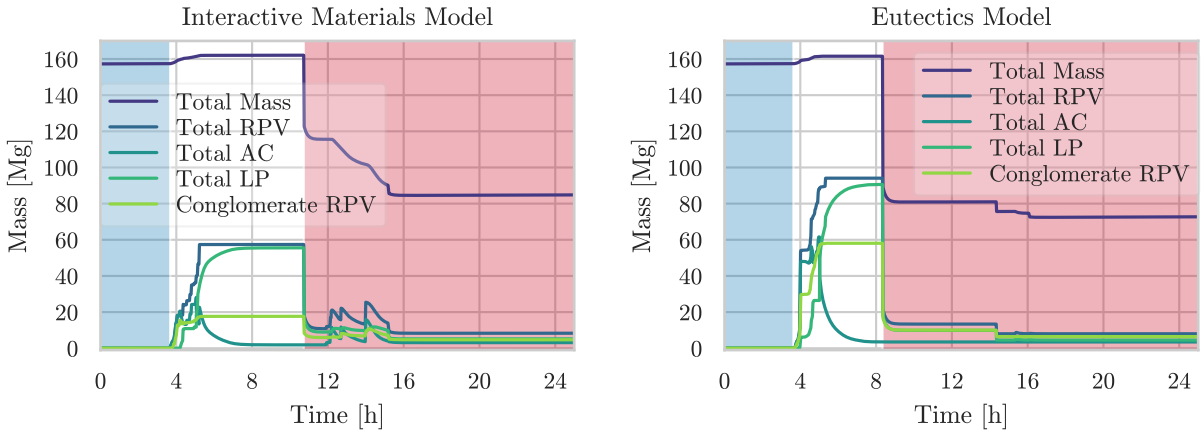

Figure 22. Comparison of debris mass distribution. Total Mass: total mass of all materials (intact and debris) in the RPV, Total RPV: total debris mass (conglomerate and particulate) in the RPV, Total AC: total debris mass (conglomerate and particulate) in the active core, Total LP: total debris mass (conglomerate and particulate) in the lower plenum, and Conglomerate RPV: total conglomerate debris mass in the RPV.

Both simulations exhibit lower plenum debris primarily made up of particulate debris, as shown in Figure 23. Oxidic and metallic molten pools (MP1 and MP2) exist only for a short period of time during initial relocation to the lower plenum. In fact, shortly after core slumping to the lower plenum, all of the molten debris, including conglomerate particulate debris above its melting point, refreezes in both simulations as discussed earlier (see Figure 12 and associated discussion). A significantly larger particulate debris bed is observed in the eutectics model simulation with a mass of 90.6 Mg. Of that mass, 55.1 Mg, or 60.8%, is conglomerate debris and was previously molten. By comparison, the interactive materials model particulate debris bed is calculated to be 55.6 Mg, with 17.2 Mg, 30.9%, of previously molten conglomerate debris. The larger mass of hot debris accelerates boil-off of the lower plenum, discussed above, and presents an earlier thermal challenge to the lower head.

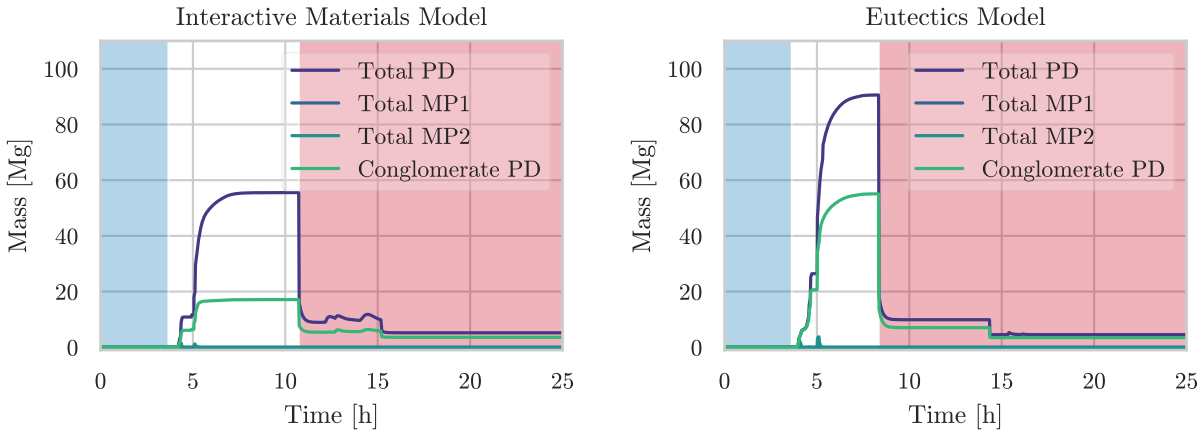

Figure 23. Comparison of lower plenum debris masses.

Figures 24-26 show the lower plenum debris temperatures in all lower plenum core cells for each debris component type (particulate debris, oxidic molten pool, and metallic molten pool). Peak lower plenum debris temperatures are higher in the eutectics model simulation. Furthermore, debris arrives in the lower plenum earlier in the eutectics model simulation, within minutes of the onset of candling, though both simulations exhibit debris in the lower plenum within 0.5 hours of the start of the late in-vessel phase. During the late in-vessel phase, peak particulate debris, oxidic molten pool, and metallic molten pool temperatures reach 2213.6 K, 2156.9 K, and 2153.9 K, respectively in the interactive materials model simulation. In the eutectics model simulation, peak temperatures are higher; PD, MP1, and MP2 temperatures reach 2654.4 K, 2872.8 K, and 2236.3 K, respectively. During the ex-vessel phase, however, average PD temperatures peak higher in the interactive materials model simulation, consistent with the larger proportion of heat-bearing materials remaining as an energy source in the RPV after lower head failure. The same also holds true for MP1 and MP2 temperatures.

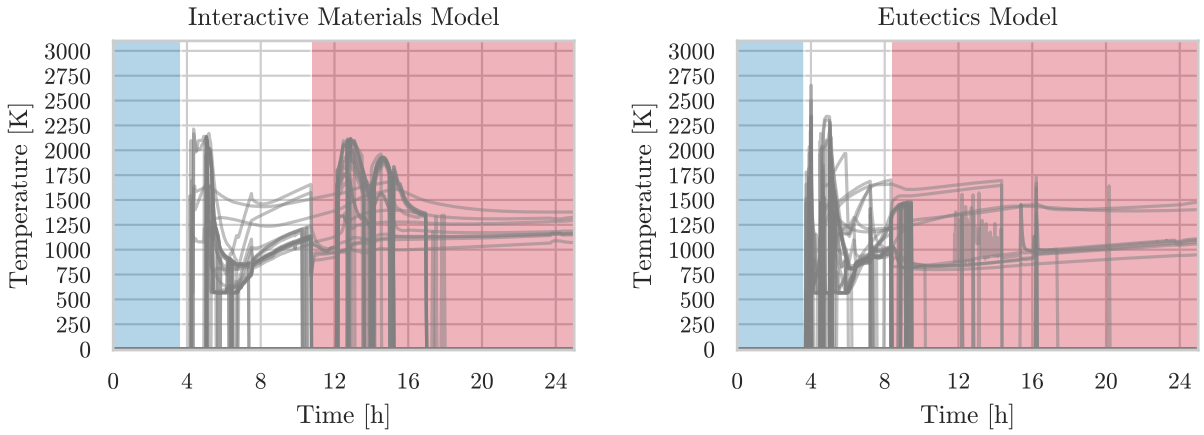

Figure 24. Comparison of particulate debris temperatures.

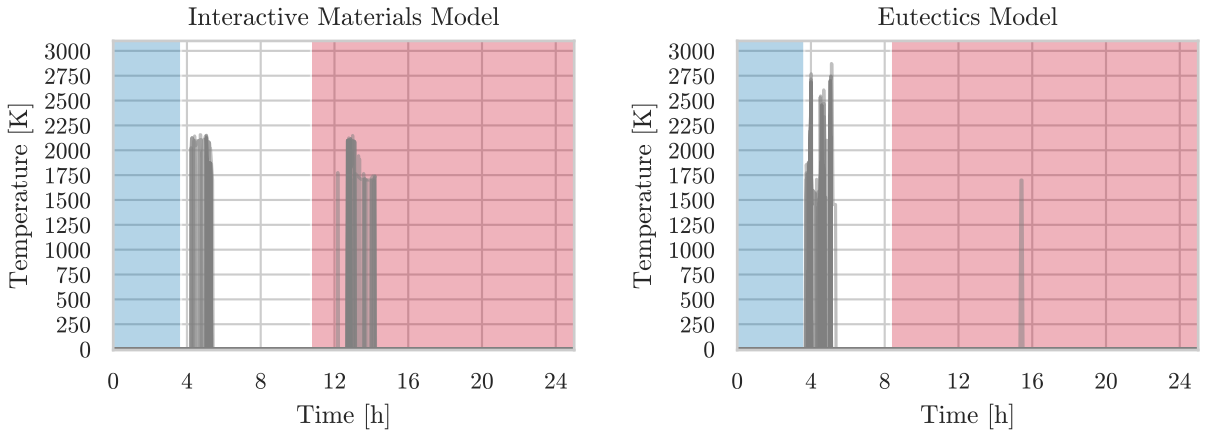

Figure 25. Comparison of oxidic molten pool temperatures.

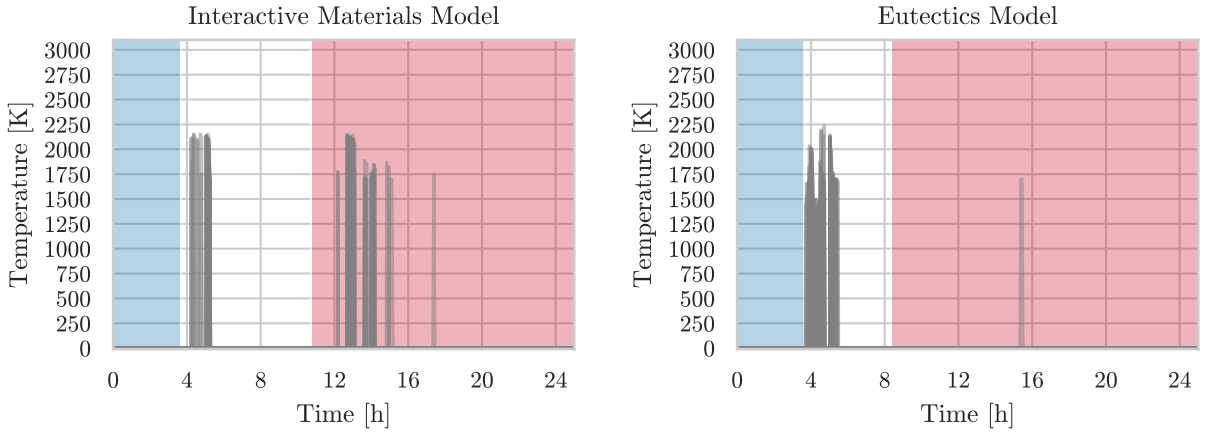

Figure 26. Comparison of metallic molten pool temperatures.

As stated previously, the eutectics model simulation exhibits an earlier thermal challenge to the lower head by a greater mass of higher temperature debris. Figure 27 shows the temperature of the inner nodes of the lower head. Heat transfer to the lower head begins much later in the interactive materials model, which also exhibits later core plate failure and core slump to the lower plenum. In the interactive materials model simulation, lower head heatup is sustained across all inner lower head nodes from 7 hours until vessel failure, which is observed at a peak temperature of 1406.8 K. Conversely, a decrease in the temperature of the first radial segment is observed prior to vessel failure in the eutectics model simulation and the lower head is observed to fail at a higher peak temperature of 1507.7 K. The lower head failure models employed are the same for each simulation.

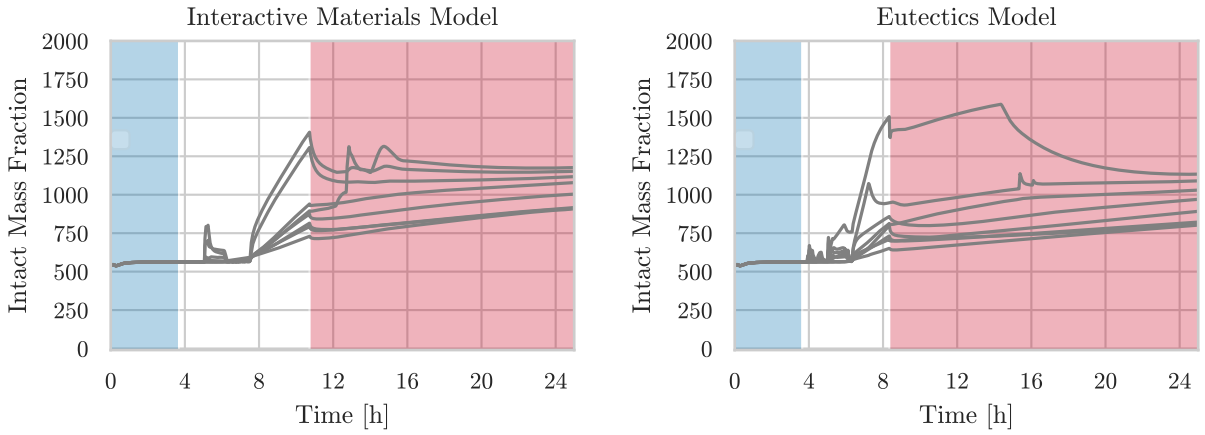

Figure 27. Comparison of lower head inner wall temperatures.

The masses of constituent materials ejected from the RPV are shown in Figure 28. Both models exhibit massive debris ejection upon lower head failure. Debris ejection events that are observed after lower head failure, in both simulations, occur after failure of remaining intact core structures (discussed in section 3.4). The interactive materials model simulation exhibits more debris formation, particularly in rings 3 and 4, after lower head failure than the eutectics model simulation. Consequently, the interactive materials model simulation also exhibits a prolonged period of debris ejection because the debris formed in the core must migrate to the RPV breach in the lower head. At 25 hours, the interactive materials model, which exhibits less debris formation, also exhibits less total ejected mass than the eutectics model simulation, 78.4 Mg compared to 89.4 Mg. Both simulations exhibit UO_2 to make up more than 50% of the total mass ejected, 51.2 Mg and 52.6 Mg for the eutectics and interactive materials model, respectively. Oxidized stainless steel makes up the smallest constituent mass of ejected debris for both simulations, 2.2 Mg and 2.7 Mg for the eutectics and interactive materials model, respectively. The eutectics model, which exhibited less core material oxidation, exhibits greater masses of ejected metallic debris (Zr and stainless steel) than the interactive materials model. Ejected Zr masses are 12.6 Mg and 7.2 Mg, and ejected stainless steel masses are 12.9 Mg and 5.3 Mg for the eutectics model simulation and interactive materials model simulation, respectively. The interactive materials model exhibits a larger mass of ejected ZrO_2, 10.5 Mg compared to 10.2 Mg.

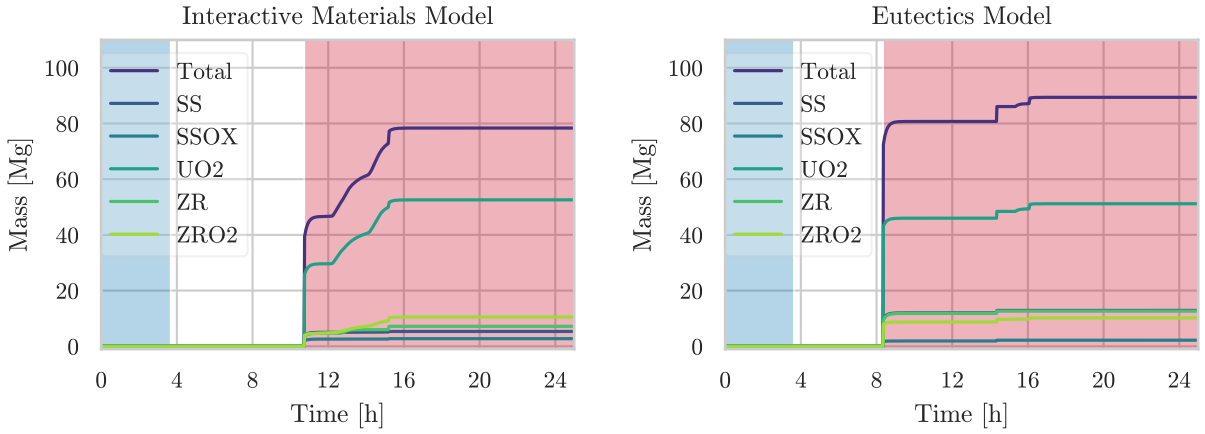

Figure 28. Comparison of ejected debris masses.

4. CONCLUSIONS

This benchmark comparison of the interactive materials model and eutectics model for a BWR under Fukushima Daiichi boundary conditions indicates that implementation of the eutectics model leads to simulation of an accelerated accident progression. Nearly all key accident signatures involving core degradation occurred earlier in the eutectics model simulation including initial SSC failures, first relocation of debris to the lower plenum, core plate failure, core slumping, lower plenum dryout, and RPV breach. A greater degree of core degradation is also exhibited by the eutectics model during the late in-vessel accident phase including larger peak molten debris mass; more complete destruction of the core; greater mass of total core debris, relocation to the lower plenum, and debris ejected. As a result of earlier destruction of core components, hydrogen generation and core materials oxidation ceases at an earlier time leading to lower masses of hydrogen and oxidized materials. Furthermore, lower core temperatures during the ex-vessel accident phase preclude a secondary, significant hydrogen generating transient that was observed in ring 5 of the interactive materials model simulation. In the eutectics model simulation, a greater mass of particulate debris relocates to the lower plenum earlier and subsequently reaches higher temperatures, presenting an earlier, greater thermal challenge to the lower head; accelerating both lower head heat-up and its ultimate failure. Finally, the user-defined liquefaction temperature of ZrO_2-interactive and UO_2-interactive is found to effectively limiting maximum temperatures that can be reached by core materials and components, and consequently the maximum ΔT possible in the core, for the interactive materials model. Such a limitation on core material and component temperatures is not observed in the eutectics model simulation. Material interactions have strong implications on the path and speed with which core degradation may occur in currently deployed LWR technologies. Material interactions, though different in detail, will continue to play a key role to the behavior of emergent accident tolerant fuel and next-generation reactors technologies under severe accident conditions.

ACKNOWLEDGEMENTS

We thank Jesse Phillips (SNL) for his time and effort reviewing this work.

Part of this work was conducted in coordination with the IAEA CRP I31033 on Advancing the State-of-Practice in Uncertainty and Sensitivity Methodologies for Severe Accident Analysis in Water Cooled Reactors.

This work was jointly supported by the U.S. DOE-NE IUP Fellowship Program and the United States Nuclear Regulatory Commission. The views expressed in the article do not necessarily represent the views of the U.S. Department of Energy or the United States Government.

Sandia National Laboratories is a multimission laboratory managed and operated by National Technology & Engineering Solutions of Sandia, LLC, a wholly owned subsidiary of Honeywell International Inc., for the U.S. Department of Energy's National Nuclear Security Administration under contract DE-NA0003525.

REFERENCES

[1] P. Hoffman, "Current Knowledge on Core Degradation Phenomena, a Review," *Journal of Nuclear Materials,* vol. 270, pp. 194--211, 1999.

[2] L. L. Humphries, B. A. Beeny, C. Faucett, F. Gelbard, T. Haskin, D. L. Louie and J. Phillips, "MELCOR Computer Code Manuals Reference Manual, Vol. 2: Reference Manual," U.S. Nuclear Regulatory Commission, Washington, DC, 2019.

[3] L. L. Humphries, B. A. Beeny, F. Gelbard, D. L. Louie and J. Phillips, "MELCOR Computer Code Manuals Reference Manual, Vol. 1: Primer and Users' Guide," U.S. Nuclear Regulatory Commission, Washington, DC, 2019.

[4] B. R. Sehgal, Nuclear Safety in Light Water Reactors: Severe Accident Phenomenology, Oxford, UK: Academic Press, 2012.

[5] T. Haste and et al., "A Comparison of Core Degradation Phenomena in the CORA, QUENCH, Phébus SFD, and Phébus FP Experiments," *Nuclear Engineering and Design,* vol. 283, pp. 8-20, 2015.

[6] P. Hoffman and D. Kerwin-Peck, "UO_2/Zircaloy-4 Chemcal Interactions from 1000 to 1700˚C Under Isothermal and Transient Temperature Conditions," *Journal of Nuclear Materials,* vol. 124, pp. 80-105, 1984.

[7] K. T. Kim and D. R. Olander, "Dissolution of Uranium Dioxide by Molten Zircaloy, I. Diffusion-controlled Reaction," *Journal of Nuclear Materials,* vol. 154, pp. 85-101, 1988.

[8] K. T. Kim and D. R. Olander, "Dissolution of Uranium Dioxide by Molten Zircaloy, II. Convection-controlled Reaction," *Journal of Nuclear Materials,* vol. 154, pp. 102-155, 1988.

[9] P. J. Hayward and I. M. George, "Dissolution of ZrO_2 in Molten Zircaloy-4," *Journal of Nuclear Materials,* vol. 265, pp. 69-77, 1999.

[10] P. J. Hayward and I. M. George, "Dissolution of UO_2 in Molten Zircaloy-4, Part 1: Solubility from 2000 to 2000 ˚C," *Journal of Nuclear Materials,* vol. 208, pp. 35-42, 1994.

[11] M. S. Veshchunov and P. Hoffman, "Dissolution of Solid UO_2 by Molten Zircaloy," *Journal of Nuclear Materials,* vol. 209, pp. 27-40, 1994.

[12] P. Nikolopoulos, P. Hoffman and D. Kerwin-Peck, "Determination of the Interfacial Energy and Work of Adhesion in the UO_2/Zircaloy-4 Diffusion Couple," *Journal of Nuclear Materials,* vol. 124, pp. 106-113, 1984.

[13] C. R. Barrett, W. D. Nix and A. S. Tetelman, The Principles of Engineering Materials, Englewood Cliffs, New Jersey: Prentice-Hall, Inc., 1973.

[14] P. Hofmann, S. Hagen, G. Schanz and A. Skokan, "Chemical Interactions of Reactor Core Materials Up to Very High Temperatures," Kernforschungszentrum Karlsruhe, Karlstein, Germany, 1989.

[15] C. Gueneau, S. Gosse, A. Quaini, N. Dupin, B. Sundman, M. Kurata, T. Besmann, P. Turchi, J. Dumas, E. Corcoran, M. Piro, T. Ogata, R. Hania, B. Lee, R. Kennedy and S.

Massara, "FUELBASE,TAF-ID Databases and OC Software: Advanced Computational Tools to Perform Thermodynamic Calculations on Nuclear Fuel Materials," in *The 7th European Review Meeting on Severe Accident Research*, Marseille, France, 2015.

[16] P. Mattie, R. Gauntt, K. Ross, N. Bixler, D. Osborn, C. Sallaberry, J. Jones and T. Ghosh, "State-of-the-Art Reactor Consequence Analysis Project: Uncertainty Analysis of the Unmitigated Long-Term Station Blackout of the Peach Bottom Atomic Power Station," U.S. Nuclear Regulatory Commission, Washington, D.C., 2016.

[17] Sandia National Laboratories, "State-of-the-Art Reactor Consequence Analysis Project, Vol. 1: Peach Bottom Integrated Analysis," U.S. Nuclear Regulatory Commission, Washington, D.C., 2013.

[18] OECD Nuclear Energy Agency, "Benchmark Study of the Accident at the Fukushima Daiichi Nuclear Power Plant - (BSAF Project) -- Phase I Summary Report," OECD/NEA/CSNI, 2016.

[19] L. I. Albright, N. Andrews, L. L. Humphries, R. O. Gauntt and T. Jevremovic, "Uncertainty Analysis of Corium Relocation to the Lower Plenum Using Results from The OECD/NEA BSAF Phase II Project," in *NURETH-18*, Portland,OR, August, 2019.

[20] N. Andrews, C. Faucett, T. Haskin, N. Bixler, D. Clayton and R. Gauntt, *Sandia National Laboratories' Contribution to the OECD/NEA BSAF Phase II Project,* United States, 2019.

[21] L. I. Albright, N. Andrews, L. L. Humphries, D. L. Luxat and T. Jevremovic, "Material Interactions in Severe Accidents - Benchmarking the MELCOR V2.2 Eutectics Model for a BWR-3 Mark-I Station Blackout: Part II - Uncertainty Analysis," *Submitted.*

[22] J. N. Cardoni, "Radionuclide Inventory and Decay Heat Quantification Methodology for Severe Accident Simulations," Sandia National Laboratories, Albuquerque, New Mexico, 2014.

[23] EPRI, "Modular Accident Analysis Program (MAAP) – MELCOR Crosswalk: Phase 1 Study," EPRI, Palo Alto, California, 2014.

APPENDIX B. UNCERTAINTY ANALYSIS

MATERIAL INTERACTIONS IN SEVERE ACCIDENTS - BENCHMARKING THE MELCOR V2.2 EUTECTICS MODEL FOR A BWR-3 MARK-I STATION BLACKOUT: PART II - UNCERTAINTY ANALYSIS

Lucas I. Albright[a,b,*], Nathan Andrews[a], Larry L. Humphries[a], David L. Luxat[a], Tatjana Jevremovic[c]

[a] *Sandia National Laboratories,1515 Eubank, Albuquerque, New Mexico 87123, United States of America*
[b] *University of Utah, 201 Presidents Cir, Salt Lake City, Utah 84112, United States of America*
[c] *International Atomic Energy Agency, Wagramer Str.5, 1220 Vienna, Austria*

ABSTRACT

Single case comparisons between severe accident simulations can provide detailed insights into severe accident model behavior, however, they cannot offer insights into model uncertainty, sensitivity to uncertain parameters, or underlying model biases. In this analysis, the single case benchmark comparison of the MELCOR material interaction models for a station blackout (SBO) scenario of a boiling water reactor (BWR) using representative Fukushima Daiichi Unit 1 boundary conditions is expanded to include an uncertainty analysis. As part of this uncertainty analysis, 1200 simulations are performed for each material interaction model (2400 total), with random sampling of 14 uncertain MELCOR input parameters. Input parameters are selected for their impact on models representing core degradation processes. These include candling, fuel rod failure, debris quenching and dryout. The analysis performed here is not a traditional "best-estimate" uncertainty analysis that uses best-estimate parameters or identifies best-estimate figure of merit distributions. Instead, it is an exploratory uncertainty analysis that identifies and interrogates underlying model form biases of the two material interaction models (*eutectics* and *interactive materials* models). Uniform distributions are applied to all uncertain parameters to ensure coverage of the model parameter uncertainty space. Key findings from this study include underlying model form biases exhibited by material interaction models, and notable differences in accident progression outcomes between the material interaction models. This uncertainty study extends and confirms the conclusions from the first part of this study, which compared the impact of material interaction modeling on simulation of a short-term station blackout scenario with representative Fukushima Daiichi Unit I boundary conditions. In particular, this study confirms that the *eutectics model* generally exhibits accelerated degradation and failure of fuel components, the core plate, and the lower head. The eutectics model also has a tendency to exhibit a greater degree of core degradation, greater debris mass formation, and larger debris mass ejection. Finally, the eutectics model exhibits higher maximum temperatures for fuel, cladding, particulate debris, oxidic molten pool, and metallic molten pool components than the *interactive materials model*; interactive materials model simulations exhibit a soft "limitation" on maximum temperatures that is related to the temperature at which material relocation occurs.

HIGHLIGHTS

* Corresponding Author
Email Addresses: lialbri@sandia.gov, (Lucas I. Albright), nandrew@sandia.gov (Nathan Andrews), llhumph@sandia.gov (Larry L. Humphries), dlluxat@sandia.gov (David L. Luxat), T.Jevremovic@iaea.org (Tatjana Jevremovic)

- Bifurcating accident progression signatures contrast material interaction models
- Model biases are identified for material interaction models in MELCOR V2.2
- Eutectics model simulations exhibit accelerated fuel degradation
- Higher peak fuel rods and debris temperatures are exhibited by the eutectics model
- More extensive molten material formation is calculated by the eutectics model

Keywords: MELCOR, Severe Accident, Material Interactions, Eutectics Model, Interactive Materials Model, Uncertainty Analysis

1. INTRODUCTION

Material interactions are fundamental to the complexity of severe accidents. These interactions serve to initiate a loss of core geometry through formation of intermetallic compounds that liquefy at temperatures well below that of the pure melting points of the core materials. For example, local material interactions leading to failure in one component may subsequently challenge the integrity of neighboring core components, setting off progressive degradation of core and vessel structures ultimately leading to reactor pressure vessel (RPV) failure. A summary of the phenomenology of material interactions between core materials under severe accident conditions, particularly for the fuel-clad system, is discussed in Part I of this study [1]. The effects of material interactions on degradation and failure of reactor core systems, structures, and components (SSCs) and fission product barriers (FPBs) in light water reactors (LWRs) is discussed in greater detail below.

1.1. Material Interactions and Core Degradation

Under severe accident conditions, the structural integrity of the LWR fuel-clad system (fuel pellets, gap, and cladding) faces a number of challenges. During core uncovery, rapid cladding oxidation in the steam environment leads to growth of an oxide scale (ZrO_2 for Zr-based cladding alloys) [2]. The oxide scale serves as a protective barrier to internal unoxidized cladding materials and impacting the rate of cladding oxidation. At the unoxidized clad-oxide scale interface, oxygen diffuses across the steep concentration gradient between the ZrO_2 and unoxidized Zr, thereby sustaining growth of the oxide scale. Cladding embrittlement accompanies growth of the oxide scale and local breakaway of embrittled cladding may occur, thereby thinning and decreasing the thickness and remaining structural integrity of the oxide scale [3].

Thick oxide layers can provide some structural support to fuel rods – here a "thick oxide layer" is defined as an oxide scale with enough thickness to preserve the rod-like geometry of degraded fuel rods. The structural support provided by an oxide layer can maintain fuel rod integrity at temperatures in excess of the melting point of cladding materials [2]. A layer of unoxidized and partially oxidized materials located between intact fuel pellets and the oxide layer liquify after exceeding their melting point, but are unable to relocate due to hold-up by the oxide-layer. Persistent extreme temperature conditions inevitably cause oxide layer failure, at which point, held-up molten materials are released. Failure, or breach, of the oxide layer typically occurs by physical stress (e.g. crack or rupture) or thermo-chemical attack (i.e. material interactions) by held-up molten materials – a similar process can also occur externally in the presence of a molten mixture [3] and is described in greater detail in part I of this analysis [1]. Alternatively, failure of support structures can cause fuel rod failure and relocation of both molten debris and solid, partially intact debris. Similar failure pathways are generally considered for other oxidized core SSCs as well.

SSC failures have important consequences on severe accident progression, often leading to bifurcations in accident progression. Both solid and molten debris relocation pathways relocate materials to lower core elevations, however, debris distribution, heat transfer, and the challenges presented to neighboring structures are fundamentally different. In the case of candling from intact, rod-like core geometry, molten material discharged from a breach site relocates to lower, presumably cooler core elevations along a structure's surface until the candled material refreezes. Upon refreezing, significant heat (latent heat of fusion) is deposited into the structure at the freezing site decreasing the safety margin to a subsequent local failure; safety margin here is defined as the difference between the actual value of a physical property for a given component and the failure limit of that same property for that component. Refrozen materials may also partially occlude, or even block existing flow channels; an important milestone leading to the loss of coolable, rod-like geometry. Another effect of refreezing is the formation of a protective layer on the surface of the refreezing structure that reduces the exposed surface area of that structure and limits chemical reactions between the environment and structure (e.g. oxidation). Alternatively, solid, partially intact debris relocates downward by gravity until it is held-up by other SSCs or debris at lower elevations; because the debris was never liquid, there is no significant, local deposition of heat that accompanies its relocation aside from normal heat transfer processes. While the flow channel that the partially intact debris occupies is occluded by the debris, limited flow through the debris is likely to continue due to the porous structure of debris beds. Moreover, the partially intact debris does not offer any "protection" to nearby structures as in the case of candled materials; chemical processes between the environment, nearby structures, and partially intact debris will continue unimpeded. In fact, due to the increased surface area of partially intact debris relative to the intact parent structure, chemical processes may accelerate as long as reactants are available.

1.2. Material interactions, Core Slumping, and Lower Head Failure

The impact of material interactions is not limited to accelerated degradation of the active core, but also affect debris morphology and relocation pathway characteristics during the transition to degradation of lower plenum structures beginning with the core plate. In boiling water reactors (BWRs), the lower plenum has a large inventory of both liquid water (~39000 kg at 1F1) and structural materials (~25000 kg at 1F1) that function as a sink for heat rejected by lower plenum debris. In particular, the superheated debris relocating into the lower plenum, termed core slumping when large masses of debris are relocating, rejects heat as it "falls" through the lower plenum pool until lower plenum dryout or the debris is quenched. A wide range of heat fluxes from falling debris to the lower plenum pool are possible and depend on the characteristics of the debris (e.g. temperature, surface area, and falling velocity). Eventually, lower plenum debris accumulates into one or more debris beds – debris beds are supported by either intermediate crusts formed by quenched debris or the lower head. Within a debris bed, heat transfer is limited by the bed porosity and the ability of water to permeate lower elevations of the debris bed; if the heat flux is high enough, water entering the debris bed will boil before reaching the bottom of the debris bed, causing a counter current flow limitation. Alternatively, unquenched lower plenum debris may accumulate into one or more molten pools. Molten pools may be metallic or oxidic in composition, but metallic and oxidic molten pools will be immiscible. Other lower plenum molten pool characteristics of significance to accident progression in LWRs are greater heat rejection to nearby structures and debris facilitated by convection of the molten debris and greater heat conduction to the lower head after "wetting" of the lower head wall.

Sustained challenges to the lower head by lower plenum debris eventually induce failure; however, the nature of the challenge presented to the lower head will impact the outcome. Similar to other core SSCs, the lower head may face both thermo-chemical and thermo-physical challenges that lead to gross or localized failure. For example, gross rupture by structural and thermal loading by a massive lower plenum debris bed, might exhibit rapid, massive ejection of largely solid debris located at and above the elevation of the rupture site. Conversely, localized melt-through by molten debris might exhibit largely liquid debris ejection until growth of the failure site accommodates the size of solid debris.

This paper describes a severe accident uncertainty study of a short-term station blackout (SBO) scenario for a boiling water reactor (BWR). This SBO scenario is based on the Fukushima Daiichi Unit 1 accident boundary conditions. The plant model used for this study is the Fukushima Daiichi Unit 1 model developed by Sandia National Laboratories for phase 2 of the Benchmark Study of the Accident at the Fukushima Daiichi Nuclear Power Plant (BSAF) [4]. As in part I, the goal of this work is not to explicitly replicate the key accident signatures observed during the Fukushima Daiichi Unit 1 accident, but to perform a fundamental comparison between the eutectics and interactive material models, and to inform future model development [1]. In particular, the focus for this part of the benchmark is the impact of material interaction models on accident progression, and the degradation of SSCs and FPBs. Section 2 describes the analysis methodology including a description of relevant MELCOR V2.2 models and specifications of the uncertainty analysis. Analysis results are presented in section 3 with discussion. Lastly, a brief summary of the analysis and review of main findings comprise section 4.

2. MATERIALS AND METHODS

2.1. MELCOR V2.2

The MELCOR code, successor to the Source Term Code Package, is a plant risk assessment tool developed at Sandia National Laboratories for the U.S.NRC [5] [6]. Over the decades of development since its original inception, the MELCOR code has transitioned from a fast-running, parametric source term code with large epistemic uncertainty, into a highly flexible, primarily mechanistic severe accident code. MELCOR applications include large-scale uncertainty analysis. The MELCOR code lends itself to large-scale uncertainty analysis with its built-in flexibility in modeling choices and parameter selection available to users. This analysis is performed with MELCOR V2.2 revision 15348. As in part I, MELCOR material designations are used in place of chemical forms in the description of MELCOR models in the present section to maintain consistency with other references: zirconium (ZR), zirconium dioxide (ZRO2), uranium dioxide (UO2), stainless steel (SS), oxidized stainless steel (SSOX), and boron carbide (B4C) [1].

2.1.1. MELCOR Material Interactions Models

There are currently two material interaction models available to users in the MELCOR code: the interactive materials model and the eutectics model. Broadly speaking, the eutectics model approximates material interactions mechanistically for materials in physical contact. The interactive materials model treats material interactions parametrically through modification of individual material liquefaction temperatures. Each material interaction model is described in more detail in part I of this benchmark [1]. Alternatively, users can find the authoritative descriptions in references [5] [6].

2.1.2. MELCOR Candling Models

Prior to component failure, the candling model can be a primary mechanism of relocation for mass and energy in the core. The candling process, as modeled, relocates molten materials to lower core elevations until a blockage is encountered or the molten mixture refreezes onto the surface of the "refreezing component." Upon refreezing, the mass of refrozen material is added to the conglomerate[7] field of the refreezing component, the exposed surface area of the refreezing component is reduced, the latent heat of refrozen materials is transferred to the refreezing component, and the cross-sectional flow area is reduced or in some cases eliminated.

The candling model in MELCOR assumes a steady melt generation rate over each time-step while materials exceed their liquidus temperature. The amount of candled material that refreezes on a component within a given time-step is determined by the heat transfer between the molten material and the component. When the amount of heat transferred exceeds the sensible heat of the candled materials, a portion of the candled material is refrozen on to the refreezing component. An exhaustive description of the heat transfer for steady flow candling is found in the MELCOR V2.2 reference manual [5].

Within a given time step, the entire mass of material determined to candle also reaches its final destination (i.e. it refreezes or the flow path is blocked). Candled materials refreeze onto the same component type as the originating component, if present. When candled materials refreeze in a core cell that does not contain the originating component type, the molten materials will refreeze to an alternate refreezing component according to Table 6. When there are no components of either the originating component type or a suitable alternate refreezing component type, candled materials will fall-through to the next lowest core cell.

Table 6. Alternate Refreezing Components

Core Region	Originating MELCOR Component Type				
	CL – Fuel Cladding Component	**CN/CB – Fuel Canister Component (fuel channel/ bypass)**	**SS/NS – Supporting/ Non-supporting Structure Components**	**PD – Particulate Debris Component (fuel channel)**	**PB – Particulate Debris Component (bypass region)**
Active Core	1. PD 2. Fall-through	1. PD 2. Fall-through	1. PB/PD 2. Fall-through	1. CL 2. Fall-through	1. NS 2. Fall-through
Lower Plenum	1. PD 2. SS 3. Fall-through	1. PD 2. SS 3. Fall-through	1. PD 2. Fall-through	1. CL 2. SS 3. Fall-through	1. NS 2. SS 3. Fall-through

Candling may also occur when molten materials have been held up by a crust or other blockage in the core preventing downward relocation of molten materials. It should be noted that when the interactive materials model is activated, materials candle independently at their designated melting points (e.g. the stainless steel and zirconium in a stainless steel/zirconium mixture will melt and relocate at different times, separating the mixture). Conversely, the eutectics model allows candling

[7] The conglomerate field of a component is a MELCOR object used to track the mass of previously molten materials that have refrozen onto a given component.

of the conglomerate debris mixture according to the composition-dependent mixture properties evaluated by the eutectics model (e.g. stainless steel/zirconium mixtures will melt and relocate at the same time). Moreover, refrozen mass has the same composition as the molten mixture.

The MELCOR candling model tracks the vertical distribution of refrozen candled materials in each core cell to identify flow channel blockages. The vertical distribution of refrozen candled materials is tracked across "sub-nodes," a vertical discretization of the core cell, that allow formation of local blockages within a core cell. By default, MELCOR creates 10 vertically distributed sub-nodes per core cell. Local blockages hold up both molten materials, which are converted into either metallic or oxidic molten pool, and particulate debris. More information on the vertical distribution of refrozen candled material in MELCOR can be found in references [5] and [6].

Candled material that refreezes accumulates and occludes the surface area of the underlying component. Reduction in the component surface area due to conglomerate debris accumulation impacts future oxidation, convection, and material refreezing models as long as the occlusion is present. Equations governing the surface area effects of conglomerate debris are explained in detail in the MELCOR reference manual [5].

As described in part I [1], during core degradation, oxidation of core materials forms an oxide layer. Molten materials contained by an oxide shell cannot relocate until breach of the oxide layer. To model this phenomenon, MELCOR uses a molten material holdup model. Two criteria are used to determine whether an oxide layer is intact: the critical oxide thickness, $\Delta \mathrm{r}_{\mathrm{hold}}$, and the critical temperature, T_{breach}. So long as an oxide layer thickness is greater than $\Delta \mathrm{r}_{\mathrm{hold}}$, and the component temperature is less than T_{breach}, then the oxide layer is considered intact. After initial breach, the oxide layer is considered degraded regardless of component temperature or thickness. During the initial breach of an oxide layer, the release of a mass of molten material M_m, candles over a constant timestep Δt_{break}, with a maximum flow rate of $\Gamma_{\max}$:

$$\Delta t_{break} = \max\left[\Delta t, \frac{M_m \Delta z}{\Gamma_{\max} A_s}\right] \tag{1}$$

where Δz is the height of the core cell, and A_s is the surface area of the component. By default, $\Delta \mathrm{r}_{\mathrm{hold}} = 0.00001\mathrm{m}$ and $T_{breach} = 2400\mathrm{K}$, however, users can modify both parameters with sensitivity coefficients 1131(1) and 1131(2) through the COR_SC input record. Similarly, $\Delta t_{break} = 1\mathrm{s}$ and $\Gamma_{\max} = 1\frac{\mathrm{kg}}{\mathrm{m \cdot s}}$ by default but can be modified by users with sensitivity coefficients 1141(1) and 1141(2).

2.1.3. MELCOR Fuel Rod Failure Models

MELCOR has multiple built-in fuel rod failure pathways. In MELCOR, intact fuel rods are represented in each core cell by a fuel (FU) component, and a cladding (CL) component. The simplest fuel rod failure pathway is failure of any component supporting a given fuel component. Fuel components are supported by structures in core cells at lower elevations including other fuel components and supporting structure (SS-comp) components such as the core support plate. Fuel components are also supported by the cladding components in same core cell. Should any component supporting fuel components fail, the fuel component will be converted to particulate debris.

The second pathway for fuel rod failure is the reduction of the unoxidized cladding thickness to a given $\Delta r_{CL,min}$ defined as the "component critical minimum thickness criteria." Should the unoxidized cladding thickness be reduced below $\Delta r_{CL,min}$, the fuel component will be converted to particulate debris. Unoxidized cladding thickness can be reduced through a number of mechanisms including, cladding oxidation, melting, and candling. Users can modify $\Delta r_{CL,min}$ through the DRZRMN data field of the COR_CCT input record, however, modification of that data field also affects the component critical minimum thickness criteria of canister structures in a BWR model. By setting $\Delta r_{CL,min}$ to 0, users can prevent this pathway for fuel component failure. Consequently, fuel components will remain standing until other failure criteria are met.

Fuel rods may also fail through discrete temperature criteria. There are currently two discrete temperature criteria, dependent on cladding composition, that define fuel rod failure temperatures. Users may modify both criteria sensitivity coefficients 1132(1) and 1132(2) through the COR_SC input record. The first temperature criterion corresponds to early failure of oxidized fuel rods as observed in the Phébus experiments and is applied only in the absence of metallic zirconium (i.e. the ZR in the cladding component has oxidized/candled completely) [7]. MELCOR has a default value of 2500K is appropriate for irradiated fuel rods. The second temperature criterion, designed to fail fuel rods unconditionally, corresponds to situations where fuel rods may reach high temperatures in the absence of an oxide layer; either in an inert environment, or after loss of the oxide layer through candling, secondary transport, eutectics interactions, or melting. The default value for this criterion is 3100K. As with other fuel rod failure pathways, fuel components are converted to particulate debris upon reaching these criteria.

Lastly, MELCOR has a time-at-temperature (TaT) model designed to approximate physio-chemical processes that lead to fuel rod failure under prolonged severe accident conditions [5] [6]. Failure by the so-called "sharkfin" TaT model results in an instant transition from intact rod geometry to particulate debris. Activation of the TaT model prevents potentially non-physical fuel rod behavior, in which fuel rods exist at high temperatures for significant periods of time. Based on data from the VERCORS experiments [8], the TaT applies a temperature dependent lifetime criterion to prevent nonphysical existence of fuel rods at high temperatures for extended periods of time. The TaT model takes the form of a damage fraction defined by:

$$D_{fraction}(t) = \sum_i^N \frac{1}{L(T)_i} \Delta t_i \tag{2}$$

where $D_{fraction}(t)$ is the fuel component damage fraction with respect to time, $L(T)_i$ is the lifetime value of the fuel component at the ith timestep, and Δt_i is the length of the ith timestep. When $D_{fraction}(t) = 1.0$, the fuel component fails.

$$\frac{1}{L(T)} = A \exp{(BT)} \tag{3}$$

The reciprocal of the lifetime value, $L(T)$, for some temperature T, is assumed to follow an Arrhenius relation, with coefficients $A = 2.16 \times 10^{-11} \left[\frac{1}{\mathrm{s}}\right]$ and $B = 7 \times 10^{-3} \left[\frac{1}{\mathrm{K}}\right]$ corresponding

to the 50th percentile of possible Arrhenius curves identified in [9]. Expected fuel rod lifetime using default parameters is shown in Figure 29.

The "sharkfin" TaT model is enabled by default in MELCOR. Users have the option to disable the model by setting the IRODDAMAGE data field in the COR_ROD input record to "OFF." Alternatively, users can apply their own time-at-temperature criterion with a tabular function on the same record.

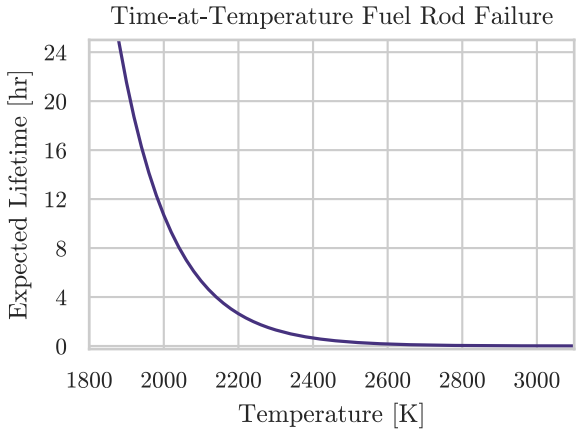

Figure 29. Default time-at-temperature fuel rod failure model [5] [6].

2.1.4. MELCOR Debris Quenching and Dryout Models

There are two modes of debris heat transfer to liquid water pools in the MELCOR code: (1) falling debris quench and (2) stable debris bed heat transfer. The falling debris quench mode models rapid quenching of hot debris during its relocation downward through liquid water pools (e.g. after core plate failure). The stable debris bed heat transfer mode models the boil-off of an overlying water pool by a particulate debris bed.

The falling debris quench model calculations begins at the time of core support plate failure. An elevation for the leading edge of falling debris, z_d, is calculated for each core ring using a user-defined, constant velocity of falling debris, v_d, input in the VFALL data field of the COR_LP input record.

$$z_d = z_{csp} - v_d\left(t - t_{fail}\right) \tag{4}$$

Where z_{csp} is the elevation of the core support plate, t_{fail} is the time of core support plate failure of a given ring, and t is the current simulation time. All debris above z_d, previously supported by the failed core support in that ring, will relocate downwards until all of the debris has relocated, the free volume below z_d has been filled, or the falling debris encounters supporting structures at lower core elevations.

Falling debris quench heat transfer begins when the falling debris enters the pool of liquid water. A heat transfer surface area is calculated for the falling debris, assuming spherical debris, using the user-defined hydraulic diameter for particulate debris – defined with the DHYPD and DHYPB data

fields of the COR_EDR input record for the appropriate axial levels. The heat transfer coefficient, also user-defined in the HDBH2O data field of the COR_LP input record, is assumed constant until falling debris reaches lower head and significant debris relocation halts in that core ring. After both conditions are met, a decay factor is applied to the constant heat transfer coefficient given by:

$$f(t+\Delta t) = \min\left[1, f(t)\, exp\left(-\frac{\Delta t}{\tau_{spr}}\right) + \frac{V_{cor}}{V_{LP}}\right] \tag{5}$$

where $f(t)$ is the time-dependent heat transfer decay factor, Δt is the length of a given core timestep, τ_{spr} is the time constant for solid debris radial spreading, V_{cor} is the volume of core debris that relocates into the ring from radial spreading over Δt, and V_{LP} is the volume of debris in the ring beneath the core support plate. The heat transfer coefficient decay factor approximates the transition from rapid falling debris quench to stable debris bed heat transfer. To account for additional falling debris as a result of radial debris spreading above the core plate, the decay factor has a time constant equal to the solid debris radial spreading time constant. The decay factor is initially 1.0, and transition to stable debris bed heat transfer is considered complete when the decay factor falls below 0.01. While the falling debris quench model is active in a given core ring, candling, dissolution, and radial debris spreading models in that ring are deactivated.

After the formation of a stable debris bed, heat transfer becomes limited by hydrodynamic phenomena (i.e. how much water can reach the debris). MELCOR assumes that a liquid pool of water is displaced by the debris bed, and therefore that cooling of the debris bed is achieved through downward migration of liquid water into the debris bed. However, the downward migration of water through the debris bed is restricted by counter-current, upward flow of water vapor produced in the debris bed. Dryout occurs when vapor production in the debris bed prevents liquid from permeating the debris bed, and the associated dryout heat flux is calculated by the Lipinski zero-dimensional correlation [10]. The Lipinski zero-dimensional correlation is considered to be a maximum heat transfer rate, q_d, from the stable debris bed and is given by:

$$q_d = 0.756\, h_{lv}\left[\frac{\rho_v(\rho_l-\rho_v)gd\varepsilon^3\left(1+\frac{\lambda_c}{L}\right)}{(1-\varepsilon)\left[1+\left(\frac{\rho_v}{\rho_l}\right)^{\frac{1}{4}}\right]^4}\right]^{-\frac{1}{2}} \tag{6}$$

where h_{lv} is the latent heat of water, ρ_v is the vapor density of water, ρ_l is the liquid density of water, g is gravitational acceleration, d is the debris diameter, ε is the porosity of the debris bed, L is the depth of the debris bed, λ_c is the liquid capillary head in the debris bed:

$$\lambda_c = \frac{6\sigma\cos(\theta)(1-\varepsilon)}{\varepsilon d(\rho_l-\rho_v)g} \tag{7}$$

where σ is the surface tension of water, and θ is the wetting angle. If calculated heat transfer rates reach the dryout heat flux in a core cell, no convective heat transfer to the pool by other components in that cell is calculated. Furthermore, stable debris bed heat transfer is not calculated for core cells at lower axial levels. Stable debris bed heat transfer model parameters that are accessible to users include the leading constant (0.756), nominal capillary head (for 0.5 mm particles

in approximately 0.089 m of water), and the minimum debris porosity (default 0.15) with sensitivity coefficients 1244(1) and 1244(2), and 1244(3), respectively, through the COR_SC input record.

2.2. Plant Representation

The general plant representation used in this part of the benchmark is identical to that used in part I [1]. The plant is based off of the Fukushima Daiichi Unit 1 nuclear reactor (460 MW(e) BWR/3 reactor housed in a Mk-I containment), however, changes made to the input deck for this analysis are not necessarily representative of the severe accident at Fukushima Daiichi Unit 1 (1F1). As in part I of this benchmark, the accident scenario is representative of the SBO at 1F1 including early operation of the isolation condenser (IC), wetwell venting, and the reactor building explosion. A more detailed description of the plant representation is presented in part I and [11].

2.3. Parametric Uncertainty Analysis Specification

This parametric uncertainty analysis includes 2400 MELCOR simulations using each material interaction model (1200 for each model). Each simulation includes a forward propagation of uncertainty for 14 randomly sampled uncertain MELCOR input parameters. Uncertain parameters from the COR8 and MP9 packages are selected due to their relevance to material interaction, early fuel/cladding degradation and failure, and lower plenum debris quench phenomena. The present uncertainty analysis is unlike past uncertainty analyses which have considered source term and consequence uncertainty [12] [13] [14]. The purpose of this uncertainty analysis is to develop accident progression insights through a survey of the uncertainty space and underlying biases in each material interaction model; as such, it is not a best-estimate uncertainty analysis. In other words, the analysis does not consider "best-estimate" distributions of input parameters or attempt to establish "best- estimate" distributions of figures of merit. Instead, uniform distributions are imposed for all input parameters to promote coverage of the uncertainty space and perform a "blind" comparison of models. By using uniform distributions, a priori biases on input and result distributions are removed and model biases across the entire parametric uncertainty space are investigated. Equitable comparison between models is ensured by using the same uncertain parameters and respective distributions for each material interaction simulation set where possible. Parameters unique to one of the material interaction models are, of course, not shared between simulation sets (i.e. the interactive materials model reduced liquefactions temperatures are irrelevant to eutectics model simulations). Uncertain parameters included in this uncertainty analysis can be found in Table 7, and are described in greater detail below.

[8] The MELCOR core (COR) package comprises all models that describe the response of core structures in the lower plenum and active core region to an accident transient including core degradation.
[9] The MELCOR material properties (MP) package contains the physical properties of all built-in materials and modelling options for additional user-defined materials.

Table 7. Uncertain Parameters

Input Record	Description	Units	Distribution	Parameter Range	
				Interactive Materials Model	Eutectics Model
MP_PRC: ZRO2-INT, UO2-INT	Interactive materials model reduced liquefactions temperatures for ZRO2-INT and UO2-INT	K	Uniform	2230.0-2728.0	Not Applicable
COR_NS: TNSMAX	Maximum temperature of NS structure permitted before collapse	K	Uniform	1520.0-1700.0	
COR _SC: 1131(2)	Molten Material Holdup Parameters: Maximum ZRO2 temperature permitted to hold up molten Zr in CL.	K	Uniform	2100-2540	
COR _SC: 1141(2)	Core Melt Breakthrough Candling Parameters: Maximum melt flow rate per unit width after breakthrough	kg m/s	Uniform	0.1-2.0	
COR_CCT: DRZRMN	Component Critical Minimum Thicknesses	m	Uniform	0.0-0.00015	
COR_SC: 1132(1)	Core Component Failure Parameters: Temperature to which oxidized fuel rods can stand in the absence of unoxidized Zr in the cladding.	K	Uniform	2230.0-2728.0	
COR_ROD	Rod Collapse Model	-	Discrete Uniform	Active (0), Disabled (1)	
COR_EDR: DHYPD, DHYPB	Particulate debris equivalent diameter in the lower plenum	m	Uniform	0.0001-0.005	
COR_EDR: DHYPD, DHYPB	Particulate debris equivalent diameter in the active core region	m	Uniform	0.005-0.015	
COR_LP: HDBH2O	Heat transfer coefficient of falling debris	W/m^2K	Uniform	100.0-4000.0	
COR_LP: VFALL	Velocity of falling debris	m/s	Correlation	-	
COR_TST: IMPLZDM	Lipinski zero-dimensional dryout heat flux flag	-	Discrete Uniform	Active (0), Disabled (1)	
COR _SC: 1244 (3)	Debris Dryout Heat Flux Correlation: Minimum Debris Porosity	-	Uniform	0.15-0.4	

2.3.1. Material Interactions Model Parameters

As part of the State-of-the-Art Reactor Consequence Analysis (SOARCA) uncertainty analysis, a distribution for reduced liquefaction temperatures of the fuel-clad (U-Zr-O) system was developed [13] [14]. The distribution is derived from fuel collapse temperature data obtained during different experiments and accounts for the effects of both fuel burnup and cladding oxidation on liquefaction temperatures. The minimum and maximum liquefaction temperatures of both UO2-INT and ZRO2-INT (input record – MP_PRC: ZRO2-INT, UO2-INT) applied in this study were obtained by taking the 3σ limit of the normal distribution used in the SOARCA uncertainty analyses in either direction about the mean value 2479.0 K [2230.0 K – 2728.0 K]. The same value is applied for both UO2-INT and ZRO2-INT. Secondary material transport model parameters were not perturbed in this analysis. Eutectics model simulations used default model parameters for each aspect of the model: eutectic reaction temperatures, composition-dependent mixture properties, and dissolution models.

This analysis is a first attempt to characterize the primary differences between the eutectics and interactive materials models in MELCOR. To capture the behavior of the U-Zr-O-X systems, where X indicates any number of other interacting materials (e.g. Fe, fission products, etc.), including early fuel rod failure and mixture liquefaction temperatures, this study made the following assumptions:

1. The interactive materials model approximates the variation in liquefaction temperature for all plausible U-Zr-O-X mixture compositions, with a single, globally modified liquefaction temperature.
2. The distribution applied to the liquefaction temperatures for UO2-INT and ZRO2-INT in this study captures the liquefaction of plausible U-Zr-O-X compositions in addition to the effects of both fuel burnup and cladding oxidation.
3. By default, the eutectics model approximates the reduced liquefaction temperatures for UO_2-ZrO_2 mixtures mechanistically with a pseudo binary phase diagram described in part I of this analysis [1] and MELCOR references [5] [6].
4. By default, the eutectics model approximates the reduction in liquefaction temperature for all other U-Zr-O-X mixture compositions with composition dependent mixture properties calculated as described in part I of this analysis.
5. Further modification of the UO_2-ZrO_2 eutectic temperature in the eutectics model for this study is considered unnecessary by the authors because the effects of other materials on mixture liquefaction temperatures are already captured by the composition dependent mixture property calculation.

The choice by the authors of this study to use the MELCOR default 2450K UO_2-ZrO_2 eutectic temperature, and not include alternate UO_2-ZrO_2 eutectic temperatures was adopted to emphasize how the uncertainty models used to drive each material interaction model are not a one-to-one mapping. To reiterate, the interactive materials model treats a broad range of multi-component mixtures liquefaction temperatures through a single uncertain parameter whereas the eutectics model utilizes a composition dependent mixture property calculations to determine multi-component mixture liquefaction temperatures. The choice to not include alternate UO_2-ZrO_2 eutectic temperatures is expected to substantively impact the results and conclusions of this analysis. Firstly, the liquefaction temperature for all UO_2-ZrO_2-X mixtures, as determined by the composition dependent mixture property calculation, are higher in this study than if lower eutectic temperatures had been considered. This forces mixtures to reach higher temperatures before the solid to liquid

phase transformation and subsequent material relocation occurs. Higher core component temperatures function to accelerate oxidation of Zr and Fe as well as hydrogen generation. Furthermore, fuel rod lifetimes as determined by the TaT model decrease at higher temperatures. Predicting the impact of the UO_2-ZrO_2 eutectic temperature in the late phases of core degradation is non-trivial due to the complicated interactions between core degradation phenomena, however, it is expected that component temperatures, molten debris masses, and event timings (e.g. core plate failure, lower head failure, etc.) would be substantively affected.

Control blade failure temperatures are also perturbed as part of this analysis. The TNSMAX data field of the COR_NS input record determines the temperature at which the control blade structure collapses. Standard practice in the past has been to implement a maximum control blade temperature of 1520K to account for the interaction between B4C and SS parametrically. With that implementation, structures reaching 1520K collapse and relocate as particulate debris. In reality, the B4C/SS interaction rate accelerates at 1520K, but the control blade does not necessarily collapse as solid debris. In this analysis, the maximum control blade temperature before collapse is varied from 1520K to 1700K (failure temperature for pure SS structures) to survey the uncertainty in collapse temperatures of control blade structures due to B4C/SS interaction. It should be noted that the eutectics model B4C/SS interaction will not be utilized if the collapse temperature is at or below the interaction temperature.

2.3.2. Candling Model Parameters

Candling model parameter distributions used in this analysis were also informed by the distributions developed for the same parameters as part of the SOARCA uncertainty analysis. The expected range for cladding breakout temperatures, or the temperature at which the oxidized cladding is breached and molten zircaloy is expelled (COR _SC: 1131(2)), from the SOARCA analysis ranges from 2100K (the melting point of Zr) to 2540K (high temperature failure by flowering) [12] [13]. The same temperature range is applied in this analysis.

A second candling model parameter, the maximum molten drainage rate (COR _SC: 1141(2)), was also investigated by the SOARCA uncertainty analysis. The SOARCA limits for this parameter are also applied to this study [0.1 – 2.0 $\frac{\text{kg·m}}{\text{s}}$]. It is noted in the SOARCA analysis that this parameter is exploratory due to a lack of validation data [12] [13].

2.3.3. Fuel Rod Failure Model Parameters

Three fuel rod failure model parameters from section 2.1.3 are included in this analysis. The first parameter is the component critical minimum thickness criteria (COR_CCT: DRZRMN), or $\Delta r_{CL,min}$, which defines the minimum thickness of metallic ZR in cladding components required for fuel rods (fuel and cladding) to remain intact. The range selected for this parameter is [0.0m – 0.00015m]. The minimum represents the case where "bare" fuel pellets and oxidized cladding are self-supporting and remain standing until failure by other criteria. The maximum thickness was selected through engineering judgement and represents failure after the thickness of metallic ZR is reduced below ~20% of the initial clad thickness. Consequently, the minimum thickness is also applied to other ZR-clad components (e.g. CN and CB), however, those components typically fail much earlier due to significantly lower temperature failure criteria (2100K default).

The second fuel rod failure parameter perturbed in this analysis is the fuel failure temperature criteria for oxidized fuel rods, or core component failure parameter COR_SC: 1132(1), which was perturbed for both the eutectics and interactive material models. When liquefaction temperatures of UO2-INT and ZRO2-INT are reduced using the interactive material model, it is recommended to also reduce the temperature criteria for fuel rod failure to the same value. Should the liquefaction temperatures of UO2-INT and ZRO2-INT be set to a value less than COR_SC: 1132(1), forced melting of oxidized fuel rods will occur, effectively lengthening the fuel rod lifetimes. Should the liquefaction temperatures of UO2-INT and ZRO2-INT be set to a value greater than COR_SC: 1132(1), forced collapsed of oxidized fuel rods as solid debris is more likely to occur before UO2-INT and ZRO2-INT reach liquefaction temperatures; candling of oxidized materials is discouraged if not wholly prevented depending on selected values. In the case that liquefaction temperatures of UO2-INT and ZRO2-INT are set equal to COR_SC: 1132(1), liquefaction of UO2-INT and ZRO2-INT may occur prior to oxidized fuel rod collapse into solid debris.Thus, this parameter is set equal to the liquefaction temperature of UO2-INT and ZRO2-INT from section 2.3.1. The distribution was also applied to eutectics model simulations to account for the same physio-chemical interactions leading to early fuel rod failure [13] [14].

Lastly, a discrete uniform distribution is applied to simulations to activate or disable the built-in TaT model (COR_ROD). By default, the TaT model is activated. By disabling the TaT model, fuel rod failure by other failure criteria is forced.

2.3.4. Debris Quenching and Dryout Parameters

The current modelling assumption for component failure and transition to particulate debris, is that 100% of component material becomes particulate debris of user-defined equivalent diameter. Users specify equivalent diameters for each axial level for both particulate debris in the channel (PD) and bypass (PB). In this analysis, two equivalent diameters are used for each simulation: one for particulate debris above the core support plate, in the active core (PD and PB equivalent diameters are set to the same values), and another for particulate debris in the lower plenum (only PD exists in the lower plenum). Equivalent diameters (COR_EDR: DHYPD, DHYPB**)** are selected uniformly from 0.005m – 0.015m, which represents ~50% variation about approximate nominal fuel pellet dimensions (1 cm) for BWR fuel pellets [15]. While partially intact components of much larger dimensions may exist during severe accidents, this analysis assumes that high melting point, heat-bearing fuel debris makes up a significant portion of the total mass of solid particulate debris. Upon relocation to the lower plenum it is assumed that particulate debris will break-up to 0.0001m – 0.005m (COR_EDR: DHYPD**)** or at most, 50% of the nominal fuel pellet length. The lower limit is meant to capture significant rubblization.

In this analysis, the velocity of falling debris (COR_LP: VFALL) is approximated with by a terminal velocity equation. The correlation uses a density averaged across all core materials and is correlated to the particulate debris equivalent diameter in the lower plenum (COR_EDR: DHYPD). The terminal velocity ranges from about 0.1-0.8 m/s.

A discrete uniform distribution is applied to simulations to activate or disable the Lipinski zero-dimensional dryout heat flux correlation (COR_TST: IMPLZDM). By default, the Lipinski zero-dimensional dryout heat flux correlation is turned on. In deactivating the Lipinski zero-dimensional

dryout heat flux correlation, the upper bound of the debris dryout heat flux that approximates the countercurrent flow limitation is removed.

Finally, the default minimum debris porosity (COR _SC: 1244 (3)) in MELCOR is 0.15. Experiments used to develop the zero-dimensional model included debris porosities near 0.4. As such, a range from 0.15-0.4 was selected [10].

2.4. Comparison Methodology

Part I of this benchmark examined baseline model behavior through comparison of single case, best-estimate simulations using each MELCOR material interaction model: (1) the interactive materials model and (2) the eutectics model [1]. Part II broadens the scope of the benchmark to include a comparison of model form differences through parametric uncertainty analysis for each MELCOR material interaction model. Results for each material interaction model parametric uncertainty analysis are organized into the same fundamental categories as part I of this benchmark: overall accident progression, hydrogen generation, thermal hydraulic response, reactor core degradation, and reactor pressure vessel lower head breach. Generally, the figures of merit from part I are revisited in part II with the exception of some thermal hydraulic response variables that do not offer further insight. In lieu of direct comparison of time-dependent horsetails, this analysis focuses on comparison of accident progression snapshots at times near key events in the accident progression such as core plate failure and lower head failure. Insights into model bias and accident progression are derived from interrogation of outcome distributions and clustering as well as identification of outcome correlations and their bases.

3. RESULTS AND DISCUSSION

In the following section, an in-depth comparison between the simulated plant behavior using each material interaction model is presented and discussed. A green/brown color scheme has been used to represent interactive materials and eutectics model simulation outcomes, respectively, for all general comparisons between the two models. A purple/orange color scheme has been used for other comparisons to highlight the impact of TaT model activation/deactivation, respectively. Furthermore, kernel density estimates are provided as a visual aid to illustrate underlying model biases on figures of merit. Kernel density estimates should not be interpreted as "best-estimate" distributions of any figures of merit. Kernel density estimates are not provided for input parameter distributions, which were sampled uniformly across distributions ranges defined in section 2.3. In-depth analysis of model bias and emergent model form differences are interrogated primarily through "snapshot" comparisons, or simulation results taken from a single point in time across all simulations. In this analysis, use of the term significant should be interpreted according to its use in common speech, and not be interpreted as "statistical significance." As in Part I of this analysis, interactive materials (e.g. ZRO2-INT) are denoted, in this section, an "-interactive" suffix [1].

3.1. Overall Accident Progression

The accident progression, characterized by key event timings, of all simulations is shown in Figure 30. Part (a) of Figure 30 highlights core boiloff to top of active fuel (TAF) and bottom of active fuel

(BAF), and the initiation of candling, all indicators of accident progression in the active core region of the RPV. Part (b) of Figure 30 shows core plate failure, lower plenum dryout, and lower head failure; all indicators of late phase in-vessel accident progression. Small differences are observed between exhibited behavior of each model for early indicators of core degradation in the active core region (boiloff to TAF and initial candling). Conversely, late indicators of core degradation in the active core region and in the lower plenum exhibit comparatively large differences in both magnitude and "strength" of clustering, defined here as the relative concentration of observed simulation outcomes. Strong clustering means that simulation outcomes are tightly concentrated about some value, while weak clustering means they are more spread out. In particular, interactive materials model simulations exhibit weaker clustering for core plate failure, lower plenum dryout, and lower head failure than eutectics model simulations. Additionally, the eutectics model exhibits accelerated lower plenum dryout and lower head failure. The impact of each material interaction model on key event timings and the subsequent impact on other core degradation phenomena are explored further in sections 3.4 and 3.5.

Close agreement is observed during the early in-vessel phase of the accident transient (time to RPV boiloff to the TAF) between all simulations. Differences between simulations using either material interaction model are also relatively small. The variance that can be observed in the time to TAF is explained by numerical uncertainty associated with the thermal hydraulic solution matrix. No other uncertain parameters (including material interaction model choice) can explain the variance in time to TAF because core degradation has not begun.

Observable differences between the behavior exhibited by each material interaction model begin to appear at the onset of the late in-vessel phase of the accident (i.e. the loss of coolable rod-like geometry) consistent with past observations. As in part I of the analysis, the initiation of candling is used as the indicator for the onset of the late in-vessel phase of the accident [1]. Both material interaction model simulation sets exhibit strong clustering for the initiation of candling, however, the eutectics model simulations exhibit stronger clustering than the interactive material model simulations. Candling initiates in all simulations within a time window approximately 5 minutes long. The interactive materials model has simulation outcomes spanning the last four minutes of the time window, while the eutectics model simulation outcomes span approximately the first minute of the window. Earlier candling by the eutectics model is due to the reduced melting points of core material pairs, whereas the interactive materials model liquefies materials at their individual melting points.

At the time core boiloff, when the water level reaches the bottom of the active fuel (BAF), the small time differences in the initiation of the late in-vessel accident phase between cases, indicated by candling, have evolved into larger temporal differences in the accident transients, even hours in some cases, as observed in the points that form the upper tails of both material interaction model distribution. The majority of simulations for both models exhibit boiloff timings clustered about 4 hours; core boiloff (TAF to BAF) is clustered about 1.4 hours for both material interaction models. Delayed boiloff is observed for simulations using each material interaction model. The delays in core boiloff are larger for the eutectics model than the interactive materials model. Furthermore, the interactive materials model exhibits stronger clustering of simulation outcomes for core boiloff to BAF about 4 hours. This behavior is consistent with the observations of core degradation near 4 hours. Namely, that interactive materials model simulations exhibit strong clustering of intact fuel rod masses (near 100%) beyond 4 hours as well as stronger clustering in total intact mass fraction of the core near 4 hours (discussed later). Conversely, eutectics model simulations exhibit weaker

clustering of the intact fuel rod mass at 4 hours, and consequently feature early relocation of heat bearing materials, contributing to the weaker clustering of boiloff time to BAF.

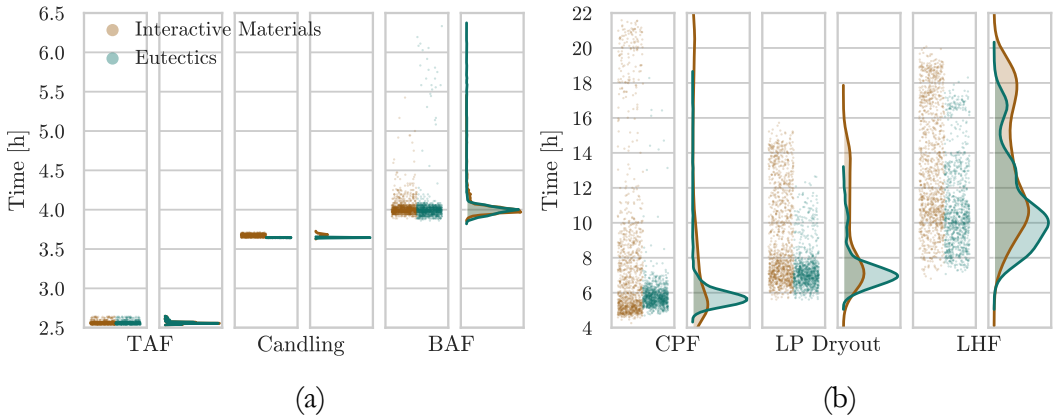

Figure 30. Event progression summary strip plot (scatter plot with one categorical axis). The x-axis shows categorical events; TAF: top of active fuel, Candling: onset of candling, BAF: bottom of active fuel, CPF: core plate failure, LHF: lower head failure. The y-axis shows the event timing for every realization and event category.

Core plate failure observed to occur by times between 5.5-6.5 hours in a significant number of simulations for both material interaction models, however, both material interaction model simulations sets contain simulations with much later core plate failure. Both models exhibit multiple simulations in which core plate failure occurs after lower plenum dryout. And some simulations using the interactive materials model even calculated core plate failure after lower head failure, an observation that is discussed in more detail below. Eutectics model simulations exhibit stronger clustering for time of core plate failure than interactive materials model simulations. In the following sections, snapshots at both 5.5 and 6.5 hours are revisited to demonstrate the transition from degradation in the core region to the lower plenum.

Lower plenum dryout is primarily clustered about 7 hours for simulations using both material interaction models. Clustering is stronger for eutectics model simulations. Time differences between lower plenum dryout and core plate failure outcomes (not shown) are clustered about 1 hour for eutectics models and 1.5 hours for interactive materials models. Differences between lower plenum dryout and BAF outcomes are clustered about 3 hours for both material interaction models, though the interactive material model simulations exhibit a larger number of cases with greater differences (not shown).

Finally, primary lower head failure clusters for both material interaction models are centered about ~10 hours with eutectics model simulations exhibiting stronger clustering. In the following sections, snapshots at both 10.3 hours are revisited to demonstrate the transition from the in-vessel accident phase to the ex-vessel accident phase. Features of the lower head failure distribution are further analyzed in section 3.5.

In summary, small differences are observed in key event timings during the early in-vessel phase of the accident across all simulations. After the onset of the late in-vessel phase of the accident, increased variation in key event timings is observed in simulations. The distributions for key event

timings shows different characteristics for each material interaction model simulation set during the late in-vessel phase of the accident. In particular, the eutectics model simulations exhibit stronger clustering in occurrence of core plate failure, lower plenum dryout, and lower head failure.

3.2. Hydrogen Generation

Figure 31 shows the hydrogen generated after 25.0 hours for all materials (TOTAL), Zr, stainless steel, and B_4C. Eutectics model simulations exhibit clustering about lower magnitudes of hydrogen generation for all material categories. Outcome clustering for the eutectics model is clustered about 600 kg for total in-vessel hydrogen generation, 500 kg for Zr, 85 kg for stainless steel, and 10 kg for B_4C. For interactive materials model simulations, outcomes cluster about 760 kg for total in-vessel hydrogen generation, 570 kg for Zr, 160 kg for stainless steel, and 20 kg for B_4C. This observation is consistent with accelerated debris relocation to the lower plenum and subsequent boiloff also exhibited by the eutectics model, that terminates the oxidation reaction of cladding components prematurely through earlier relocation of materials to lower, cooler core elevations. Eutectics model simulations also exhibit stronger clustering for hydrogen generation by stainless steel and B_4C than interactive materials model simulations. In the case of B_4C, eutectics model simulations inhibit further chemical reactions with B_4C after it has become part of a eutectic mixture. Conversely, common practice for interactive material modeling of B_4C /stainless steel material interactions in BWR control blades is employed – control blades fail at a user-specified B_4C /stainless steel interaction temperature (see section 2.3.1) and relocate the component mass as PD – which can promote further oxidation of the B_4C and stainless steel materials after subsequent uncovery through increased surface area.

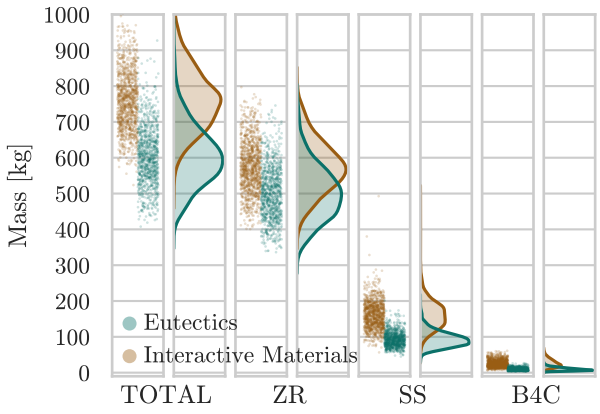

Figure 31. Strip plot of in-vessel, integral hydrogen generation from core material oxidation after 25.0 hours. The x-axis shows categories of core materials that can produce hydrogen during oxidation; TOTAL: all materials, ZR: zirconium, SS: stainless steel, B4C: boron carbide. The y-axis shows integral hydrogen generation (after 25.0 hours) through oxidation of a given material for every case.

Figure 32 shows the distribution of hydrogen generation across rings 1-5 of the active core; ring 1 is the centermost ring. The interactive materials model simulations exhibit clustering about higher magnitudes of hydrogen generation in all rings; the hydrogen generation distribution for rings 1-4 is centered ~25 kg higher. Similar strength of clustering is observed between each material interaction models for the three inner core rings, whereas the interactive materials model is slightly more strongly clustered in ring 4 than the eutectics model and the eutectics model is more strongly

clustered in ring 5 than the interactive materials model. Interactive material model simulations exhibit bimodal distribution characteristics in ring 5; the central region of the entire distribution for interactive material model simulation outcomes is ~80-100kg more than the central region of the eutectics model cluster. Also, a significant number of interactive materials model simulations outcomes are ≥150 kg more than the central region of the eutectics model cluster in ring 5; the second distribution peak occurs ~50 kg higher than the maximum eutectics model simulation outcome. As with the differences in overall in-vessel hydrogen generation, the differences in the distribution of hydrogen generation are consistent with accelerated relocation of debris to the lower plenum and lower plenum boiloff. Further interrogation of the hydrogen generation distribution reveals that during core boiloff, the interactive materials model simulations exhibit significant hydrogen generation in ring 4, while eutectics model simulations exhibit suppressed hydrogen generation in ring 4 during the same timeframe. During core boiloff, hydrogen generation in ring 5 is comparable between both models. Subsequently, during lower plenum boiloff, eutectics model simulations exhibit significant hydrogen generation in ring 4 to similar magnitudes observed for interactive materials model simulations at the same time. During the same period, interactive materials model simulations exhibit less hydrogen generation in ring 4, and significant hydrogen generation in ring 5.

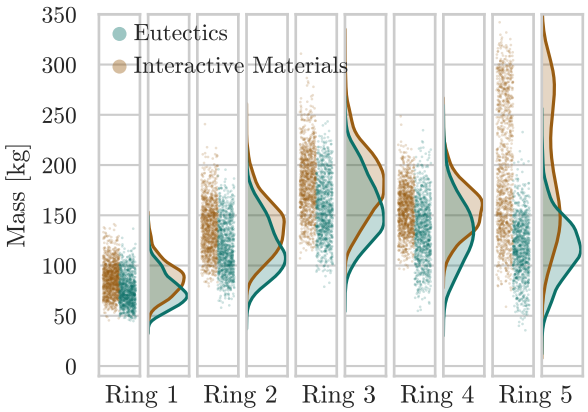

Figure 32. Strip plot of in-vessel, integral hydrogen generation in radial core rings after 25.0 hours. The x-axis shows radial core rings; ring 1 is the innermost ring and ring 5 is the outermost ring in the active core region. The y-axis shows integral hydrogen generation (after 25.0 hours) through core material oxidation in a given core ring for every case.

To summarize, interactive materials model simulations generally exhibit greater masses of hydrogen generation by all materials and in all core rings. Total hydrogen generation is clustered about 760 kg for interactive materials model simulations and 600 kg for eutectics model simulations. Generally, interactive materials model simulations exhibit clustering about magnitudes ~25 kg larger than eutectics model simulation in rings 1-4. Much larger differences are observed in ring 5 hydrogen generation with clustering of interactive materials model simulations centered 150 kg more than the center of the eutectics model simulation cluster.

3.3. Thermal Hydraulic Response

No thermal hydraulic model parameters were perturbed as part of this uncertainty analysis. Thermal hydraulic phenomena are, however, indirectly affected by other parameters, and thus their behavior is analyzed here.

3.3.1. Primary Coolant System Response

The thermal hydraulic response to the transient in the primary coolant system follows behavior exhibited in part I of this analysis [1]. The steam dome pressure transient is trivial for the high pressure ejection scenario modeled and thus not included. Steam dome pressure remains high, between the SRV opening and closing setpoints, during RPV boiloff. SRV operation continues until RPV lower head failure. After lower head failure, pressure in the steam dome is at equilibrium with the drywell.

Conversely, insightful features emerge in other thermal hydraulic figures of merit. In particular, features are observed during the transition from active core to lower plenum degradation marked by core plate failure, and the transition from the in-vessel to the ex-vessel accident phase marked by lower head failure, and are presented in snapshots taken at 5.5-6.5 hours and 10.3 hours, respectively.

RPV water level at 5.5 hours is shown in Figure 33. While the eutectics model exhibits greater debris masses in the lower plenum and reduced RPV water level in many simulations at 5.5 hours, the boiloff transient follows a similar pattern for both models. At 5.5 hours it is observed that the water level clustering is centered approximately 1.0-1.5 meters below BAF and the mass of debris in the lower plenum is < 30Mg prior to core plate failure for both material interaction models. After core plate failure, however, both material interaction models exhibit increased variability in RPV water level due to a buildup of hot debris in the lower plenum. Accelerated fuel degradation, discussed in section 3.4, contribute to more rapid boiloff exhibited by eutectics model simulations.

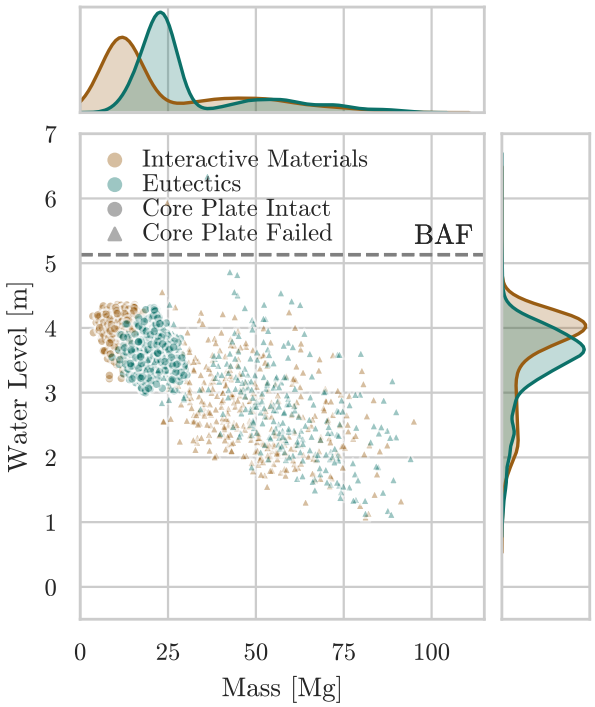

Figure 33. RPV water level (y-axis) relationship with debris mass in the lower plenum (x-axis) at 5.5 hours. Marker types represent core plate damage states; circle: core plate intact, triangle: core plate failed.

Figure 34 shows a snapshot of steam dome temperature at (a) 5.5 and (b) 10.3 hours. At 5.5 hours, Figure 34 (a), two clusters of outcomes are observed that are dependent on the damage state of the core plate. Before core plate failure, steam dome temperatures exhibit similar clustering for both material interaction models. Steam dome temperatures are clustered about lower magnitudes for the eutectics model simulations. After core plate failure, hot debris accumulates in the lower plenum and the lower plenum dries out. During lower plenum boiloff, limited convective heat transfer by steam cause steam dome temperatures to decrease and superheated gases in the RPV are ejected through the SRV to the suppression pool. Both material interaction model simulation sets follow similar pathways to lower plenum dryout, however, steam dome temperatures are observed to cluster about lower magnitudes in eutectics model simulations. Lower steam dome temperatures are indicative of comparatively less convective heat losses in the core and consequently higher core component temperatures and core structure degradation, which is consistent with the greater degree of fuel degradation generally observed in eutectics model simulations at 5.5 hours (discussed in section 3.4).

After lower plenum dryout, temperatures increase by radiation, in pseudo-linear fashion as discussed in part I of the analysis [1]. This period of steam dome heatup is captured in Figure 34 (b). At 10.3 hours, two major clusters of outcomes are observed for each material interaction model that relate to lower head damage states – lower head intact or failed. Prior to lower head failure, the steam dome temperatures are clustered about 1100K for lower plenum debris masses >50 Mg. Simulations with lower plenum mass <50 Mg exhibit an inverse relationship with steam dome temperature and can be largely divided into subclusters dependent on core plate damage state – core plate intact or failed. Generally, simulations with an intact core plate have the lowest lower plenum debris masses and highest steam dome temperatures, however, a small number of interactive materials model simulations exhibit high steam dome temperatures after core plate failure. The steam dome temperatures before core plate failure are higher because of the greater masses of heat bearing materials in the active core. In particular, interactive materials model simulations exhibit much higher steam dome temperatures prior to core plate failure. These temperatures are the result of prolonged fuel lifetimes exhibited by some simulations with the TaT model turned off, discussed in section 3.4. Furthermore, the connectedness of the two subclusters (before and after core plate failure) is indicative of the transition to lower plenum dryout and heat rejection through the SRV after core plate failure. After lower head failure, significant energy is ejected into containment, including a significant mass of core materials. The massive ejection of energy and mass, in particular heat bearing materials, caused by gross lower head failure leads to reduced steam dome temperatures and lower plenum debris masses. Strong agreement is observed between clustering exhibited by both material interaction models after lower head failure.

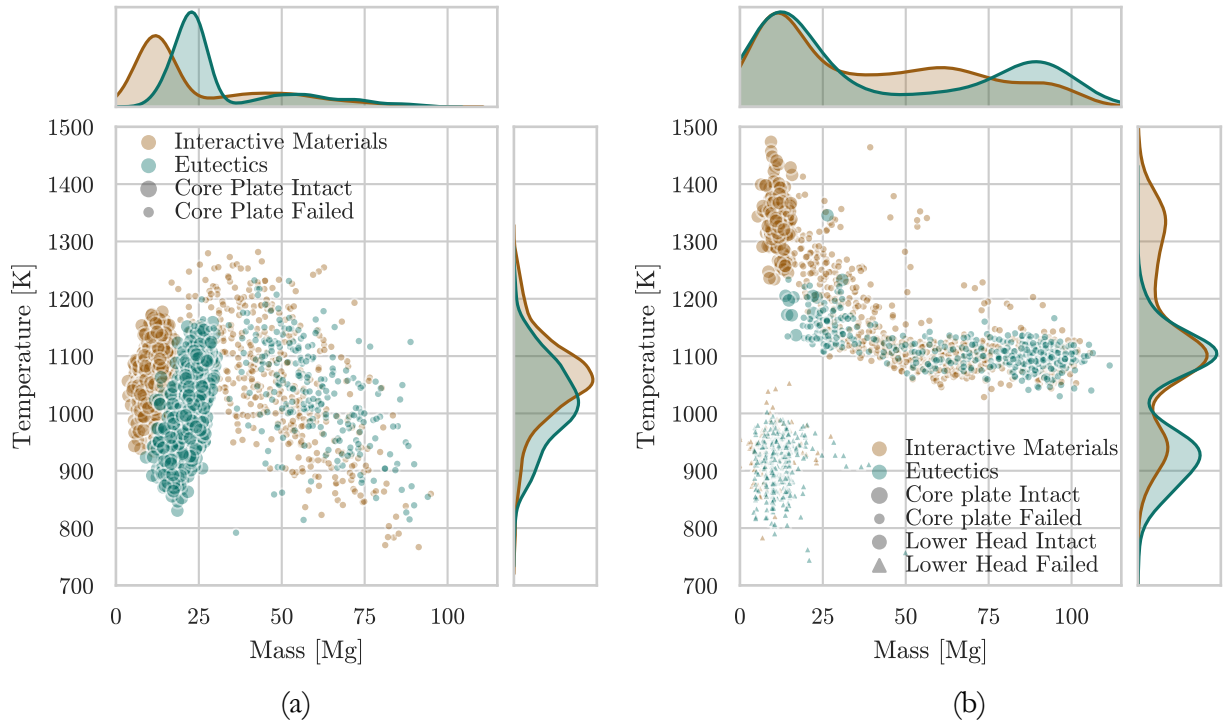

Figure 34. Steam dome temperature (y-axis) relationship with debris mass in the lower plenum (x-axis) at (a) 5.5 hours and (b) 10.3 hours. Marker sizes represent core plate damage states; large: core plate intact, small: core plate has failed. Marker types represent lower head damage states; circle: lower head intact, triangle: lower head failed.

3.3.2. Containment Response

Figure 35 shows a snapshot of the containment response to the transient, drywell pressure dependence on in-vessel hydrogen generation during the transition from the in-vessel to the ex-vessel phase of the accident. Two major clusters of outcomes (a gross bifurcation) are observed and distinguished by the damage state of the lower head (lower head intact or failed). Both clusters exhibit a strong relationship between in-vessel hydrogen generation and drywell pressure. As discussed previously the interactive materials model exhibits greater in-vessel hydrogen generation because of the prolonged component lifetime, fuel components in particular, and greater degree of oxidation of core components. Similarly, the drywell pressure clusters for the interactive materials model simulations are centered about larger magnitudes than the eutectics model simulations because of the greater masses of noncondensible gases (e.g. hydrogen). While the interactive materials model outcomes cluster about greater hydrogen masses and drywell pressures than eutectic materials model outcomes, the relationship between the two figures of merit is seemingly unaffected by the material interaction model choice. Both material interaction models exhibit a similar relationship between hydrogen generation and drywell pressure, indicating that the relationship is not dependent on the core damage pathway (which is not shared between the two simulation sets) or material interaction model choice, but is dependent on the core damage state (i.e. lower head failure) and is plant dependent (free volume in containment volume, etc.). While the behavior is not core damage pathway dependent, it is event specific, for example, a different primary depressurization pathway is unlikely to result in the same drywell pressure – hydrogen mass relationship.

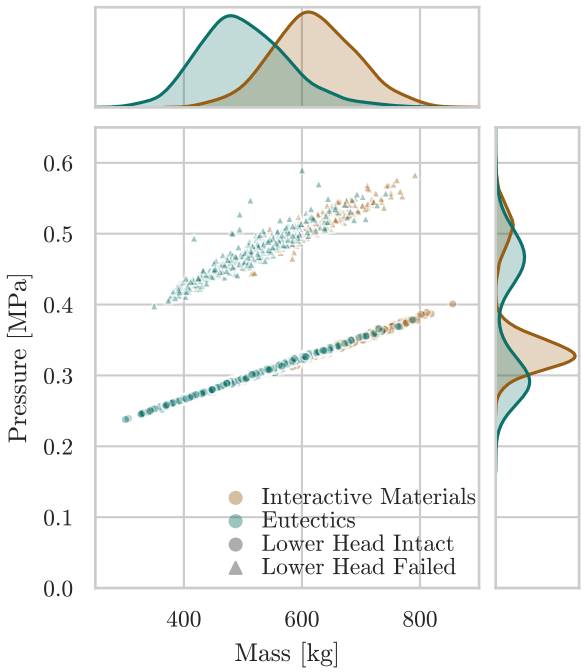

Figure 35. Drywell pressure (y-axis) dependence on in-vessel hydrogen generation (x-axis) at 10.3 hours. Marker types represent lower head damage states; circle: lower head intact, triangle: lower head failed.

As in the case of steam dome pressure, the wetwell pressure transient is trivial and matches closely with the drywell pressure transient as observed in part I of this analysis [1]. Furthermore, the suppression pool temperature was not observed to exceed saturation in any simulation.

In summary, thermal-hydraulic phenomena exhibit similar progression throughout the transient, across all simulations, regardless of material interaction model choice. Conversely, large variation in thermal hydraulic behavior is observed between core damage states and events such as core plate failure and lower head failure. In particular, a strong relationship is observed between hydrogen generation and drywell pressure before and after lower head failure.

3.4. Reactor Core Degradation

The loss of rod-like geometry and build-up of debris in the core region obstructs coolant flow through the core inhibiting core cooling. Figure 36 shows a snapshot at 5.5 hours of the average minimum-normalized axial flow area of the core and its relationship with the overall intact mass fraction of the fuel. Component intact mass fractions (e.g. cladding and fuel) are computed as in Part I of this analysis – the mass of the primary component material (cladding: Zr, Fuel: UO_2, fuel canister: Zr, control blade: B_4C) at a given time divided by the initial mass of the material in that component [1]. Losses of the primary component material by melting, oxidizing, or otherwise relocating all decrease the intact mass fraction of core components. To obtain the minimum normalized axial flow area of the core, an average is taken of the minimum normalized axial flow areas in each core ring; normalized axial flow areas are obtained by dividing the flow area available to coolant at a given time by the initial flow area available to coolant as in Part I of this analysis. When core materials relocate, it is possible for the open area available to coolant to grow larger the initial value, which allows normalized axial flow areas > 1.0 to occur. Prior to core plate failure both

material interaction models exhibit a relationship between intact fuel mass fraction and normalized axial flow area, whereby increased intact fuel mass fraction is related to increased normalized axial flow areas. The eutectics model exhibits stronger clustering for both smaller intact fuel mass fractions and smaller normalized axial flow areas that the interactive materials model before core plate failure. After core plate failure, a discrete discontinuity in normalized axial flow area can be observed for both material interaction model simulations, as a gap from ~0.2 to ≥0.4 normalized axial flow area, due to the opening of a flow channel previously obstructed by the core plate and held-up debris. MELCOR models gross failure of the core plate in each ring of the core. After failure of the core plate, normalized axial flow area may increase > 1.0 due to the availability of cross-sectional area previously occupied by core SSCs. The distribution of intact fuel fraction outcomes after core plate failures is clustered about smaller magnitudes than prior to core plate failure. This observation is consistent with the support structure model applied to the core plate – failure of the core plate causes failure of any supported structures. As stated previously, the eutectics model simulations exhibit clustering about both smaller intact fuel mass fractions and normalized axial flow area in comparison to the interactive materials model.

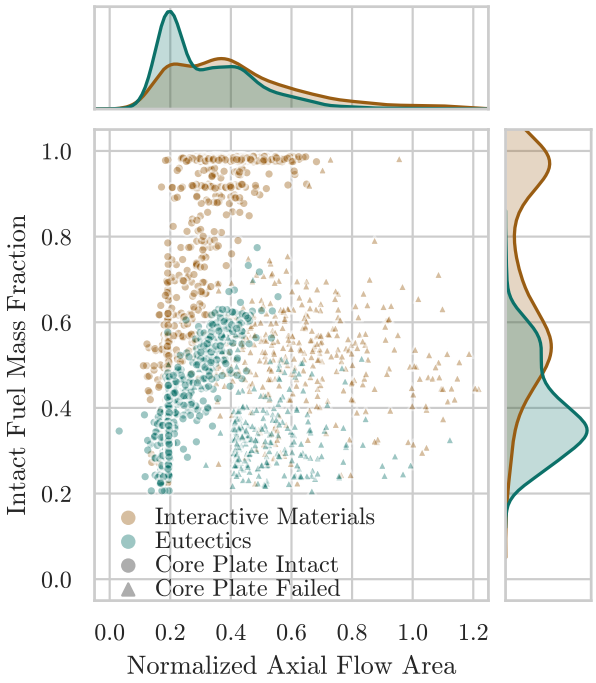

Figure 36. Normalized axial flow area of the core (x-axis) relationship with fuel intact mass fraction (y-axis) at 5.5 hours. Marker types represent core plate damage states; circle: core plate intact, triangle: core plate failed.

Figure 37 shows the relationship between the molten mass and normalized axial flow area of the core at 5.5 hours. The transient nature of molten materials can be difficult to capture by snapshots in time of the accident progression, however, by focusing on transition periods, insights may still be drawn. At 5.5 hours, prior to lower head failure, the eutectics model simulations exhibit larger molten masses than interactive materials model simulations. Both models also exhibit some level of correlation between large molten pool masses and small normalized axial flow area, consistent with the reduced coolant flow associated with a blockage. Eutectics model simulations that exhibit core plate failure by 5.5 hours are observed to have larger molten masses than interactive materials model

simulations. Furthermore, after core plate failure, the molten masses are not observed to be as larger and the axial flow area is observed to increase.

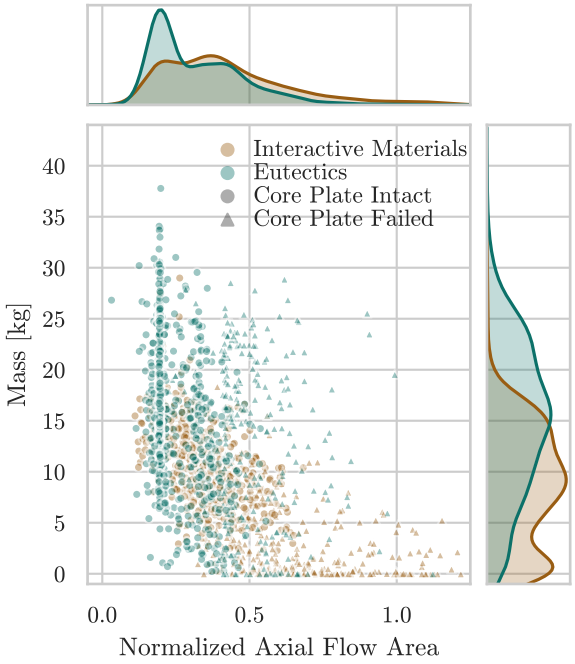

Figure 37. Molten mass (y-axis) relationship with the normalized axial flow area of the core (x-axis) at 5.5 hours. Marker types represent core plate damage states; circle: core plate intact, triangle: core plate failed.

A summary of core damage progression is shown at (a) 4.5 hours and (b) 6.5 hours in Figure 38. Intact mass fractions for UO_2 in fuel components, Zr in cladding components, Zr in fuel canister components (CN+CB) and B_4C in control blade structures (non-supporting structure components, NS), the control blades, are used as indicators of core damage progression. The overall core damage state is also represented by the summation of mass of each primary material for each core component in the core region (TOTAL). It should be noted that for the purpose of this analysis oxidized Zr is removed from the "intact" mass fraction. Thus, smaller intact mass fractions of Zr and B_4C based structures are consistent with greater oxidation of those structures, as indicated by larger hydrogen generation in section 3.2, and do not necessarily indicate failure of the structure. Even at 4.5 hours, significant degradation of some core structures is observed for both material interaction models, however, the interactive materials model simulations exhibit greater degradation of control blade, fuel canister, and cladding components as demonstrated by clustering about lower intact mass fractions in Figure 38 (a). Further investigation into the distribution of intact components reveals that differences in core-wide component degradation at 4.5 hours between the material interaction simulation sets shown in Figure 38 (a), are primarily the result of differences in ring 4 degradation at that time (not shown), with minimal differences in ring 5; interactive materials model simulations generally exhibit significant degradation of ring 4 components, while eutectics model simulations generally exhibit only partial degradation in ring 4. Conversely, the eutectics model simulations exhibit significantly greater degradation of fuel components in all core rings when compared to interactive materials model simulations.

Similar trends are observed at 6.5 hours in Figure 38 (b); distributions of the interactive materials model simulation outcomes exhibit greater clustering about lower intact mass fractions for control blade, fuel canister, and cladding components. However, the extent of damage to Zr-based components is in greater agreement. Further investigation into the distribution of intact components reveals that differences observed in core-wide control blade, fuel canister, and cladding component degradation shown in Figure 38 (b) are primarily due to differences in ring 5 degradation (not shown). Between 4.5 hours and 6.5 hours, eutectics model simulations generally exhibit significant degradation of ring 4 control blade, fuel canister, and cladding components (not shown), reaching similar levels of degradation for the same components in ring 4 of interactive materials model simulations (not shown), and only partial degradation of the same components in ring 5 (not shown). Conversely, interactive materials model simulations generally exhibit significant degradation of control blade, fuel canister, and cladding components in ring 5 (not shown). Control blade components are observed to be in a more degraded state for many interactive materials model simulations, which cluster about 0.05 intact mass fraction, whereas eutectics model simulations cluster about 0.2 intact mass fraction. The disparity between the two models is the consequence of different levels of control blade degradation observed in the outermost core rings; eutectics model simulations exhibit less control blade degradation in both rings 4 and 5 at 6.5 hours. Large differences between model outcomes are also observed for fuel components. The eutectics model exhibits significant fuel degradation at 6.5 hours, with significantly stronger clustering about 0.3 intact mass fraction relative to the interactive materials model, which is near uniformly distributed from ~0.2 to ~1.0 intact mass fraction. As before, eutectics model simulations generally exhibit greater degradation of fuel components in all core rings when compared to interactive materials model simulations.

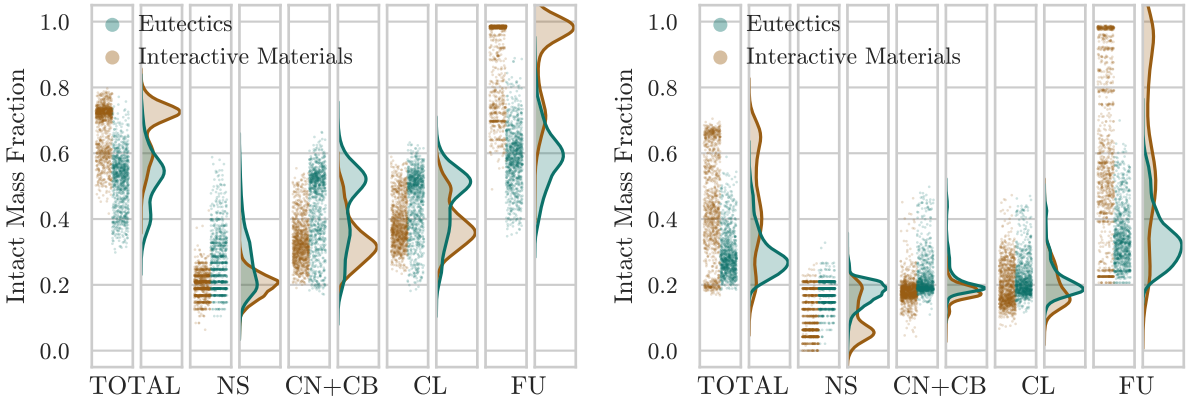

Figure 38. Component damage progression strip plots at (a) 4.5 hours and (b) 6.5 hours. The x-axis shows categories of core components; TOTAL: total core (all core components), NS: non-supporting structure (control blade), CN: fuel canister, CL: fuel cladding, FU: fuel. The y-axis shows the intact mass fraction of each component category for every realization.

Maximum component temperatures observed in the core region over the entire simulation length are shown in Figure 39. Eutectics model simulations exhibit distributions that peak at higher maximum temperatures for control blade, cladding, and fuel component types in the core region; higher maximum temperatures for fuel and cladding components are expected in the eutectics model simulations because the melting points of the constituent materials have not been reduced. Reported control blade structure temperatures include both stainless steel structures and stainless

steel/B_4C control blade structures. Control blade structures are observed to reach maximum temperatures between 1520K and 1700K, the same range as the TNSMAX parameter. While not all control blade structures were observed to fail at the TNSMAX parameter setpoint, the TNSMAX setpoint was observed to correspond the lowest maximum temperatures of control blade structures observed; eutectics model simulations were observed to exceed the TNSMAX setpoint more often than interactive materials model simulations as demonstrated by clustering about greater maximum control blade temperatures in Figure 39. Fuel canister structures maximum temperatures are observed to reach the parametric collapse temperature setpoint 2100K, which coincides with the default melting point of Zr. In experiments, interactions between fuel canister and control blade materials has been observed to occur at temperatures below 2100K [16]. Early failure of fuel canister structures in experiments is attributed to material interactions between Zr and Fe in the fuel canister and control blade, respectively. The eutectics model treats Zr/stainless steel material interactions in conglomerate debris, however, there is no mechanistic treatment of early control blade-fuel canister interactions due to Zr/stainless steel material interactions. Dissolution of unoxidized stainless steel by Zr is also not currently captured by the eutectics model. Greater variability is observed, relative to control blade and fuel canister components, in the maximum temperatures reached by both cladding and fuel components for both material interaction models. The greater degree of variability can be attributed to the competition and interaction between the different fuel failure models in MELCOR. Generally, eutectics model simulations, however, exhibit elevated maximum cladding and fuel temperatures, the basis of which is explored in greater detail below.

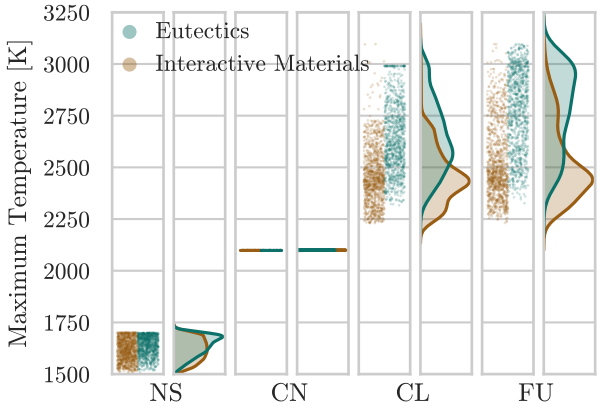

Figure 39. Maximum component temperature strip plot. The x-axis shows categories of core components; TOTAL: all core components, NS: non-supporting structure (control blade), CN+CB: fuel canister, CL: fuel cladding, FU: fuel. The y-axis shows the intact mass fraction of each component category for every realization.

Figure 40 shows a snapshot at 6.5 hours of the relationship between cladding damage progression, cladding breach temperature (COR _SC: 1131(2)), TaT model status, and the inequality of the breach temperature and relocation temperature (COR_SC: 1132(1)) for each set of material interaction model simulations. As discussed above in reference to Figure 38 (b), interactive material model simulations exhibit cluster peaks at slightly lower cladding intact mass fractions at 6.5 hours than eutectics model simulations. Cladding intact mass fraction does not exhibit a strong dependence on TaT model state for either material interaction model simulation set. This is because the major phenomena contributing to the reduction of intact cladding mass is oxidation, and not gross cladding failure. A dependence is observed, however, on both breach temperatures and the relationship between breach temperature and relocation temperature for interactive materials model simulations. Lower breach temperatures, which allow candling of Zr, are associated with greater

degradation of the cladding component. Interactive materials model simulations for which breach temperature was greater than relocation temperature exhibit less cladding damage; cladding damage is defined here as the loss of intact Zr mass either through oxidation, melting, or particulate debris formation. In these cases, damage to cladding components is inhibited because the parameter combination promotes temperature-based component melting/failure before temperature-based candling. While fuel rod collapse before cladding breach and subsequent candling is a less common phenomenological pathway, it cannot be excluded from the uncertainty space. The same dependencies are not observed for eutectics model simulations, which show no obvious dependence of cladding damage on any of the breach temperature, TaT model status, or the breach temperature and relocation temperature inequality. The results indicate greater overlap (minimum to maximum) between distributions for the intact cladding mass fraction for each material interaction model simulation set for greater breach temperature input parameters, when the breach temperature setpoint is greater than ~2350 K.

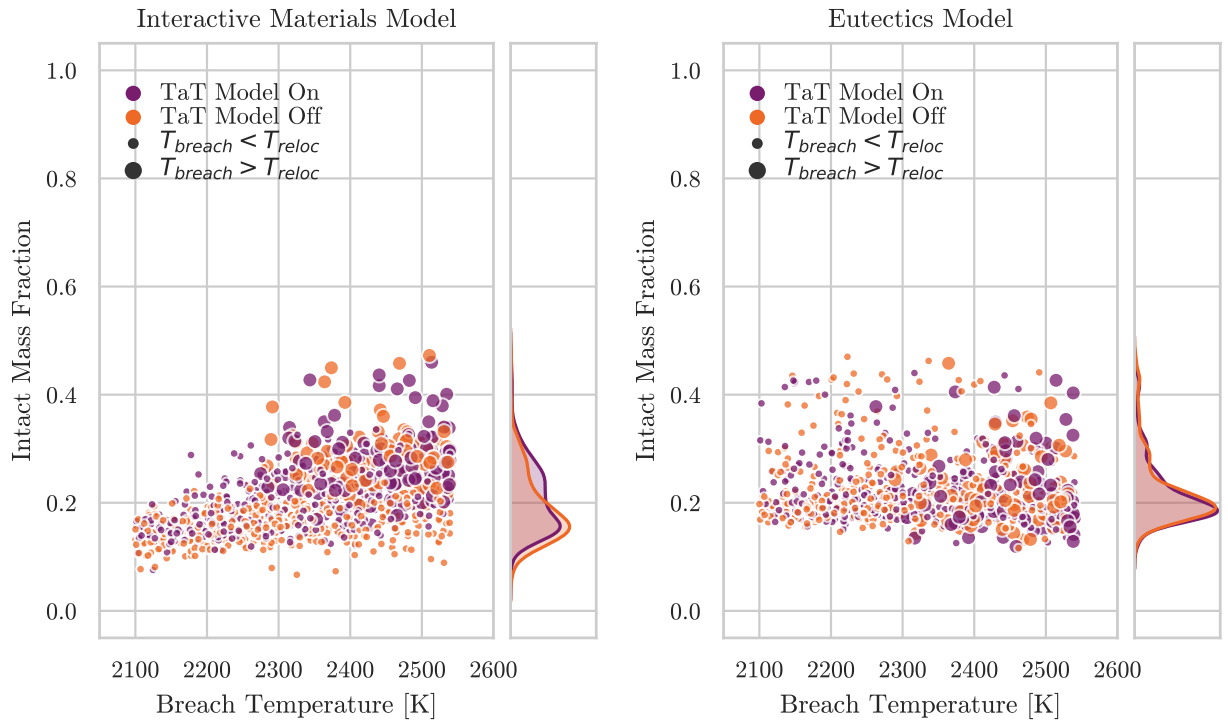

Figure 40. Cladding damage progression (y-axis) relationship with breach temperature (x-axis) at 6.5 hours. Marker sizes represent the relationship between the breach and relocation temperatures; small: $T_{breach} < T_{reloc}$, large: $T_{breach} > T_{reloc}$.

Figure 41 shows the relationship between maximum cladding temperature reached during the transient, relocation temperature, TaT model status, and the inequality between Δr_{hold} (R_{hold}), the minimum oxide thickness required to "hold-up" the molten materials discussed in section 2.1.2, and the thickness of the oxide layer (OXTH). MELCOR does not activate the relocation temperature setpoint (SC 1132(1)) until breach of the cladding and candling of all metallic Zr has occurred, i.e. when OXTH < R_{hold}. Visibly different behavior between the two sets of simulations are observed. In particular, TaT model status strongly impacts maximum cladding temperatures for the interactive materials model. When the TaT model is active, very few interactive materials model simulations exhibit maximum cladding temperatures above the relocation temperature setpoint. Cases that do

exhibit maximum temperatures above the setpoint do not exceed it significantly. Conversely, when the TaT model is deactivated, the majority of simulations exhibit maximum cladding temperatures equal to the relocation temperature setpoint. Some simulations are observed to exceed this setpoint. When the TaT model is turned off, maximum temperatures can exceed the relocation temperature setpoint so long as OXTH > R_{hold} and metallic Zr is still present. Thus, it is suspected that these cases exceeded the setpoint before it was activated internally due to thick oxide layers that slowly melted until OXTH < R_{hold} became true and the rod subsequently collapsed. Under these conditions, the remaining cladding mass before rod failure would be small and heating it in excess of the liquefaction temperature would be possible. The same behavior is not exhibited by eutectics model simulations, which exhibit no visible dependence of maximum cladding temperature on relocation temperature or the relationship between OXTH and R_{hold}. The lack of dependence on relocation temperature and the relationship between OXTH and R_{hold} can be explained by the fact that liquefaction of UO_2 and ZrO_2 does not occur at the relocation temperature setpoint in eutectics model simulations. Thus, heat transferred to the component is added as sensible heat and increases component temperatures instead of transferring as latent heat, and slowly melting/draining component materials causing a temperature stall. Finally, a slight dependence on TaT model status is observed for eutectics model simulations. Maximum cladding temperatures are clustered about a slightly lower magnitude when the TaT model is on. This behavior is not unexpected, as the fuel rod lifetime becomes shorter at higher temperatures, and heat-up to extreme temperatures requires similarly extreme heat-up rates. It is possible that this difference is due to a potential cluster about maximum cladding temperatures of ~2990 K for eutectics model simulations with the TaT model turned off. Generally, when the TaT model is off, eutectics model simulations exhibit a nearly uniform distribution of cladding temperatures, with a number of cases that reach the default ZrO_2 melting point (2990K) regardless of the relocation temperature setpoint. This requires that the OXTH > R_{hold} for the duration of at least some fuel rod lifetimes.

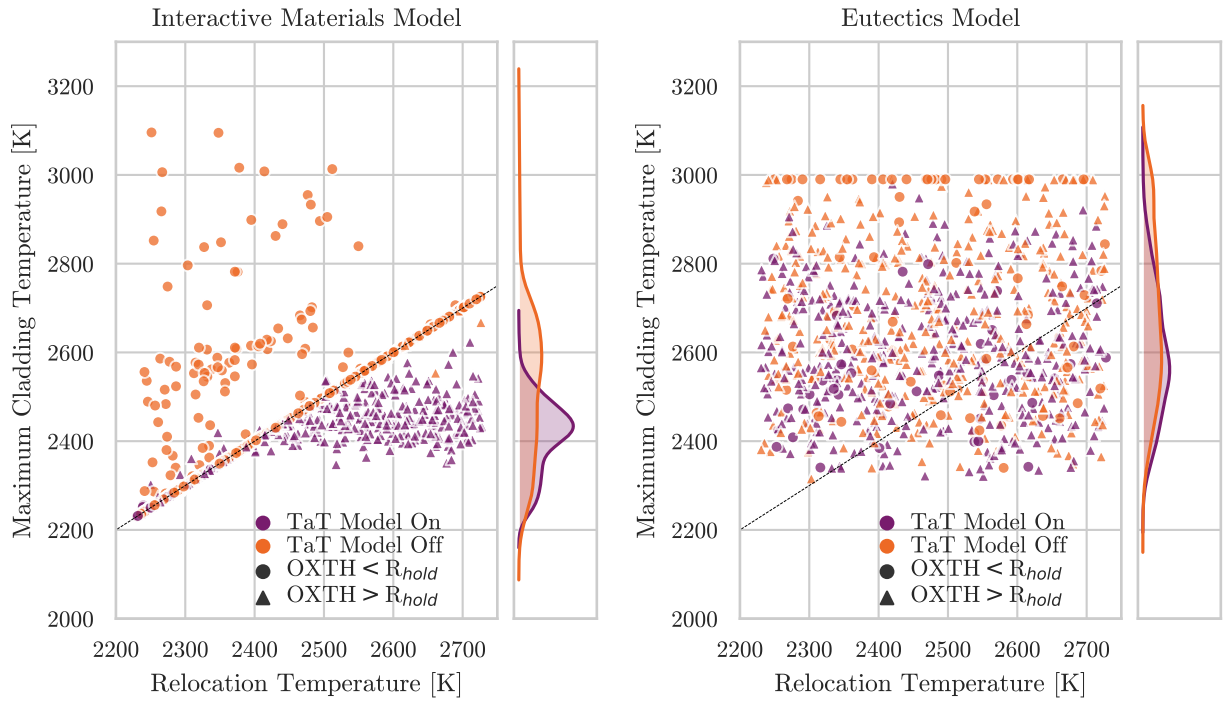

Figure 41. Maximum cladding temperature (y-axis) relationship with relocation temperature (x-axis). Marker types represent the integrity of the cladding oxide layer; circle: OXTH $<$ R_{hold} (cannot hold up molten materials), triangle: OXTH $>$ R_{hold} (can hold up molten materials).

A snapshot at 6.5 hours of fuel damage progression is shown in Figure 42. While eutectics model simulations exhibit a slight dependence on TaT model status, interactive materials model simulations show a strong dependence on TaT model status. When the TaT model is turned off, a significant number of interactive materials model simulations exhibit near-fully intact fuel (~0.8-~1.0 intact mass fraction), even at relocation temperature setpoints < 2500K. For interactive materials model simulations, the intact fuel mass fraction dependence on TaT model status is less pronounced when the breach temperature is greater than the relocation temperature. The range of intact fuel mass fractions for interactive materials model simulations are in much greater agreement with eutectics model simulations when the TaT model is turned on than when it is turned off and is generally between 0.2 – 0.6 intact mass fraction. Eutectics model simulations behavior is not visibly affected by the relocation temperature setpoint, or its relationship with breach temperature, but the TaT model appears promote slightly accelerated fuel rod degradation as demonstrated by the small difference in cluster peaks.

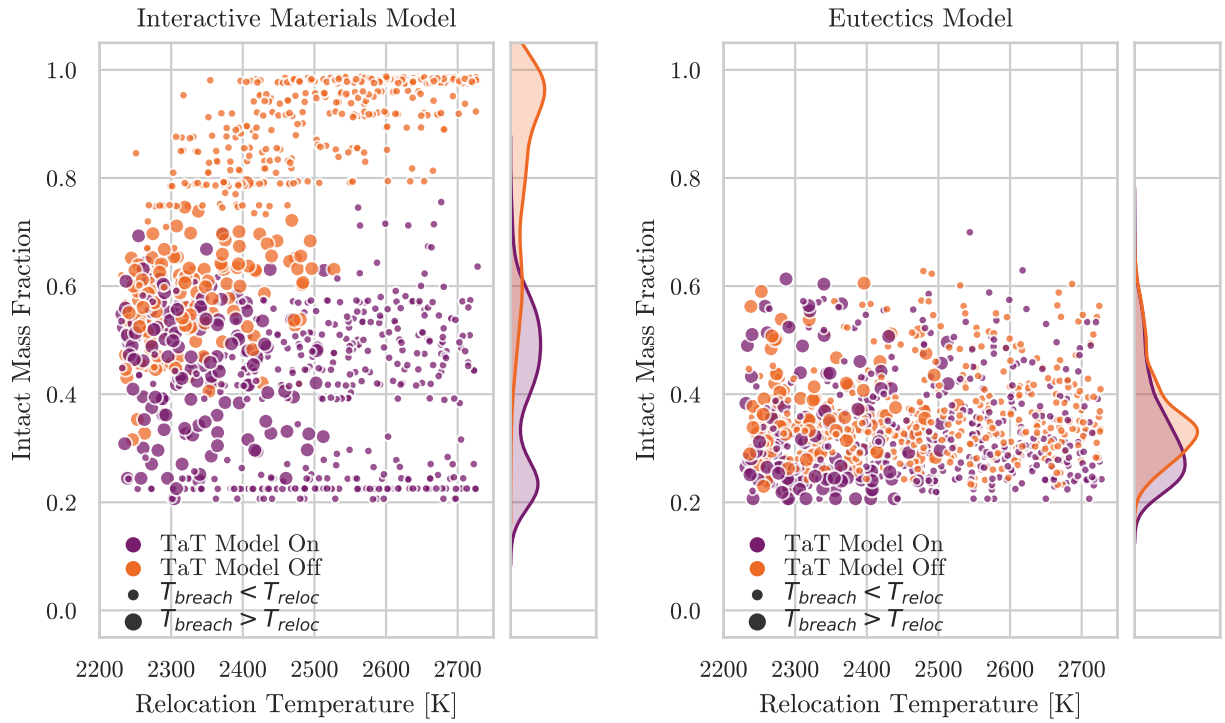

Figure 42. Fuel damage progression (y-axis) relationship with relocation temperature (x-axis) at 6.5 hours. Marker sizes represent the relationship between the breach and relocation temperatures; small: $T_{breach} < T_{reloc}$, large: $T_{breach} > T_{reloc}$.

As with the maximum cladding temperature, maximum fuel temperature exhibits a strong dependence on TaT model status for interactive materials model simulations, and no visible dependence on TaT model status for eutectics model simulations, shown in Figure 43. For interactive materials model simulations with the TaT model activated, maximum fuel temperatures are observed to match relocation temperatures up to 2400K except for a cluster of outcomes with relocation temperatures between ~2200 K - 2300 K and OXTH < R_{hold}. For higher relocation

temperature setpoints, maximum fuel temperatures are observed to stall between approximately 2400K-2600K. At maximum fuel temperatures between 2400K-2600K, undamaged TaT model expected lifetimes are between 10 and 30 minutes. Maximum fuel temperatures for simulations with the TaT model deactivated are observed to be greater than relocation temperature setpoints with rare exception. Similar to maximum cladding temperatures, it is suspected that these cases exceeded the setpoint before the relocation temperature setpoint was activated internally because of the existence of thick oxide layers that slowly melted until OXTH < R_{hold} became true and the rod subsequently collapsed. In this situation, limited heat transfer out of the fuel, into the cladding and oxide layer would allow fuel temperatures to exceed their liquidus temperature prior to Zr breakout. During that time, heat transfer is converted into latent heat in the cladding, and leads to a slow melt-off of the oxide layer until OXTH < R_{hold}. As in the case of maximum cladding temperatures, the eutectics model does not exhibit a stall in maximum fuel temperatures as a result of slow melt-off that is observed in interactive materials model simulations. Thus, fuel components are able to heat up beyond the SC 1132 setpoint until some fuel rod failure criterion is reached. In fact, maximum fuel temperatures are observed to range nearly uniformly from ~2300 K - ~3100 K.

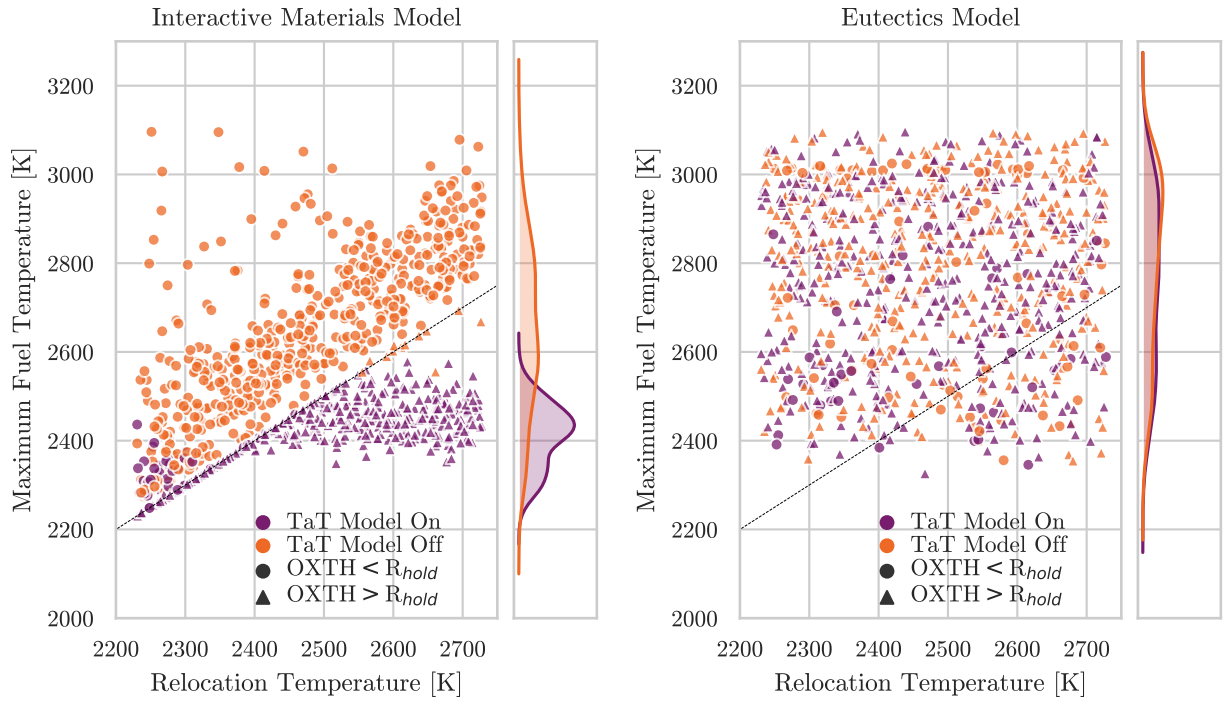

Figure 43. Maximum fuel temperature (y-axis) relationship with relocation temperature (x-axis). Marker types represent the integrity of the cladding oxide layer; circle: OXTH < R_{hold} (cannot hold up molten materials), triangle: OXTH > R_{hold} (can hold up molten materials).

Core plate failure, which marks the opening of a pathway for bulk material relocation to the lower plenum, is shown in Figure 44. Core plate degradation follows similar trends as cladding and fuel component degradation for both material interaction models. Core plate failure shows a strong dependence on TaT model status for interactive materials model simulations, but not eutectics model simulations. Interactive materials model simulations with the TaT model turned off exhibit extended core plate failure lifetime compared to simulations with the TaT model turned on. When the TaT model is turned off in interactive materials model simulations, degradation of fuel

components which have large masses and contain heat-bearing materials is delayed. In particular, a gap in core plate failure is observed between about 12-16 hours where relatively few core plate failure occurrences are observed. Conversely, when the TaT model is turned on in interactive materials model simulations, significant fuel component degradation presents the core plate with an earlier challenge by both heat-bearing debris and larger debris masses in general, leading to its earlier failure. A third cluster is observed for interactive materials model simulations, with the TaT model turned off and the breach temperature in excess of the relocation temperature (when the ratio between T_{reloc} and T_{breach} is less than 1.0). This cluster also promotes early fuel rod failure degradation and early challenge to the core plate by large debris masses and heat-bearing debris leading to early core plate failure. Eutectics model simulations also exhibit early fuel rod failure and consequently early core plate failure because of the more rapid fuel component degradation exhibited by the eutectics model simulations. Neither set of simulations shows a strong dependence on relocation temperature alone, which only indirectly affects the failure of the core plate. The challenge presented to the core plate by heat-bearing materials builds over time as hot debris accumulates on the core plate and transfers heat to it. Thus, the timing of debris relocation, in particular heat-bearing fuel debris, is a stronger factor on core plate failure than the temperature setpoint for debris failure. In other words, later relocation of heat bearing, fuel rod materials present a delay in the challenge to and failure of core structures at lower elevations.

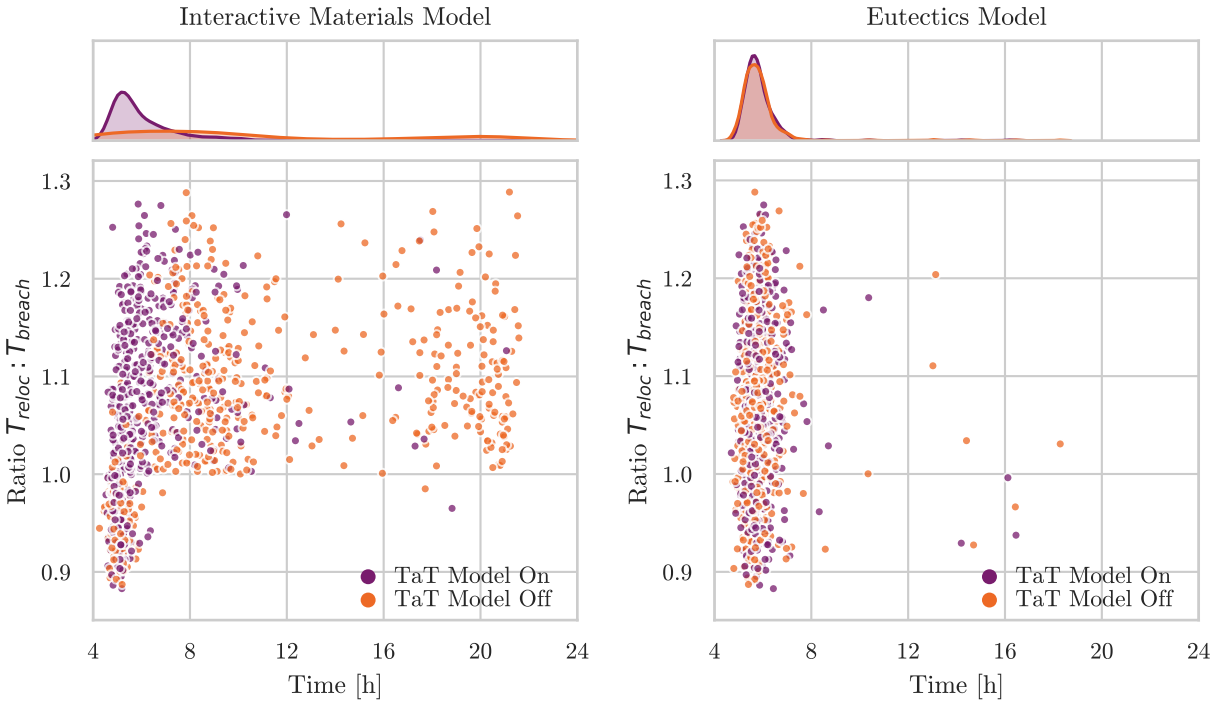

Figure 44. Core plate failure timing (x-axis) relationship with the ratio between relocation temperature and breach temperature (y-axis).

In conclusion, TaT model status is observed to impact many late phase core degradation figures of merit considered for interactive materials model simulations including maximum cladding and fuel component temperatures, degradation of fuel components, and core plate failure; no strong impacts by TaT model status is observed for eutectics model simulations. Furthermore, maximum cladding

and fuel temperatures are strongly affected by the relocation temperature setpoint in interactive materials model simulations. Finally, eutectics model simulations generally exhibit greater maximum cladding and fuel component temperatures than interactive materials model simulations. Eutectics model simulations also generally exhibit delayed degradation of control blade, fuel canister, and cladding components, but accelerated degradation of fuel components when compared to interactive materials model simulations.

3.5. RPV Lower Head Breach

Figure 45 shows a snapshot of the distribution of debris in the RPV at 6.5 hours. For total debris masses in the RPV, the eutectics model simulations exhibit stronger clustering than interactive materials model simulations centered near 90 Mg. Interactive materials model simulations exhibit weak clustering and range from ~ 15 Mg – 110 Mg nearly uniformly. The distribution of total debris mass in the RPV reflects fuel component degradation (Figure 38) at 6.5 hours, high debris masses correspond to significant fuel component degradation, because UO_2 in fuel components constitutes the largest material mass in the active core. In Figure 45, in the active core region, both sets of simulations exhibit clustering about low debris masses at 6.5 hours, centered about 5 Mg – 10 Mg, but also some cases with much larger debris masses in the active core, even > 80 Mg for interactive materials model simulations. Small debris masses (5Mg – 10 Mg) in the active core at 6.5 hours are obtained either because little core degradation has occurred or because core plate failure occurs after partial degradation of core structures at higher core elevations, preventing to buildup of debris on the core plate, in other words debris relocates to the lower plenum. Larger debris masses (e.g. >30 Mg, more than the total mass of materials in any single core ring) are obtained only when multiple rings of the core have endured significant degradation without failure of the supporting core plate. In the lower plenum, both sets of models exhibit two clusters, one at low debris masses and one at high debris masses. The primary cluster for interactive materials model simulations exhibit clustering about low debris masses near 12 Mg, while for eutectics model simulations the primary cluster is centered about much larger masses near 85 Mg. The low debris masses are indicative of debris hold-up by the core plate, while larger debris masses indicate significant degradation and failure of the core plate in multiple core rings.

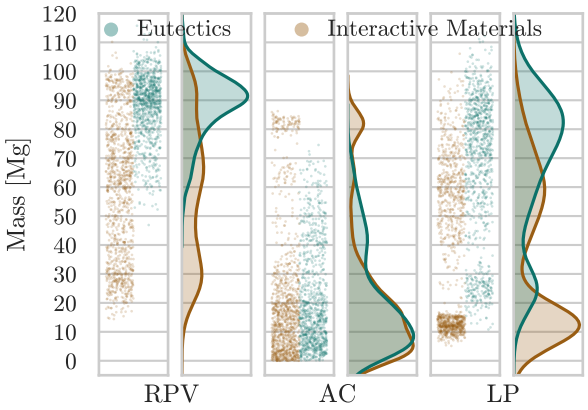

Figure 45. Debris mass distribution strip plots at 6.5 hours. The x-axis shows region categories in the RPV; RPV: entire RPV region, AC: active core region, LP: lower plenum region. The y-axis shows the debris mass in each region category for every realization.

Debris masses in the lower plenum region can be further subdivided into debris types: particulate debris, oxidic molten pool (MP1), and metallic molten pool (MP2). In Figure 46, the snapshot taken

at 6.5 hours shows that irrespective of material interaction model, the majority of lower plenum debris is particulate debris. The two regions of clustered results for overall lower plenum debris mass each model from Figure 45 are still visible and clustered similarly. Small masses of oxidic molten pool are observed in a small number of cases for both material interactions model simulations set. A larger number of simulations exhibit masses of metallic molten pool at 6.5 hours, however, it is still only a fraction of the overall mass in the active core. Formation of molten pools in the lower plenum is inhibited by the large inventory of water that provides some degree of cooling until lower plenum dryout occurs clustered about 7 hours.

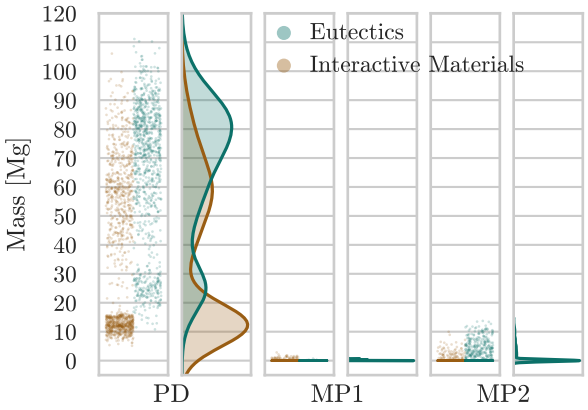

Figure 46. Lower plenum debris masses strip plot at 6.5 hours. The x-axis shows the debris type categories; PD: particulate debris, MP1: oxidic molten pool, MP2: metallic molten pool. The y-axis shows the mass of each debris type category for every realization.

Maximum particulate debris temperatures in the lower plenum are shown in Figure 47. Much like with cladding and fuel temperatures, the interactive materials model simulation set exhibits a strong dependence on TaT model status. Lower maximum temperatures are observed for simulations with the TaT model turned on, clustered near 2200K with no visible dependence on the relocation temperature setpoint. Conversely, simulations with the TaT model turned off exhibit maximum temperatures at or near the relocation temperature setpoint in the majority of cases. It is suspected that cases exhibiting maximum temperatures above the relocation temperature setpoint are the result of small masses receiving significant heat transfer that superheats the small material mass. Eutectics model simulations do not exhibit the same dependence on either TaT model status or relocation temperature. Instead, maximum particulate debris temperatures in the lower plenum for eutectics model simulations are clustered about ~2650K regardless of TaT model status or relocation temperature.

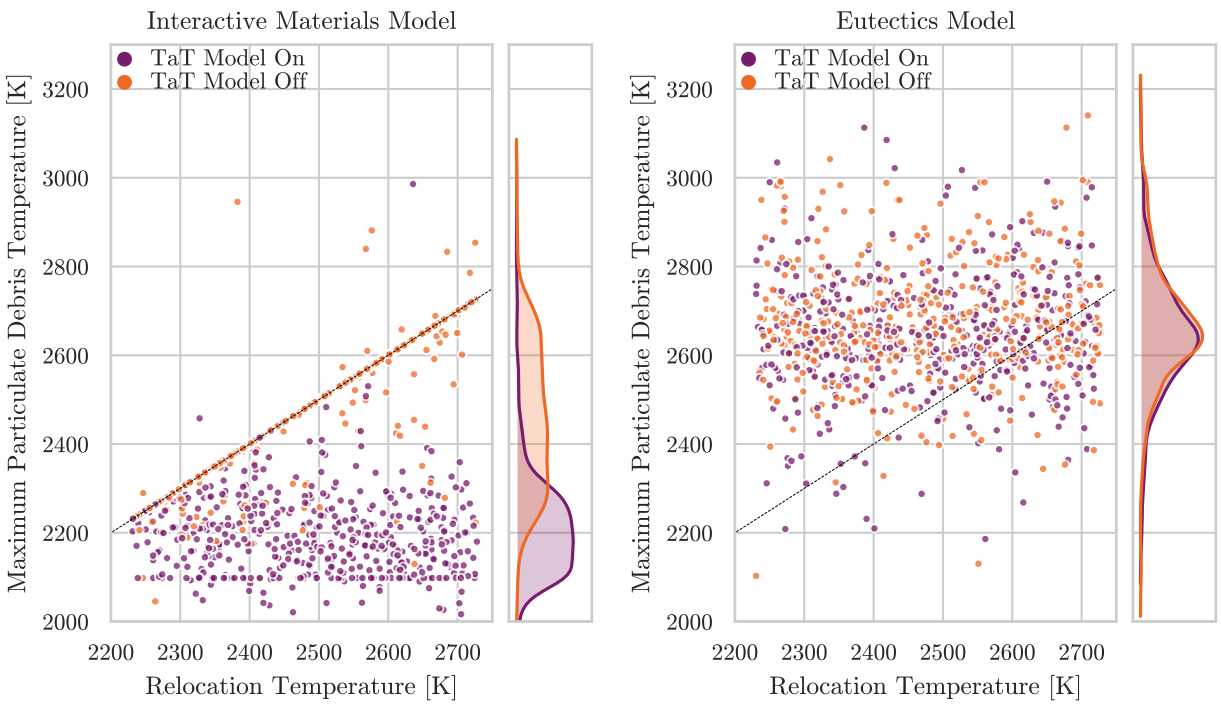

Figure 47. Maximum particulate debris temperature in the lower plenum (y-axis) relationship with relocation temperature (x-axis).

The relationship between maximum particulate debris mass in the lower plenum and time of lower head failure is shown in Figure 48. As with maximum temperatures, the interactive materials model outcomes show strong dependence on TaT model status. Simulations with the TaT model turned on exhibit greater variability in maximum particulate debris masses in the lower plenum than those with the model turned off, both the minimum and maximum value of maximum particulate debris mass occur when the TaT model is turned off. Furthermore, interactive materials model simulations with the TaT model turned on generally exhibit greater agreement with eutectics model simulation outcomes. Large particulate debris masses in the lower plenum correspond to early lower head failure for both material interaction model simulation sets, with the earliest failures occurring for similar active core particulate debris masses. Similarly, lower magnitudes of particulate debris in the active core correspond to the latest lower head failure occurrences unless core plate failure is delayed beyond 14 hours as observed for some interactive materials model simulations. Cases with the smallest magnitudes of maximum particulate debris masses in the active core occur because of debris holdup by the core plate.

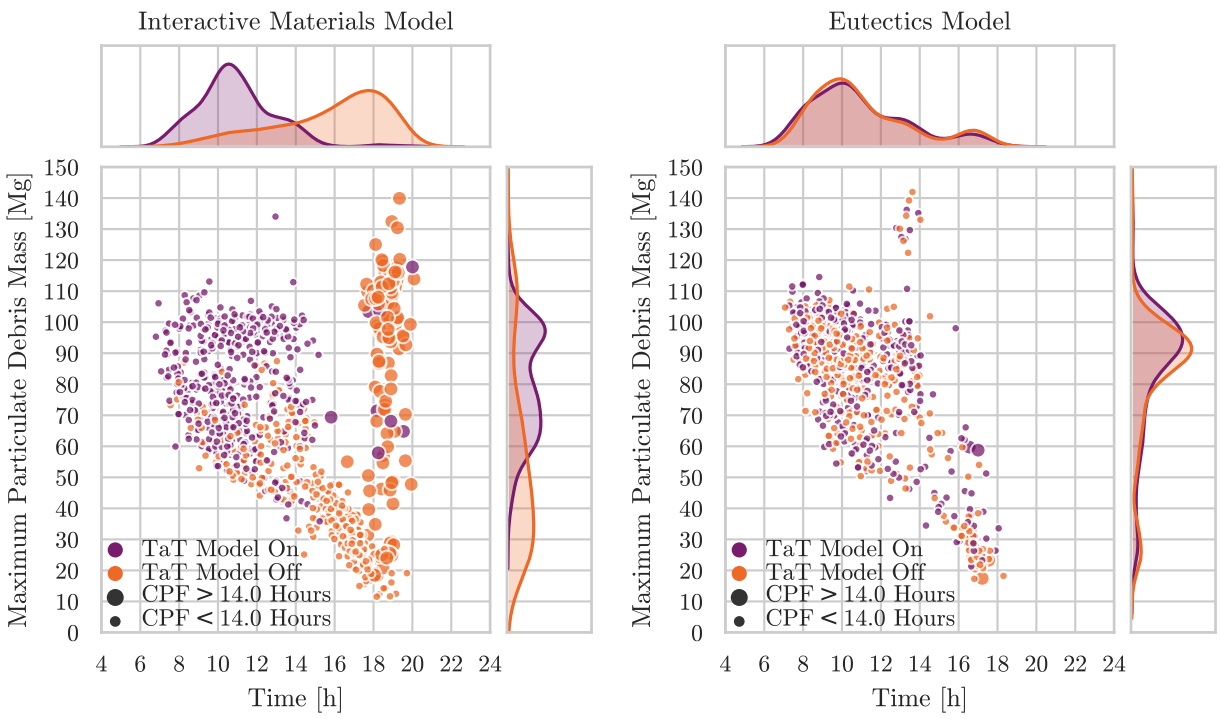

Figure 48. Maximum particulate debris mass in the lower plenum (y-axis) relationship to time of lower head failure (x-axis). Marker sizes represent the core plate failure timing; small: core plate failure timing < 14.0 hours, large: core plate failure timing > 14.0 hours.

Figure 49 shows maximum oxidic molten pool temperatures. The interactive materials model exhibits behavior akin to that previously discussed for cladding, fuel, and particulate debris components in Figures 41, 43, 47, respectively, that are likely familiar to readers by now; when the TaT model is turned off, maximum temperatures follow closely, the relocation temperature. A notable difference, however, is that a larger number of simulations exhibit maximum oxidic molten pool temperatures that exceed the relocation temperature when the TaT model is turned off. Furthermore, a relationship with the relocation is maintained in most simulations that are observed to exceed the relocation temperature, generally by about 50 K - 100 K. This observation is expected for oxidic debris, as the relocation temperature is defined as the liquefaction temperature for both UO_2-interactive and ZrO_2-interactive. After debris becomes molten, any additional heat is added as sensible heat to the mixture, allowing it to heat in excess of the melting point. For simulations that have the TaT model turned on, maximum oxidic molten pool temperatures are observed to be strongly clustered below the relocation temperature in most cases, centered about ~2250K. Cases with the TaT model turned on that exhibit temperatures significantly higher than the relocation temperature setpoint are rare, and it is suspected that the behavior is the result of small masses receiving adequate heat transfer to significantly superheat the material. Finally, as before, the eutectics model does not exhibit any visible dependence on TaT activation or relocation temperature.

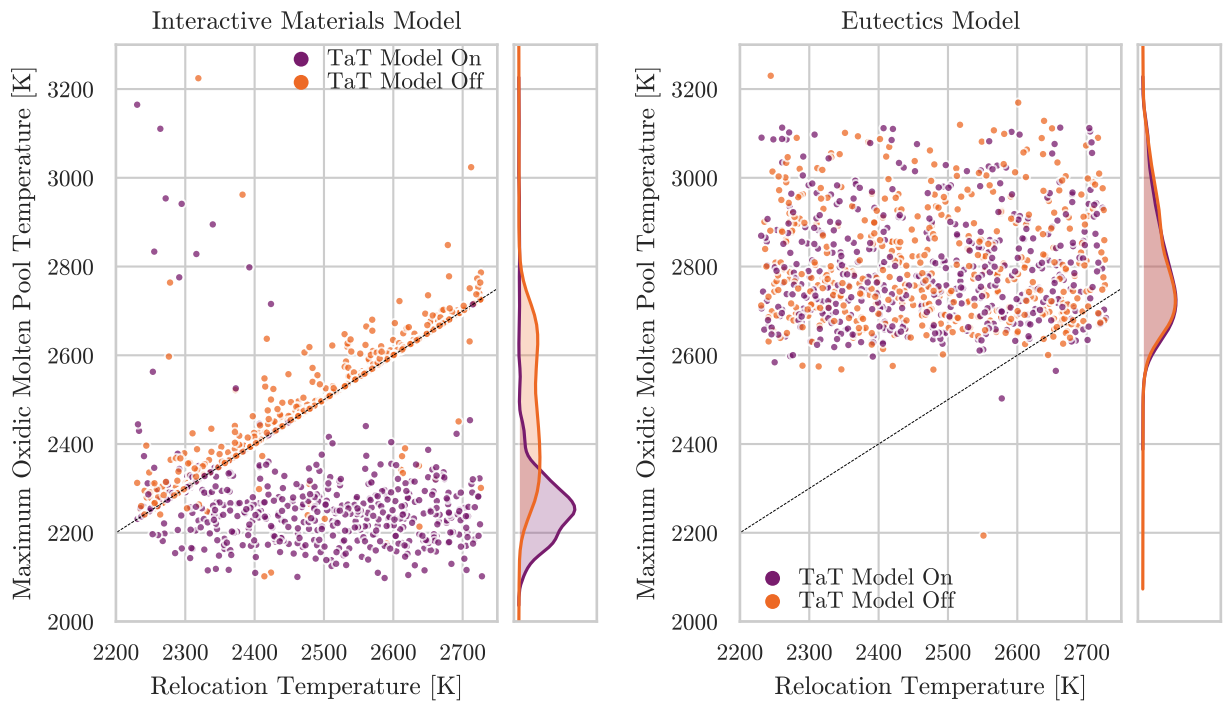

Figure 49. Maximum oxidic molten pool temperature in the lower plenum (y-axis) relationship with relocation temperature (x-axis).

Maximum metallic molten pool temperatures are shown in Figure 50. Once again, the behavior exhibited by interactive materials model simulations is similar to fuel, cladding, particulate debris, and oxidic molten pool components; namely a strong dependence on TaT model status. Interactive materials model simulations that have the TaT model turned off exhibit a strong relationship between maximum temperatures and the relocation temperature setpoint. Contrary to the oxidic molten pool, which is composed of high melting point ceramic materials like UO_2 and ZrO_2, many simulations with the TaT model turned off exhibit maximum temperatures below the relocation temperature setpoint. This occurs because materials in the metallic molten pool, such as Zr and stainless steel, have lower melting points than the relocation temperature setpoint and the materials that agglomerate into the oxidic molten pool. Some interactive materials model simulations exhibit maximum temperatures in excess of the relocation temperature setpoint; as with other core components, it is believed that these temperatures are achieved for small masses receiving enough heat transfer to superheat the materials. Simulations with the TaT model turned on exhibit lower maximum temperatures, clustered more strongly about ~2250 K. The lowest maximum metallic pool temperatures are ~2100 K, or the melting point of Zr. Eutectics model simulations show no visible dependence on relocation temperature or TaT status.

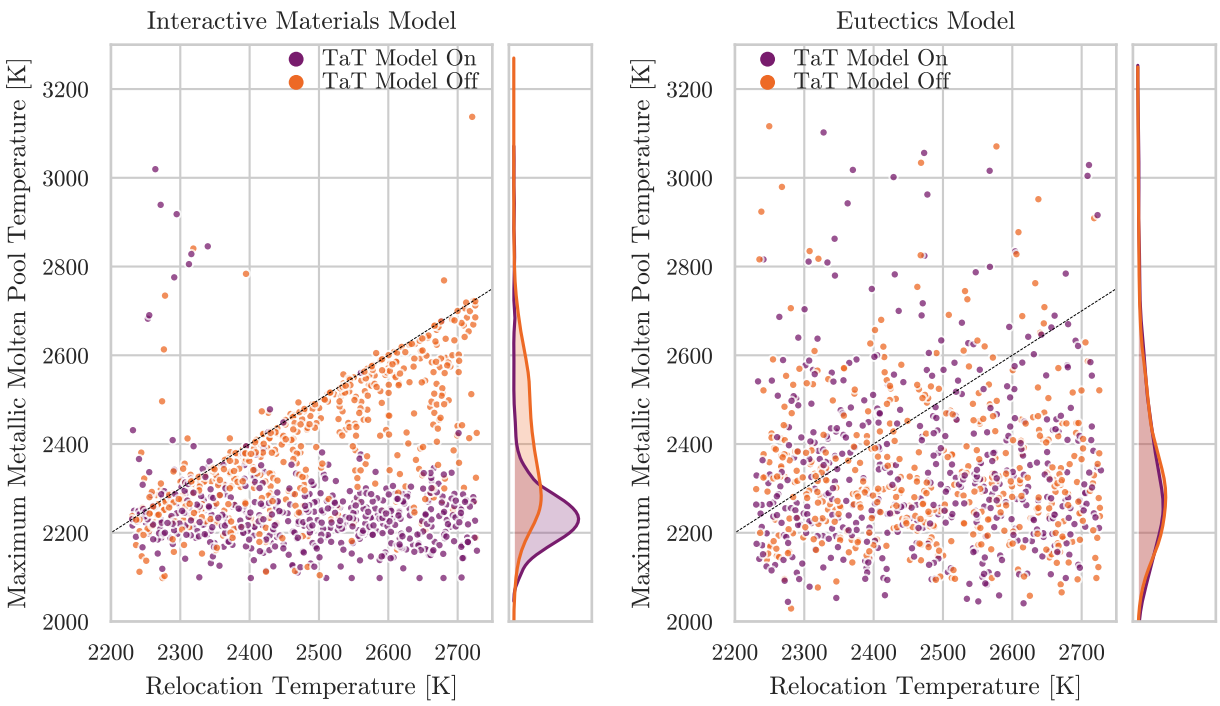

Figure 50. Maximum metallic molten pool temperature in the lower plenum (y-axis) relationship with relocation temperature (x-axis).

Figure 51 shows a snapshot at 10.3 hours for the relationship between lower head temperature of the innermost lower head node of ring 1, lower plenum debris masses, TaT model status, lower plenum dryout status 1.5 hours prior (at 8.8 hours), and lower head failure status. Simulations for both material interaction models that have not completely boiled off the water inventory at 10.3 hours in the lower plenum exhibit temperatures <600 K. Furthermore, simulations for both material interaction models exhibit a period of lower head heat-up visible for simulations that are still within 1.5 hours of active core dryout, demonstrated by simulations that exhibit lower plenum dryout after 8.8 hours and lower head temperatures between ~600 K – ~800 K. Simulations that exhibit lower plenum dryout prior to 8.8 hours exhibit temperatures greater than ~800 K. Heat-up behavior for eutectics model simulations is independent of TaT model status and consistent across simulations, heating to ~800 K as debris accumulates in the lower plenum. Interactive materials model simulations do not exhibit the same consistency in lower head heat-up, but do exhibit a dependence on TaT model status. At 10.3 hours, interactive materials model simulations with the TaT model turned off exhibit lower head heat-up in the presence of smaller lower plenum debris masses (20Mg), while simulations with the TaT model turned on do not generally exhibit heat-up until large (~70Mg) of debris has relocated to the lower plenum. Beyond ~800K, neither model exhibits a strong relationship between lower plenum debris mass and lower head temperature, with cases exhibiting rapidly increasing lower head temperatures. Finally, both material interaction models exhibit small lower plenum debris masses for cases that have undergone lower head failure with lower head temperatures between ~800K and 1600K.

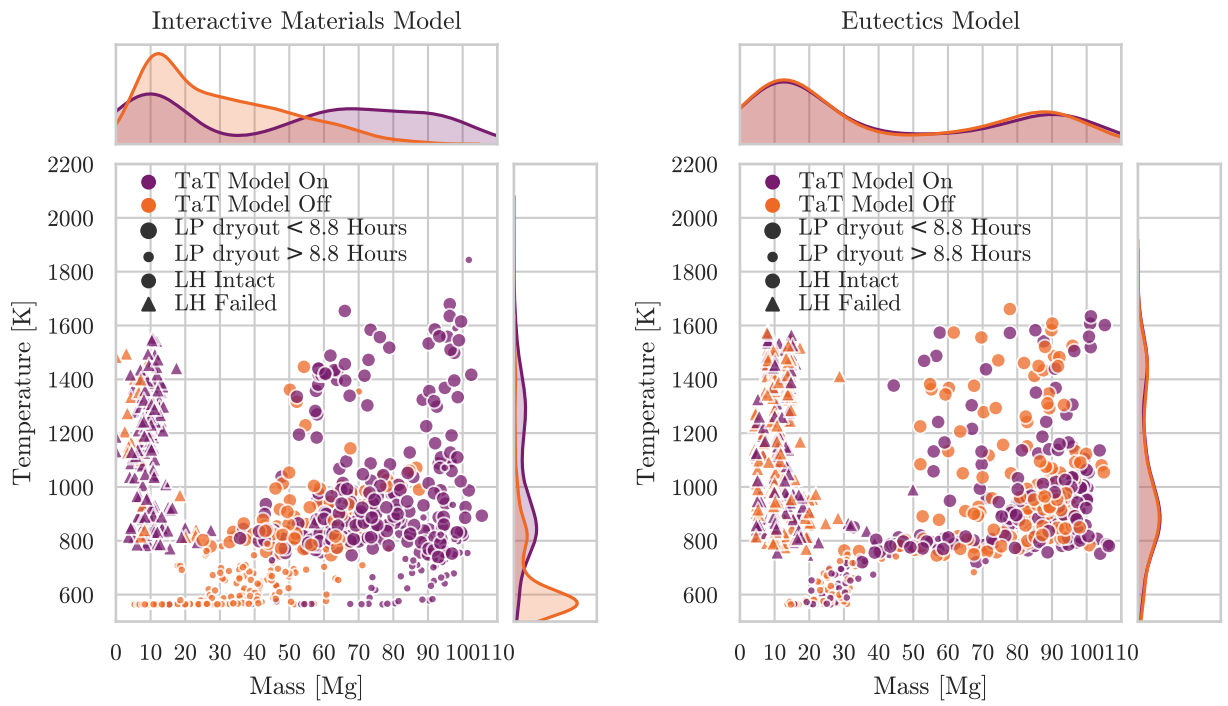

Figure 51. Lower head temperature (y-axis) relationship with debris mass in the lower plenum (x-axis) at 10.3 hours. Marker types represent lower head damage states; circle: lower head intact, triangle: lower head failed. Marker size represents lower plenum dryout timing; small: lower plenum dryout > 8.8 hours, large: lower plenum dryout < 8.8 hours.

Figure 52 compares lower head failure between simulations for each material interaction model. As in the case for core plate failure, the interactive materials model exhibits a strong dependence on TaT model status, whereas the eutectics model simulations show no similar dependence. Interactive materials model simulations with the TaT model turned off exhibit delayed lower head failure compared to simulations with the TaT model turned on. The delayed lower head failures are clustered near 18 hours. When the TaT model is turned on lower head failure outcomes are clustered about 10.5 hours. Interactive materials model simulations with the TaT model turned off also exhibit a strong relationship between lower head failure and the ratio of the relocation temperature and breach temperature parameters. If the breach temperature is greater than the relocation temperature, then lower head failure is observed to occur at similar times regardless of TaT model status. Eutectics model simulations do not show a strong relationship between lower head failure and the ratio of relocation temperature and breach temperature parameters. Eutectics model simulations exhibiting lower head failure times >16 hours were found to have smaller maximum lower plenum debris masses, implying a reduced challenge to the lower head by lower plenum debris.

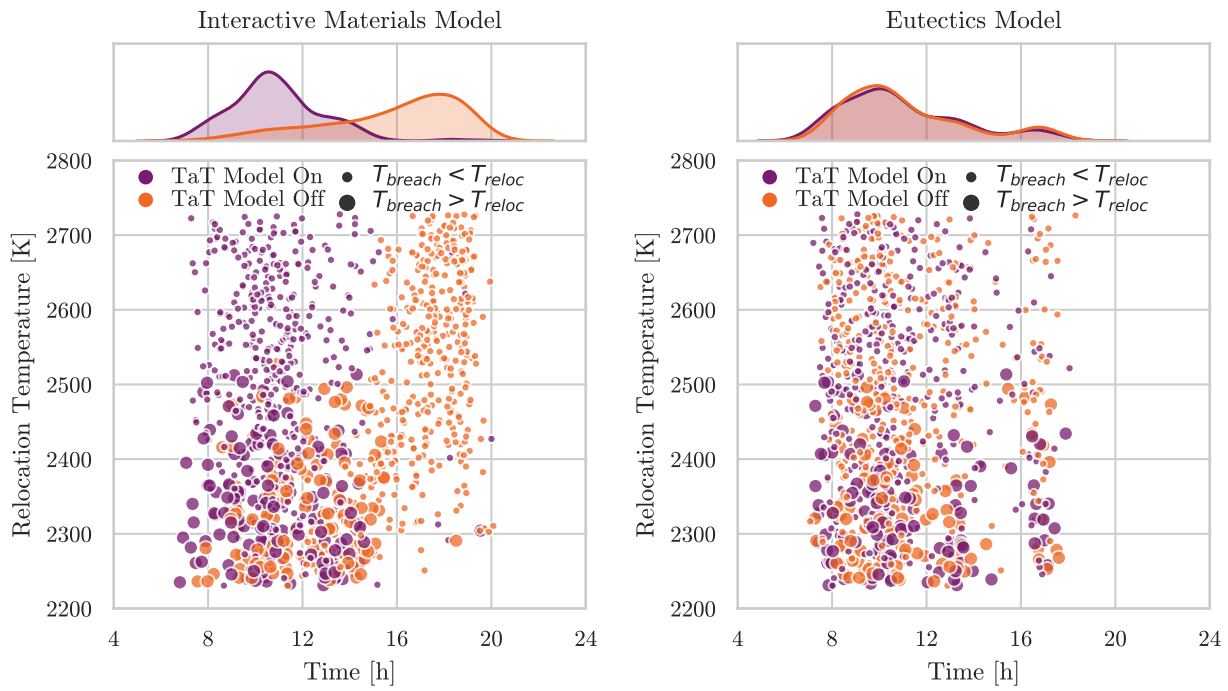

Figure 52. Lower head failure timing (x-axis) relationship with relocation temperature (y-axis). Marker sizes represent the relationship between the breach and relocation temperatures; small: $T_{breach} < T_{reloc}$, large: $T_{breach} > T_{reloc}$.

Debris ejection by material at 25.0 hours is shown in Figure 53. The eutectics model exhibits stronger clustering for all materials than the interactive materials model. Clusters for each material are also centered about larger magnitudes for eutectics model simulations. Overall, the eutectics model exhibits more significant core degradation by 25.0 hours (not shown), especially of fuel components. Most simulations exhibit significant degradation of core components in rings 1-4, with partial degradation of ring 5 structures. One notable exception is to this trend is interactive materials model simulations exhibiting minimal degradation of ring 4 fuel components. The presence of intact fuel components in ring 5 (and ring 4 for the notable exceptions) indicates that core plate failure did not occur in that ring and continues to hold up debris. Finally, the simulations that exhibited 100% failure of fuel components also exhibit near complete ejection of tracked core masses ~140Mg-150Mg; while rare for both material interaction models, this condition was observed more often for interactive materials model simulations.

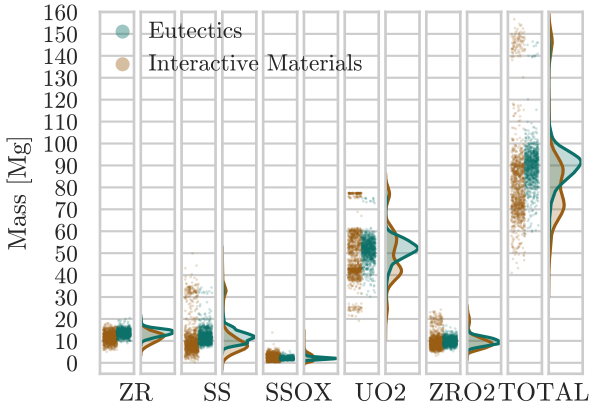

Figure 53. Ejected debris masses strip plot at 25.0 hours. The x-axis shows categories of core materials; ZR: zirconium, SS: stainless steel, SSOX: oxidized stainless steel, UO2: uranium dioxide, ZRO2: oxidized zirconium, TOTAL: all core materials. The y-axis shows the mass of each core material category for every realization.

To summarize, eutectics model simulations generally exhibit more significant degradation of core components, larger debris masses, and earlier relocation of large debris masses to the lower plenum. Further, maximum debris temperatures are generally higher in eutectics model simulations. The largest masses of ejected debris are observed to occur for interactive materials model simulations, however, eutectics model simulations generally exhibit larger masses of ejected debris. Interactive materials model simulations continue to exhibit a strong dependence on TaT model status between core plate failure and lower head failure. In particular maximum debris temperatures are strongly influenced by relocation temperature setpoints when the TaT model is turned off. Finally, lower head temperatures and lower head failure are also impacted by TaT model status.

4. CONCLUSIONS

Through this uncertainty analysis, model form biases of two material interaction models and their effect on core degradation have been interrogated. The impact of material interaction modeling choice has been demonstrated throughout in-core accident progression including hydrogen generation, thermal hydraulic response, late phase reactor core degradation, and accident progression leading up to RPV lower head breach. In particular, model biases in combination with parametric variation are observed to strongly influence phenomenological shifts sensitive to key events such as core plate failure and lower head failure. The importance of such phenomenological shifts, regardless of basis (i.e. parametric uncertainty, model form uncertainty, or events uncertainty), is that they introduce the potential for gross bifurcations in accident progression pathways and characteristics that can ultimately lead to different plant end-states.

Snapshots of thermal hydraulic phenomena during core degradation show that while the progression to a given thermal hydraulic plant state (e.g. TAF, BAF, LP dryout) may look different between two simulations, the thermal hydraulic phenomena follow similar pathways between accident states. No gross bifurcations are observed for thermal-hydraulic phenomena or pathways between simulations using different material interaction models. Gross bifurcations, however, are observed between core damage states (e.g. drywell pressure before and after lower head failure).

Material interaction, candling, and fuel rod failure models are shown to have dominant effects on figures of merit. Conversely, debris quenching and dryout model effects are not found to be the dominant factor for any figure of merit outcomes analyzed in this study. Notable, consistent differences are observed between simulations utilizing each material interaction model. Simulations that utilized the eutectics model are found to consistently generate less in-vessel hydrogen than interactive material model simulations. Eutectics model simulations exhibit accelerated degradation of fuel components throughout the accident scenario, especially in interior core rings. Higher maximum temperatures are also observed for intact core components when the eutectics model is utilized. In particular, maximum fuel and cladding temperatures are consistently observed to exceed maximum temperatures observed for interactive materials model simulations. Similarly, eutectics model simulations exhibit higher maximum debris temperatures in the lower plenum. Earlier core plate failure observed for eutectics model simulations leads to earlier lower plenum dryout and lower head failure. Figures of merit do not exhibit a strong dependence on TaT model status for eutectics

model simulations; a weak dependence may be exist for cladding and fuel temperatures and intact mass fractions.

Contrary to the eutectics model simulations, interactive materials model simulations show a strong dependence on TaT model status for nearly all figures of merit. When the TaT model is turned on, interactive materials model simulated accident progression agrees more strongly with eutectics model simulation outcomes. When the TaT model is turned off, however, gross bifurcations in simulation outcomes are observed, especially for core plate failure and lower head failure timings. Other notable differences include the maximum temperature "limitation" on maximum fuel, cladding, and debris temperatures. While exceptions are observed, interactive materials model simulations show a strong relationship between maximum temperatures for fuel, cladding, particulate debris, oxidic molten pool , and metallic molten pool components and the relocation temperature setpoint when the TaT model is turned off. The same relationship is not observed for interactive materials model simulations when the TaT model is turned on. When the TaT model is turned on, maximum temperatures are found to stay below the relocation temperature setpoint except in the case of low setpoint magnitudes. Ultimately, these characteristics imply reduced core temperatures implying smaller heat transfer to structures by debris, which is consistent with the extended component lifetimes observed for fuel components, the core plate, and the lower head.

While greater molten debris masses are observed for eutectics model simulations, simulations using both material interaction models exhibit large quantities of particulate debris that are in significant excess of molten debris masses, particularly in the lower plenum. It should be noted that when components collapse due to loss of supporting structures and other failure mechanisms, they are converted to particulate debris. Eutectics model simulations consistently exhibit a greater degree of overall core degradation. After lower head failure, debris that has accumulated in the lower plenum is ejected. Inevitably the impact of material interaction modeling choice also extends into ex-vessel phenomena as shown by the quantity and composition of ejected debris, which are larger for all material types.

The conclusions of this analysis should not be extended to other reactor types or accident scenarios without consideration of design and accident scenario differences; the presented results and conclusions are specific to short term SBO scenario of BWR that undergoes high pressure melt ejection under representative Fukushima Daiichi Unit 1 boundary conditions. The importance of material interactions cannot be undervalued to analysis of current and future reactor technologies. In particular, the effect of material interactions on accident tolerant and high burnup fuels merits further investigation from a systems perspective similar to that provided here. Similarly, the impact of material interactions on future reactor technologies merits further investigation. Forthcoming reactor technologies not only feature different material systems (different from primarily UO_2-Zircaloy-Stainless Steel), but also migrating components in some cases. In other words, the nature of postulated accidents for these reactor technologies may exhibit increased complexity. In particular, gross bifurcations in postulated accident characteristics and plant end-states that emerge as a result of increasing degrees of freedom from material interactions and other phenomena are of significant interest.

ACKNOWLEDGEMENTS

Part of this work was conducted in coordination with the IAEA CRP I31033 on Advancing the State-of-Practice in Uncertainty and Sensitivity Methodologies for Severe Accident Analysis in Water Cooled Reactors.

This work was jointly supported by the U.S. DOE-NE IUP Fellowship Program and the United States Nuclear Regulatory Commission. The views expressed in the article do not necessarily represent the views of the U.S. Department of Energy or the United States Government.

Sandia National Laboratories is a multimission laboratory managed and operated by National Technology & Engineering Solutions of Sandia, LLC, a wholly owned subsidiary of Honeywell International Inc., for the U.S. Department of Energy's National Nuclear Security Administration under contract DE-NA0003525.

SAND2021-9601 J

REFERENCES

[1] L. I. Albright, N. Andrews, L. L. Humphries, M. H. Piro, G. E. Sjoden, D. L. Luxat and T. Jevremovic, "Material Interactions in Severe Accidents - Benchmarking the MELCOR V2.2 Eutectics Model for a BWR-3 Mark-I Station Blackout: Part I - Single Case Anlaysis," *Submitted.*

[2] P. Hoffman, "Current Knowledge on Core Degradation Phenomena, a Review," *Journal of Nuclear Materials,* vol. 270, pp. 194--211, 1999.

[3] B. R. Sehgal, Nuclear Safety in Light Water Reactors: Severe Accident Phenomenology, Oxford, UK: Academic Press, 2012.

[4] OECD Nuclear Energy Agency, "Benchmark Study of the Accident at the Fukushima Daiichi Nuclear Power Plant - (BSAF Project) -- Phase I Summary Report," OECD/NEA/CSNI, 2016.

[5] L. L. Humphries, B. A. Beeny, C. Faucett, F. Gelbard, T. Haskin, D. L. Louie and J. Phillips, "MELCOR Computer Code Manuals Reference Manual, Vol. 2: Reference Manual," U.S. Nuclear Regulatory Commission, Washington, DC, 2019.

[6] L. L. Humphries, B. A. Beeny, F. Gelbard, D. L. Louie and J. Phillips, "MELCOR Computer Code Manuals Reference Manual, Vol. 1: Primer and Users' Guide," U.S. Nuclear Regulatory Commission, Washington, DC, 2019.

[7] M. Barrachin, O. de Luze, T. Haste and G. Repetto, "Late Phase fuel degradation in the Phébus FP tests," *Annals of Nuclear Energy,* vol. 61, pp. 36-53, 2013.

[8] Y. Pontillon, P. P. Malgouyres, G. Ducros, G. Nicaise, R. Dubourg, M. Kissane and M. Baichi, "Lessons learnt from VERCORS tests," *Journal of Nuclear Materials,* vol. 344, pp. 265-273, 2005.

[9] M. R. Denman, "Development of the SharkFin Distribution for Fuel Lifetime Estimates in Severe Accident Codes," American Nuclear Society Winter Meeting, Las Vegas, NV, 2016.

[10] R. J. Lipinski, "Model for boiling and dryout in particle beds. [LMFBR]," U.S. Nuclear Regulatory Commission, Washington D.C., 1982.

[11] L. I. Albright, N. Andrews, L. L. Humphries, R. O. Gauntt and T. Jevremovic, "Uncertainty Analysis of Corium Relocation to the Lower Plenum Using Results from The OECD/NEA BSAF Phase II Project," Portland,OR, August, 2019.

[12] P. Mattie, R. Gauntt, K. Ross, N. Bixler, D. Osborn, C. Sallaberry, J. Jones and T. Ghosh, "State-of-the-Art Reactor Consequence Analysis Project: Uncertainty Analysis of the Unmitigated Long-Term Station Blackout of the Peach Bottom Atomic Power Station," U.S. Nuclear Regulatory Commission, Washington, D.C., 2016.

[13] K. Ross, N. Bixler, S. Weber, C. Sallaberry and a. J. Jones, "State-of-the-Art Reactor Consequence Analyses Project: Uncertainty Analysis of the Unmitigated Short-Term Station Blackout of the Surry Power Station Draft Report," U.S. Nuclear Regulatory Commission, Washington, D.C., Draft Report retrieved 2020.

[14] Sandia National Laboratories , "State-of-the-Art Reactor Consequence Analysis (SOARCA) Project: Sequoyah Integrated Deterministic and Uncertainty Analyses Draft Report," U.S. Nuclear Regulatory Commission, Washington, D.C., Draft Report retrieved 2020.

[15] R. S. Moore and K. J. Notz, "Physical Characteristics of GE BWR Fuel Assemblies," Oak Ridge National Laboratory, Oak Ridge, TN, 1989.

[16] M. Steinbrück, "Degradation and Oxidation of B4C Control Rod Segments at High Temperatures," *Journal of Nuclear Materials,* vol. 400, no. 2, pp. 138-150, 2010.

DISTRIBUTION

Email—Internal

Name	Org.	Sandia Email Address
Technical Library	01977	sanddocs@sandia.gov

Email—External (encrypt for OUO)

Name	Company Email Address	Company Name
Shawn Campbell	Shawn.Campbell@nrc.gov	Nuclear Regulatory Commission

This page left blank

This page left blank

Sandia National Laboratories

Sandia National Laboratories is a multimission laboratory managed and operated by National Technology & Engineering Solutions of Sandia LLC, a wholly owned subsidiary of Honeywell International Inc. for the U.S. Department of Energy's National Nuclear Security Administration under contract DE-NA0003525.